Volumetric Particle Velocimetry for Microscale Flows

by

Steven Adam Klein

A Dissertation Presented in Partial Fulfillment
of the Requirements for the Degree
Doctor of Philosophy

Approved June 2011 by the
Graduate Supervisory Committee:

Jonathan Posner, Chair
Kangping Chen
David Frakes
Shankar Devasenathipathy
Ronald Adrian

ARIZONA STATE UNIVERSITY

August 2011

ABSTRACT

Microfluidics is the study of fluid flow at very small scales (micro -- one millionth of a meter) and is prevalent in many areas of science and engineering. Typical applications include lab-on-a-chip devices, microfluidic fuel cells, and DNA separation technologies. Many of these microfluidic devices rely on micron-resolution velocimetry measurements to improve microchannel design and characterize existing devices. Methods such as micro particle imaging velocimetry (μPIV) and micro particle tracking velocimetry (μPTV) are mature and established methods for characterization of steady 2D flow fields. Increasingly complex microdevices require techniques that measure unsteady and/or three dimensional velocity fields.

This dissertation presents a method for three-dimensional velocimetry of unsteady microflows based on spinning disk confocal microscopy and depth scanning of a microvolume. High-speed 2D unsteady velocity fields are resolved by acquiring images of particle motion using a high-speed CMOS camera and confocal microscope. The confocal microscope spatially filters out of focus light using a rotating disk of pinholes placed in the imaging path, improving the ability of the system to resolve unsteady μPIV measurements by improving the image and correlation signal to noise ratio.

For 3D3C measurements, a piezo-actuated objective positioner quickly scans the depth of the microvolume and collects 2D image slices, which are stacked into 3D images. Super resolution μPIV interrogates these 3D images using μPIV as a predictor field for tracking individual particles with μPTV. The

3D3C diagnostic is demonstrated by measuring a pressure driven flow in a three-dimensional expanding microchannel. The experimental velocimetry data acquired at 30 Hz with instantaneous spatial resolution of 4.5 by 4.5 by 4.5 μm agrees well with a computational model of the flow field. The technique allows for isosurface visualization of time resolved 3D3C particle motion and high spatial resolution velocity measurements without requiring a calibration step or reconstruction algorithms. Several applications are investigated, including 3D quantitative fluorescence imaging of isotachophoresis plugs advecting through a microchannel and the dynamics of reaction induced colloidal crystal deposition.

DEDICATION

To my family and friends (all of you), who have always supported me.

ACKNOWLEDGEMENTS

I would like to acknowledge the following individuals:

- My committee chair and faculty advisor, Dr. Jonathan D. Posner. His work ethic, technical strength, and practical advice instilled into me what it means to be a professional researcher. Working in his lab allowed me to grow as an engineer and taught me what is expected from a technical professional. The experience I gained working with him is indispensible to me.

- My committee members, Dr. Ronald Adrian, Dr. Kangping Chen, Dr. Shankar Devasenathipathy, and Dr. David Frakes. As a teaching assistant in Dr. Adrian's lab, I learned much from him about optics and experimental fluid mechanics measurements. More importantly, I learned that you do not understand a subject fully until you teach it to others. It was a humbling experience, and one that will stay with me throughout my career. Dr. Frakes and Dr. Chen's lectures provided insight into Image Processing and Fluid Mechanics respectively, and the advice and collaboration of Dr. Frakes was invaluable to developing this 3D3C particle velocimetry technique. Dr. Devasenathipathy's expertise in μPIV and μPTV measurements and diagnostic development proved to be a valuable asset to my work, and I greatly appreciated his technical and practical advice.

- My parents, Kathryn and Ronald Klein, for supporting me through my undergraduate degree, for supporting my decision to attend

graduate school, and for supporting me in many other ways throughout my life.

- Last but not least, my girlfriend Amanda, who has been with me throughout the entirety of my graduate career and has supported me more than anyone as I tiptoed through the hindrances and highlights of graduate school.

TABLE OF CONTENTS Page

LIST OF FIGURES

Figure Page

Figure Page

LIST OF TABLES

CHAPTER 1

INTRODUCTION

In this chapter I provide motivation for the development of the high speed 3D3C velocimetry system, present the goals and expected impact of the current work, list the limitations of temporally resolved 3D velocity measurements at the microscale, and review existing work on temporally resolved velocimetry in microchannels.

1.1. Motivation

Micron-scale velocity measurements are an important part of the design of microfluidic devices ranging from micromixers to biosensors and lab-on-a-chip systems (also known as micro total analysis systems (μTAS)). Applications for these microdevices include microscale fuel cells, the detection of hazardous chemicals, and the separation of proteins for fast disease diagnosis. Experimental characterization of the flow inside these structures helps improve their design. With features on the order of 10 micrometers (μm), microscopy is typically required for accurate measurement of velocities in microdevices. There is demand in industry and academia to provide new tools for faster and more accurate measurement of microscale velocity fields and particle tracking.

Microfluidic devices are becoming steadily more common, with many companies fabricating microfluidic chips and other microfluidic technology, including Agilent, Honeywell, Illumina, Micralyne, Caliper Lifesciences, and many others (Haber 2006).

Measuring the temporal evolution of unsteady microscale flow fields is important for devices with complex structures (Trau, Saville, and Aksay 1997; Garstecki et al. 2006; Posner and Santiago 2006). Additionally, the ability to resolve 3D velocity fields in microchannels is an active area of interest (Bown, MacInnes, and Allen 2007; Cierpka et al. 2010; Erkan et al. 2008; Nagai et al. 2009; Park and Kihm 2006; Pereira et al. 2006; Peterson, Chuang, and Wereley 2008; Shinohara et al. 2005; Yoon and Kim 2006). In this dissertation, I develop a diagnostic for the measurement of temporally resolved high-speed 2D flows and temporally resolved volumetric 3D3C microflows using a confocal system to improve temporal measurements and a piezo-actuated objective positioner to scan the microchannel depth and obtain direct information about the third component of velocity.

1.2. Literature Review

Particle imaging velocimetry (PIV) is a robust diagnostic for the measurement of unsteady two dimensional velocity fields (Adrian 1991, 1984). For reasonably high volume fractions (5-10 particles per velocity vector) PIV obtains reliable measurements, whereas for low volume fraction flows particle tracking velocimetry (PTV) can track individual particles (one particle per vector).

PIV and PTV have been adapted to the study of microscale flows using epifluorescence microscopy and volume illumination (Santiago et al. 1998). Termed micro particle imaging velocimetry (μPIV) and micro particle tracking velocimetry (μPTV) , these are mature techniques used to study flows at the

microscale (Meinhart, Wereley, and Santiago 1999; Santiago et al. 1998; Wereley, Gui, and Meinhart 2002; Crocker and Grier 1996; Adrian 2005). For more information on the μPIV and μPTV techniques and recent advances in the field, see Wereley and Meinhart (Wereley and Meinhart 2010), Lee and Kim (Lee and Kim 2009), and Lindken et al. (Lindken et al. 2009).

Resolving temporally resolved 3D3C velocity fields is difficult in a microfluidic chip for two main reasons. First, μPIV is typically limited to steady flows. Macroscale PIV and PTV use a laser light sheet to define the measurement plane. However, it is too difficult to construct a light sheet small enough for microchannels (~100 microns), so volume illumination is used. One result is that the depth of field of the objective and the particle tracer diameter determine the depth of the measurement plane instead of the light sheet thickness. Additionally, volume illumination causes light from out of focus particles to impede the measurement by causing background noise in the images. Ensemble averaging of the correlation maps in correlation space (Meinhart, Wereley, and Santiago 2000) resolves the problem with background noise from out of focus light by improving the signal to noise ratio in correlation space (S/N) which is defined as the ratio of the highest to the second highest correlation peak (Keane and Adrian 1992). However, correlation ensemble averaging is only useful for steady or periodic flows because it is essentially a time average in correlation space. Secondly, classical μPIV and μPTV systems capture 2D particle images along a single measurement plane, and therefore do not inherently obtain information about the third dimension of velocity.

One way to improve the ability of μPIV and μPTV to measure unsteady and temporally resolved flows is to improve the correlation S/N. Correlation S/N is an important parameter, because higher S/N increases the likelihood that the vector will not be erroneous. Light from out of focus particles, (Klein and Posner 2010; Meinhart, Wereley, and Gray 2000; Olsen and Adrian 2000), Brownian motion (Olsen and Adrian 2000), and velocity gradients (Olsen 2009, 2010) reduce the correlation S/N. Ensemble averaging in correlation space improves the S/N, but is essentially a time average (Meinhart, Wereley, and Santiago 2000). Therefore, ensemble averaging is ineffective for unsteady flows, which require more sophisticated interrogation algorithms or adequate two-frame correlation S/N ratios. Confocal microscopes use a pinhole to spatially filter images, removing out of focus light and more accurately depicting the physical shape of tracer particles (Petran et al. 1968; Sheppard and Choudhury 1977; Brakenhoff 1979; Corle, Chou, and Kino 1986; Carlsson and Aslund 1987; Xiao, Corle, and Kino 1988; Kino and Corle 1989). Confocal microscopy has been shown to improve image S/N and correlation S/N (Klein and Posner 2010), as well as reduce depth averaging (Park, Choi, and Kihm 2004; Park and Kihm 2006). Single pinhole confocal systems are generally too slow for unsteady flows because the pinhole must raster scan the image (Tanaami et al. 2002). To improve the image acquisition time, a Nipkow disk, which is simply a disk with an array of micron scale pinholes, rotates through the image plane of the imaging system (Petran et al. 1968). Spinning disk confocal systems allow for much faster image acquisition than single pinhole microscopes, with recent models allowing

frame rates of 2000 Hz. Robust phase correlation (Eckstein and Vlachos 2009) also improves time resolved μPIV measurements (Schmieg et al. 2009; Eckstein, Charonko, and Vlachos 2008) by leveraging an advanced version of the generalized cross-correlation technique (Wernet 2005). Either increasing the S/N (by using a confocal or some other method) or using advanced algorithms such as robust phase correlation will improve the measurement of unsteady microscale flows.

Phase-locked ensemble averaging has been used in μPIV to improve the correlation S/N for unsteady periodic flows such as droplet generation in microfluidic devices (van Steijn, Kreutzer, and Kleijn 2007) and the periodic flow in an inkjet printhead (Meinhart and Zhang 2000). Additionally, selective seeding methods have been implemented in microfluidic devices to create a thin plane of illuminated particles normally accomplished by a light sheet in macro PIV (Mielnik and Saetran 2006).

Two-frame correlation μPIV (no ensemble averaging) has been demonstrated for the measurement of vortex-like motion at the interface of a two phase (water – oil) laminar flow (Shinohara et al. 2004). The μPIV measurement depth --- defined as the depth over which particles contribute to μPIV correlations (Meinhart, Wereley, and Gray 2000) --- was large in this case, more than 6 μm or 24% of the channel depth. The large measurement depth combined with the low particle seeding density facilitated the use of two frame μPIV at the expense of spatial resolution and fluorescence signal level. The effective μPIV measurement depth is inversely dependent on the numerical aperture (*NA*). For

this reason, high NA objectives are typically used to obtain thinner measurement depths, resulting in less axial spatial averaging. Thinner measurement depths and the desire for high vector spatial resolution require higher particle volume fractions in order to meet minimum particle per interrogation window constraints. Larger particle volume fractions increase the image contributions from out of focus particles which reduce the signal to noise ratio of the PIV correlations (S/N) and increase the number of erroneous vectors. Additionally, the higher the *NA* of the objective, the more particles are out of focus, therefore the more out of focus light exists which impacts the correlations. In this way, the *NA* of the imaging system is coupled to the particle volume fraction.

A novel spinning disk system (not a Nipkow confocal disk) has been used to record micro PIV measurements at different focal planes at high speeds (Angele et al. 2006). The disk consists of sectors with glass of various thicknesses and therefore different optical path lengths such that the disk alters the focal plane of the microscope objective. This enables the focal plane of the microscope to be changed rapidly as the different sectors of the glass are passed through the field of view. Angele et al. measure unsteady flow at a 3D scan frequency of 100 Hz, however are limited to low NA and large working distance objectives due to the physical constraints of the spinning disk lens system. Also this system measures only 2 components of the velocity.

Confocal imaging optically sections the flow, reducing noise from out of focus particles. In Nipkow disk based imaging systems both the excitation and emission light pass through the pinhole array. This results in large losses because

the pinholes must be small and spaced relatively far apart to achieve confocality. In fluid flow velocimetry, the motion of the flow tracing particles should be frozen requiring either short laser illumination pulses or short imaging integration times, both of which require high instantaneous light intensity. Increasing the power of the illumination source is the most straightforward method to obtain adequate light intensity of the particles and is suitable until the damage threshold of the optics in the system is reached. High quantum efficiency, low noise cameras can also be used, but often these systems are limited to low video frame rates. Another solution, implemented by Tanaami et al., is the addition of a second disk in series with the Nipkow disk containing microlenses that focus the excitation light through the pinholes of the disk (Tanaami et al. 2002). The microlens solution is available commercially from Yokogawa Electric Corporation.

Studies have been conducted to quantify the improvement in measuring steady velocity profiles provided by the optical sectioning of a spinning disk confocal system for μPIV (Park et al. 2003; Park, Choi, and Kihm 2004; Park and Kihm 2006). Park et al. showed that pressure driven flows in cylindrical microtubes measured by ensemble-averaged, confocal based μPIV resulted in better agreement with analytical solutions as compared to widefield μPIV. They conclude that the confocal system greatly improves image contrast by eliminating the contributions of out of focus particles and resolves the velocity field with improved axial spatial resolution because it optically sections the flow, reducing the effects of depth averaging on the velocity measurement.

There have been several papers published in the area of high speed confocal PIV. Lima et al. constructed a high speed confocal μPIV system to obtain detailed measurements of blood cell suspension fluid in a square microchannel. Ensemble averaged and two frame instantaneous velocity profiles were compared for Poiseuille flow using pure water as well as physiological fluid with suspended blood cells (Lima et al. 2006; Lima et al. 2007). Additionally, Lima et al. compared instantaneous confocal PIV profiles for pure water and physiological fluid with hematocrit (Lima et al. 2007). In the supplemental information of this work they include an analysis of the improvement in image signal to noise ratio as well as suggest that the confocal system may provide more distinct correlation peaks. Their system was constructed to capture data at up to 2000 Hz, but was only used at 200 Hz due to limited light levels. Lima et. al used a similar system to measure 2 components of velocity in a 3 dimensional volume (3D2C) for pressure driven flow of both physiological saline and physiological fluid with suspended blood cells and 20% hematocrit (Lima et al. 2008). Recently, confocal μPIV measurements have been made of the velocity field surrounding a microorganism during feeding (Nagai et al. 2009). These measurements were made at various focal planes around the organism at 400 fps and ten instantaneous flow fields were averaged to obtain the average velocity at each height.

Typical μPIV and μPTV systems obtain images of particles in a 3D volume projected onto a 2D plane (CCD or CMOS sensor), and cannot resolve the out of plane position of the particles accurately. To improve the ability of μPIV and μPTV to measure 3D3C microflows, new algorithms and experimental setups that

utilize information in these projected images can be used, or techniques that scan and image the entire microvolume can be used. Stereoscopic, defocusing, and interferometric methods can extract the third component of velocity from projected 2D images. Stereoscopic μPIV and μPTV (Bown, MacInnes, and Allen 2007; Bown et al. 2006; Lindken, Westerweel, and Wieneke 2006) use a stereomicroscope to obtain images of the flow at two perspectives. Stereoscopic methods determine three components of velocity through, sometimes difficult, calibration of the two perspectives (Lindken et al. 2005). The measurement volume is restricted to the overlapping depth of field of the two objectives, so depth scanning is required to resolve the third dimension for samples deeper than the depth of field. The low numerical aperture of stereo microscopes ($NA \sim 0.3$) results in reduced spatial resolution as compared with inverted epifluorescence microscopes ($NA \geq 1$). Hajjoul et al. demonstrated another stereoscopic μPTV technique, where multiple viewpoints of the particles are acquired using V-shaped micromirrors embedded in the floor of the microchannels (Hajjoul et al. 2009). They used the system for intracellular imaging in living cells. The system was demonstrated for a low number of tracer particles, indicating low spatial resolution..

Defocusing PTV methods determine the out of plane velocity component by tracking the defocused particle image patterns. As the particles translate away from the focal plane, their diameter grows and their brightness decreases due to the point spread function (PSF) of the microscope objective. If the focal plane is set to one side of the measurement volume, this effect can be used to determine

the out of plane velocity (Peterson, Chuang, and Wereley 2008; Park and Kihm 2006). One defocusing technique proposed by Pereira and Gharib et al. uses a mask with three apertures in a triangular pattern placed in the back focal plane of the microscope objective. Each physical particle generates three particle images (Pereira and Gharib 2002; Kajitani and Dabiri 2005). Kajitani and Dabiri derived equations relating the distance between the three images of each particle to the distance of the physical particle from the focal plane (Kajitani and Dabiri 2005). Yoon and Kim applied the same technique to a microfluidic system using a calibration technique (Yoon and Kim 2006). The method developed by Cierpka et al. tracks particles in the axial depth direction using a cylindrical lens placed in front of the camera sensor (Cierpka et al. 2010). The cylindrical lens alters the position of the focal plane of the system in one dimension only, elongating the particles in that direction. The method uses a calibration that relates the elongated particle images to their depth. They demonstrate the method using large (5 μm diameter - 20x magnification) particles at a low volume fraction, so the spatial resolution was limited. In general, defocusing methods work best at low volume fractions, and have problems at high particle volume fractions where the tracer images overlap.

Holographic μPTV uses interference fringes to determine the out of plane positions of particle tracers (Sheng, Malkiel, and Katz 2006; Kim and Lee 2007). Interference fringes occur when coherent light scattered from tracer particles laser light interferes with the unscattered coherent beam. Diffraction theory fits to the measured fringes can determine the particle's position, size, and index of

refraction (Cheong et al. 2009). Although the technique is able to measure 3D3C flows accurately, the computation times are long and the particle volume fraction is limited because the fits become difficult to determine when fringes of neighboring particles overlap (Ooms, Lindken, and Westerweel 2009).

Depth scanning techniques determine 3D3C velocity fields by acquiring 2D images at multiple depths and combining them into a 3D image to image the entire volume, as opposed to the previously mentioned techniques that use 2D projected images. Several research groups use depth scanning to characterize 3D colloidal crystals (Weeks et al. 2000; Dinsmore et al. 2001; Prasad, Semwogerere, and Weeks 2007; Jenkins and Egelhaaf 2008; Besseling et al. 2009; Dinsmore and Weitz 2002). Recent works acquire three-dimensional stack images using an electronically controlled *z*-stage or microscope positioner. The highest reported 2D acquisition rate is around a few hundred frames per second, and 3D acquisition rates are typically not reported (Besseling et al. 2009; Prasad, Semwogerere, and Weeks 2007). Particle tracking algorithms determine the particle centers from these 3D images and track the particles in time (Crocker and Grier 1996).

Kinoshita et al. used similar depth scanning techniques to measured the 3D internal flow in a moving droplet using spinning disk confocal PIV and depth scanning (Kinoshita et al. 2007). They inferred the out of plane velocity from a series of phase-locked two component velocity measurements at multiple focal planes and the continuity equation. This specific technique is not applicable to nonstationary flows because it uses phase-locked ensemble averages in

correlation space across many droplets. Raffel et al. introduced a dual plane PIV technique for determining 3D3C velocity fields in macroscopic laser-sheet-PIV (Raffel et al. 1996). In this method, two depth-separated light sheets determine the out of plane displacement of the particles using the ratio of the correlation peak heights between the images. Shinohara et al. adapted dual plane PIV to volume illumination in microscale flow fields by replacing the light sheet thickness with the depth of field of the objective (Shinohara et al. 2005). Erkan et al. used this method to measure the 3D2C time averaged pressure driven flow in a microchannel (Erkan et al. 2008). The error in the measurements can be as high as 40% due to background noise effects. Techniques to remove background noise are not viable with this technique because it depends on the out of focus particle images to determine the out of plane displacements.

In scanning 3D applications, some data may be missing from the flow field if the scan is not contiguous. In this case, the missing data between the scanned planes can be estimated using interpolation. Adaptive control grid interpolation (Frakes et al. 2004) and modified adaptive control grid interpolation (Frakes et al. 2008) can be used in these cases to recover the full flow field. Modified control grid interpolation has been shown to be useful for PIV and PTV data (Frakes et al. 2008).

1.3. Research Goals and Impact

This dissertation presents a diagnostic for high-speed and 3D velocimetry based on spinning disk confocal microscopy and depth scanning of a microvolume. High-speed 2D unsteady velocity fields are resolved by acquiring

images of particle motion using a high-speed CMOS camera. A confocal microscope spatially filters out of focus light using a rotating disk of pinholes placed in the imaging path. The confocal disk improves the ability of the system to resolve unsteady μPIV measurements by improving the correlation signal to noise ratio. A piezo-actuated objective positioner quickly scans the depth of the microvolume and collects 2D image slices, which are then assembled into 3D stacked images and interrogated using PIV and PTV algorithms. The technique allows for isosurface visualization of time resolved 3D particle motion and high spatial resolution velocity measurements without requiring a calibration step or reconstruction algorithms.

The first part of this work is the design and characterization of the system itself. The main system components include a high power laser for illumination, spinning disk confocal system, inverted microscope, piezo-actuated objective positioner, and high-speed CMOS camera, as well as timing equipment for synchronization of the piezo and camera. These system components are characterized and the synchronization process discussed.

The second phase is an investigation of the improvement that the confocal system grants to the measurement of high speed, unsteady flows. I present an analysis of the percent erroneous vectors for the confocal system compared to a traditional micro PIV system for two-frame correlations as a function of particle volume fraction and focal depth. As a demonstration of the ability of the confocal system to measure two-frame micro PIV velocity fields, the confocal system

measures the unsteady flow in an electro kinetic instability with 400 μs temporal resolution.

Next, I use the confocal system and a piezo actuated objective positioner to obtain 3D3C volumetric velocity measurements. Super resolution μPIV interrogates 3D images of the flow tracers using μPIV as a predictor field for tracking individual particles with μPTV. I derive equations to predict the limits of parameters of the system using relevant relations from the literature adapted for the scanning of the objective. The 3D3C velocity field in an expanding microchannel validates the method. Experimental 3D3C velocimetry data acquired at 30 Hz with instantaneous spatial resolution of 4.5 by 4.5 by 4.5 μm agrees well with a computational model of the 3D3C flow field. Finally, I utilize the 3D confocal system to briefly investigate the time resolved structure of isotachophoresis plugs and the 3D3C diffusiophoretic motion of particles assembling on a copper substrate.

I expect the successful completion of my research goals will improve knowledge of the capabilities of the hardware used for 3D3C temporally resolved velocimetry and provide the design and characterization of a system that enables researchers to investigate their complex 3D3C microflows. The findings in this document will advance the development of 3D3C velocimetry measurements by characterizing the various parameters important to the design of a high speed scanning confocal system using a piezo actuated objective positioner. Potential applications of the temporally resolved 3D3C confocal velocimetry system include the characterization of flow fields in microdevices, as well as

visualization of other microchannel based systems such as isotachophoresis plugs and the time resolved measurement of fluorescently labeled cell motion.

Contributions to the scientific community include two articles published in Measurement Science and Technology. The first article is on the improvement to two frame velocity measurements granted by the confocal system, and the second on the 3D3C scanning micro velocimetry system. The development of this imaging system has led to two collaboration collaborative works. The first collaboration involved investigations into the 3D structure of isotachophoresis plugs and was conducted with Giancarlo Garcia, Moran Bercovici, and Juan Santiago at Stanford University. The second collaboration involved the application of the confocal system in addition to new correlation methods, termed the robust phase correlation method, with Jaime Schmeig and Pavlos Vlachos at Virginia Tech.

CHAPTER 2

BACKGROUND

2.1. PIV and PTV

Two common techniques for experimental velocity measurements include micro particle tracking velocimetry (μPTV) and micro particle imaging velocimetry (μPIV) (Adrian 1991; Adrian and Yao 1985). Both methods use tracer particles to track fluid motion. Typically, fluorescent particles are used to enhance the contrast of the images, where inline filter sets only allow fluorescent light collected from the particles to reach the camera. PIV is one of the most useful techniques for determining velocity fields experimentally in most fluidic systems (Adrian 1991). It is used in both industry and academia extensively for a variety of flows. Micro PIV is more common method than μPTV for determining velocity fields, often yielding more robust data (and requiring higher particle volume fractions), but both methods have their niches in this respect. Micro PTV can track the motion of individual particles where the particles are the objects of interest rather than the fluid flow. The motion of individual particles is important for applications such as colloidal crystal formation and cell/bacteria tracking in biological systems.

In PIV, tracer particles are seeded into the flow of interest and the displacement of the particles between two exposures is determined using cross correlation algorithms in user-defined interrogation windows (Adrian and Yao 1985). The Lagrangian velocity estimator is then used to approximate the Eulerian fluid velocity, where the seeding particles are generally assumed to

follow the motion of the flow (Adrian 1991). Micro particle imaging velocimetry uses volume illumination and a microscope to image particles instead of a laser light sheet and camera lens (Santiago et al. 1998; Meinhart, Wereley, and Santiago 1999).

PTV tracks individual particles to create particle trajectories that can visualize fluid or particle motion. PTV algorithms first find the particle centroid, usually using the center of mass technique, then connect the particle centers in each frame together according to the likelihood that they belong to the same particle (Prasad, Semwogerere, and Weeks 2007). The simplest likelihood algorithm searches radially around each particle center to find the closest particle in the next image. Therefore, as the displacement of the particles between frames approaches the mean center-to-center distance between particles, the tracking becomes difficult and eventually impossible. This limitation on particle volume fraction is one of the limitations of PTV. However, because each particle is tracked individually, PTV is well suited for applications where the particles themselves are the object of interest rather than the flow field. Additionally, PTV works better than PIV for situations in which the particle volume fraction must be low. Another benefit is that whereas PIV can produce only one vector per interrogation window (which usually consists of several pixels in x, y, or z), PTV can provide a velocity vector for each location that the particle center travels through (Takehara et al. 2000). This can help to determine velocities in scanned 3D flows where the resolution in the depthwise direction is typically limited. Advanced tracking algorithms use iterative methods where tracking is repeatedly conducted with the displacements

determined from the successfully tracked particles removed in each iteration, or so called super-resolution algorithms which use PIV for a coarse velocity estimate and then track individual particles using PTV to improve the spatial resolution of the measurement (Besseling et al. 2009). Confocal systems can allow particle centers to be more accurately determined, and remove light from out of focus particles. As such confocal systems are often used in PTV measurements of non-dilute colloidal suspensions (Prasad, Semwogerere, and Weeks 2007).

2.2. Theory of Confocal Imaging for PTV and PIV Measurements

Imaging properties of optical microscopes can be described in terms of the point spread functions (PSF) of their optics. The point spread function is a 3-D diffraction pattern that is observed when imaging objects near the wavelength of visible light. Generally, the PSF depends on the numerical aperture (NA), wavelength of illuminating light λ_{em}, and index of refraction of the object being imaged (n). The 3-D intensity distribution created by a lens near its focal plane has been derived by Born and Wolf (Born and Wolf 1997) with corrections made by Carlsson et al (Carlsson and Aslund 1987). The paraxial approximation is used here, which assumes that the half angle (α) of light rays are shallow such that $\sin(\alpha) \sim \alpha$, also known as first order or Gaussian approximation (Hecht and Zajac 1974). The following uses some other approximations and for a full treatment of the derivation please see the text by Born and Wolf (Born and Wolf 1997). In short, using transformed radial and axial coordinates:

$$u = \frac{8\pi nz}{\lambda}\sin^2(\frac{\alpha}{2}) \quad (1)$$

$$v = \frac{2\pi nr}{\lambda}\sin(\alpha) \quad (2)$$

where α is the half angle of the lens, *r* is the radial direction spatial component, and *z* is the axial direction spatial component. Using these normalized optical variables, the 3D point spread function of the microscope can be described in terms of a convergent series of Bessel functions called Lommel functions :

$$U_n(u,v) = \sum_{s=0}^{\infty}(-1)^s \left(\frac{u}{v}\right)^{n+2s} J_{n+2s}(v) \quad (3)$$

$$V_n(u,v) = \sum_{s=0}^{\infty}(-1)^s \left(\frac{v}{u}\right)^{n+2s} J_{n+2s}(v) \quad (4)$$

The above functions can be implemented to obtain the 3-D PSF near the focus of a microscope, with derivation carried out in Born and Wolf:

$$I(u,v) = \left(\frac{2}{u}\right)^2 \left[U_1^2(u,v) + U_2^2(u,v)\right] I_o \quad for \quad \frac{u}{v} < 1 \quad (5)$$

$$I(u,v) = \left(\frac{2}{u}\right)^2 \left\{ \begin{array}{l} 1 + V_0^2(u,v) + V_1^2(u,v) \\ -2V_0(u,v)\cos\left[\frac{1}{2}\left(u + \frac{v^2}{u}\right)\right] - 2V_1(u,v)\sin\left[\frac{1}{2}\left(u + \frac{v^2}{u}\right)\right] \end{array} \right\} I_o \quad for \quad \frac{u}{v} > 1 \quad (6)$$

$$I_0 = \left(\frac{\pi a^2 |A|}{\lambda f^2}\right)^2 \quad (7)$$

where *A/f* is the amplitude of the incident light, *f* is the focal length of the lens, and a is the radius of the aperture. The intensity distribution in the axial direction and the focal plane can be found by setting *v* and *u* to 0, respectively, and then

simplifying. Following Born and Wolf, using the paraxial approximation, a non-dimensionalized axial spatial variable *u*, and a non-dimensionalized lateral (parallel to focal plane) radial spatial variable *v*, the PSF along the optical axis is found to be (Born and Wolf 1997),

$$I(u,0) = \left(\frac{\sin(u/4)}{u/4} \right)^2 I_o \qquad (8)$$

where I_o is the intensity at the focal plane. This means that the intensity of the point spread function along the axis of a lens is essentially a squared sinc function.

In a confocal microscope, a pinhole is placed in a conjugate focal plane to the focal plane of the microscope objective. This pinhole, or aperture, reduces the amount of out of focus light that reaches the detector by spatially filtering light from out of focus planes. This setup is depicted in Figure 1. The green lines symbolize the incident radiation and the red lines symbolize the collected radiation (fluorescent). The blue lines symbolize the out of focus emission light that originates from outside the focal plane. This out of focus light is unfocused when it reaches the pinhole plane and is therefore mostly blocked, whereas the in-focus light passes through the pinhole. A confocal microscope such as the one depicted in Figure 1 also requires some method of scanning the field of view, since it only images one point at a time. This can be achieved by using a stage scanner, Nipkow disk, or some other scanning method.

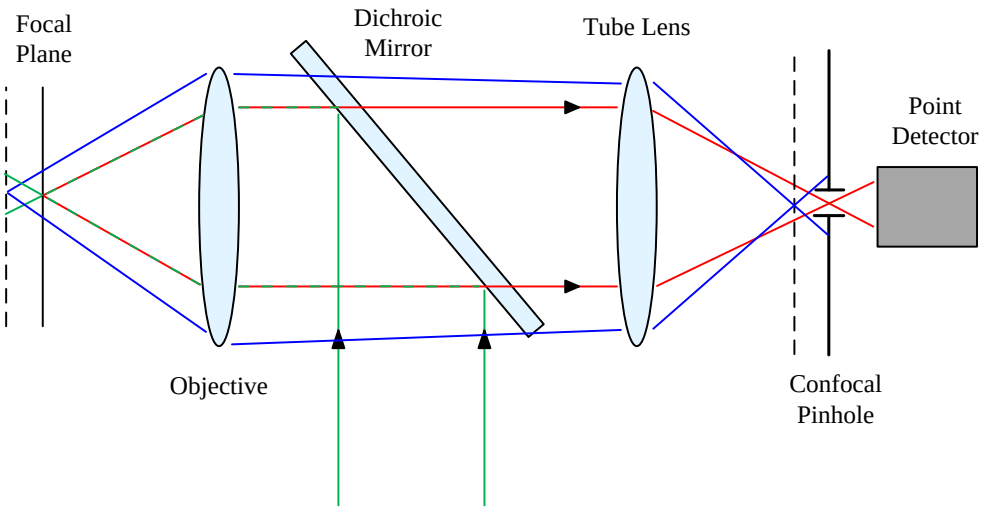

Figure 1. Depiction of simple single pinhole confocal imaging system. The green lines symbolize the incident radiation and the red lines symbolize the collected radiation (fluorescent). The blue lines symbolize the out of focus emission light that originates from outside the focal plane. This out of focus light is unfocused when it reaches the pinhole plane and is therefore mostly blocked, whereas the in-focus light passes through the pinhole.

In a confocal system, if the same optics are used for illumination and emission, the PSF can be approximated, using the assumptions above and ignoring the geometric-optical effects of the pinhole, by the square of (8) (Sheppard and Wilson 1978). A physical way to think of this is that in a confocal system, both the incident and collected light are reduced to a diffraction limited spot by the pinhole (Carlsson and Aslund 1987). In image space the resulting PSF is the product of the incident and collected PSF's by the convolution theorem. The axial PSFs for confocal and widefield systems are plotted versus u/π in Figure 2. It is evident that in the confocal system compared to the widefield, the secondary maxima are decreased and the width of the central peak is decreased. However, this does not take into account the geometric effects caused by a finite sized pinhole.

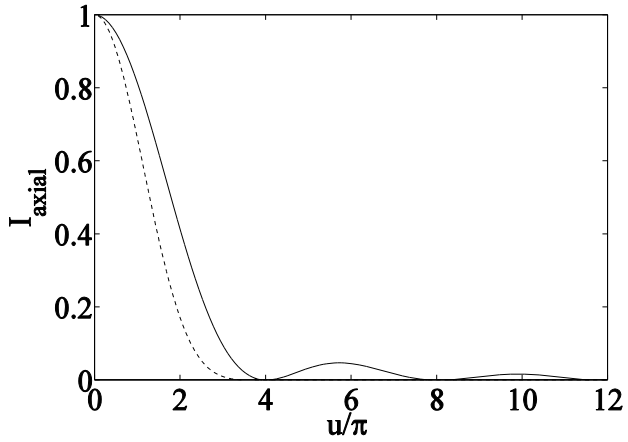

Figure 2. Theoretical axial point spread functions for widefield (solid line) and confocal (dotted line) systems with an infinitely small pinhole. Intensity profile is sharper in the case of the confocal system, with reduced sidelobes.

Confocal microscopes provide improved depth and lateral resolution to microscopic imaging and also remove light from planes outside the depth of field of the objective by changing the point spread function (Sheppard and Choudhury 1977; Sheppard and Wilson 1978; Corle, Chou, and Kino 1986; Kino and Corle 1989; Xiao, Corle, and Kino 1988). The 3D PSF in a confocal system with a pinhole size that is much smaller than the airy disk diameter can be estimated by the square of (5) - (7) (Sheppard and Wilson 1978). These equations are discretized and squared and then plotted. Figure 3 shows the effect of adding an infinitesimally small pinhole (squaring of the intensity distribution function) on the 3D intensity profile for the microscope (at the center of the focal plane) both as a surface plot and a contour plot.

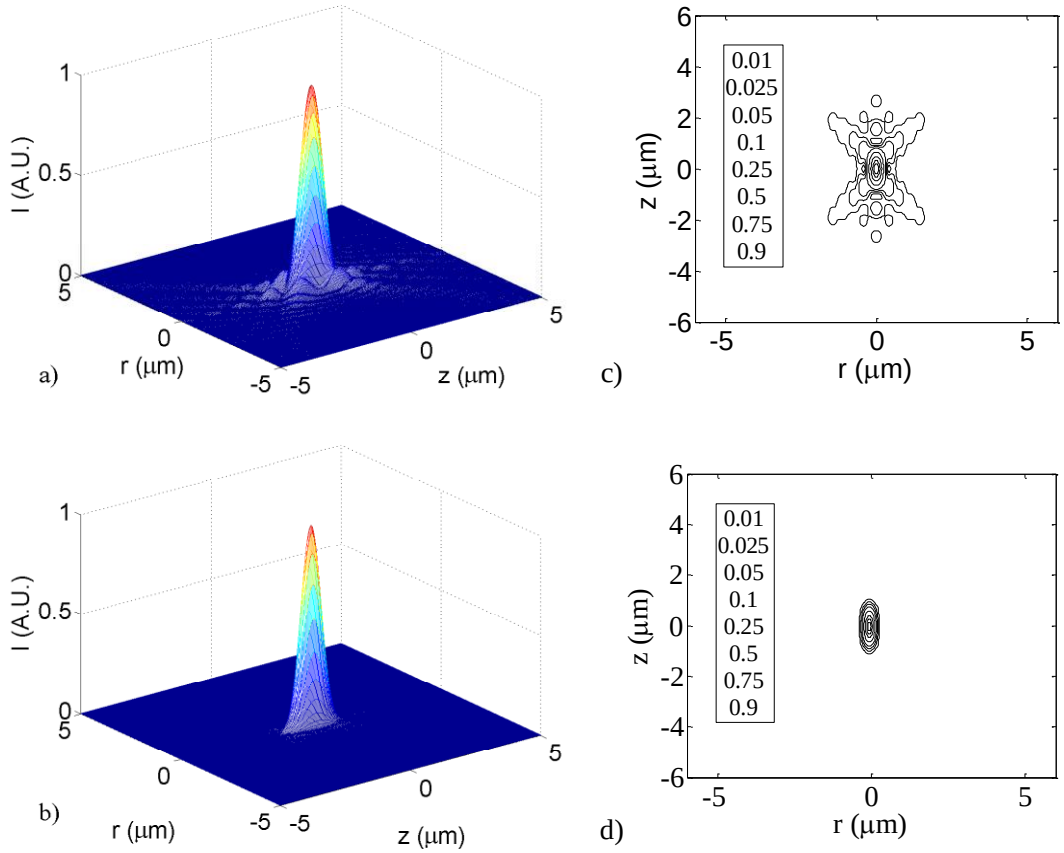

Figure 3**.** 3D point spread function simulation for widefield (a,c) and confocal (b,d) with pinhole diameter << 1 *AU*. Note that the sidelobes are barely visible in the confocal PSF while they are fairly prominent in the widefield PSF. These sidelobes are what create the "wings" often seen in *x*-z projections of particles and the Airy rings seen in *x*-y images**.**

The image of a tracer particle for μPIV can be estimated by convolving the PSF with a sphere of the diameter of the particle. Figure 4 shows the theoretical image of a 3 μm sphere using both confocal and widefield microscopes.

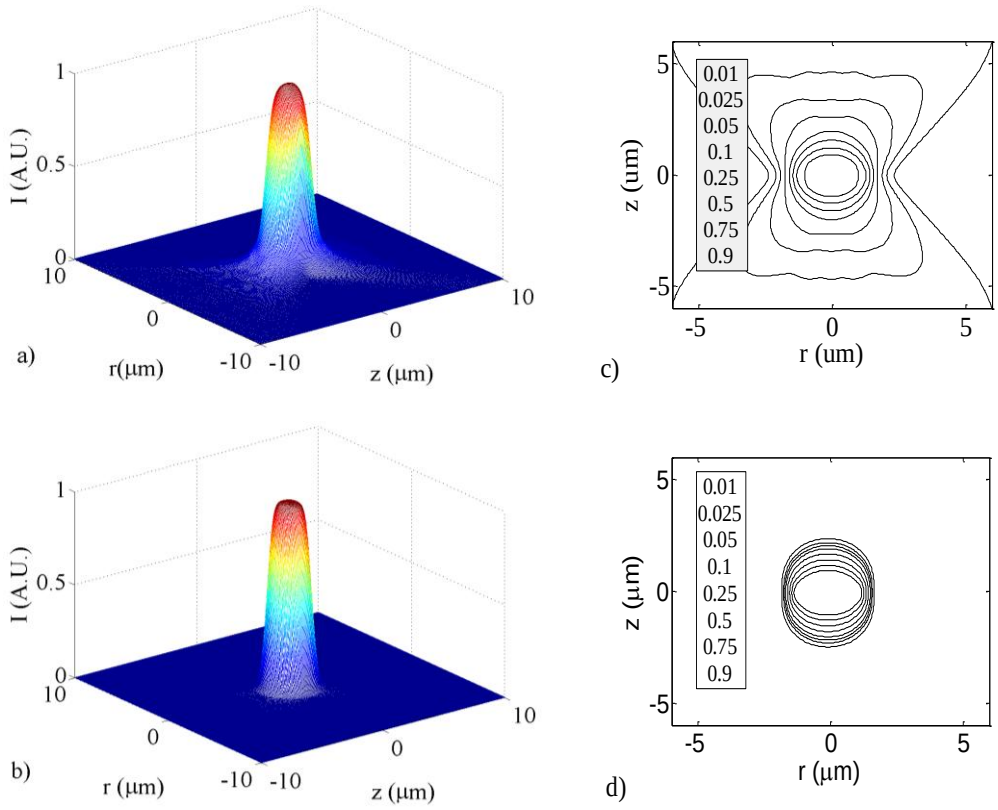

Figure 4. 3D intensity profile simulation for image of 3 μm sphere using widefield (a,c) and confocal (b,d).

Note that the images of a sphere convolved with the PSF's of the confocal and widefield systems resemble the experimental data collectecd in Figure 5. However, these theoretical predictions do not take into account the fact that the pinhole in the confocal system in this work is larger than one airy unit *(AU)*, defined as $1.22\lambda_{ex}/NA$ (the full width of the first minima of the radial PSF), where λ_{ex} is the wavelength of the illuminating light (Wilhelm et al. 2003). Therefore, it is useful to compare the theoretical predictions with experimental measurements to determine the true effect of the confocal system on images of particles. Images of a 3 μm diameter fluorescent polystyrene bead were acquired in using the 3D confocal disk system with the disk both in and out of the light path. Figure 5

shows the *x*-*z* projection of the sphere. Notice that even though the pinhole is 2x the Airy disk diameter for this confocal system, the "wings" present in the widefield projection are nearly absent in the confocal system. It is clear that the confocal system creates a more accurate image of the sphere with reduced diffraction effects. The cumulative blurring caused by these diffraction effects, when summed up from many particles in a non-dilute colloidal suspension, can prevent techniques such as PIV and PTV from accurately measuring particle motion by increasing the background intensity level and obscuring images of in focus particles. Additionally, the intensity profile along the center of the bead is shallower for the confocal compared to the widefield system as shown in Figure 5c. This shows that the pinhole need not be very small (<< 1 Airy disk diameter) to remove a substantial amount of out of focus light.

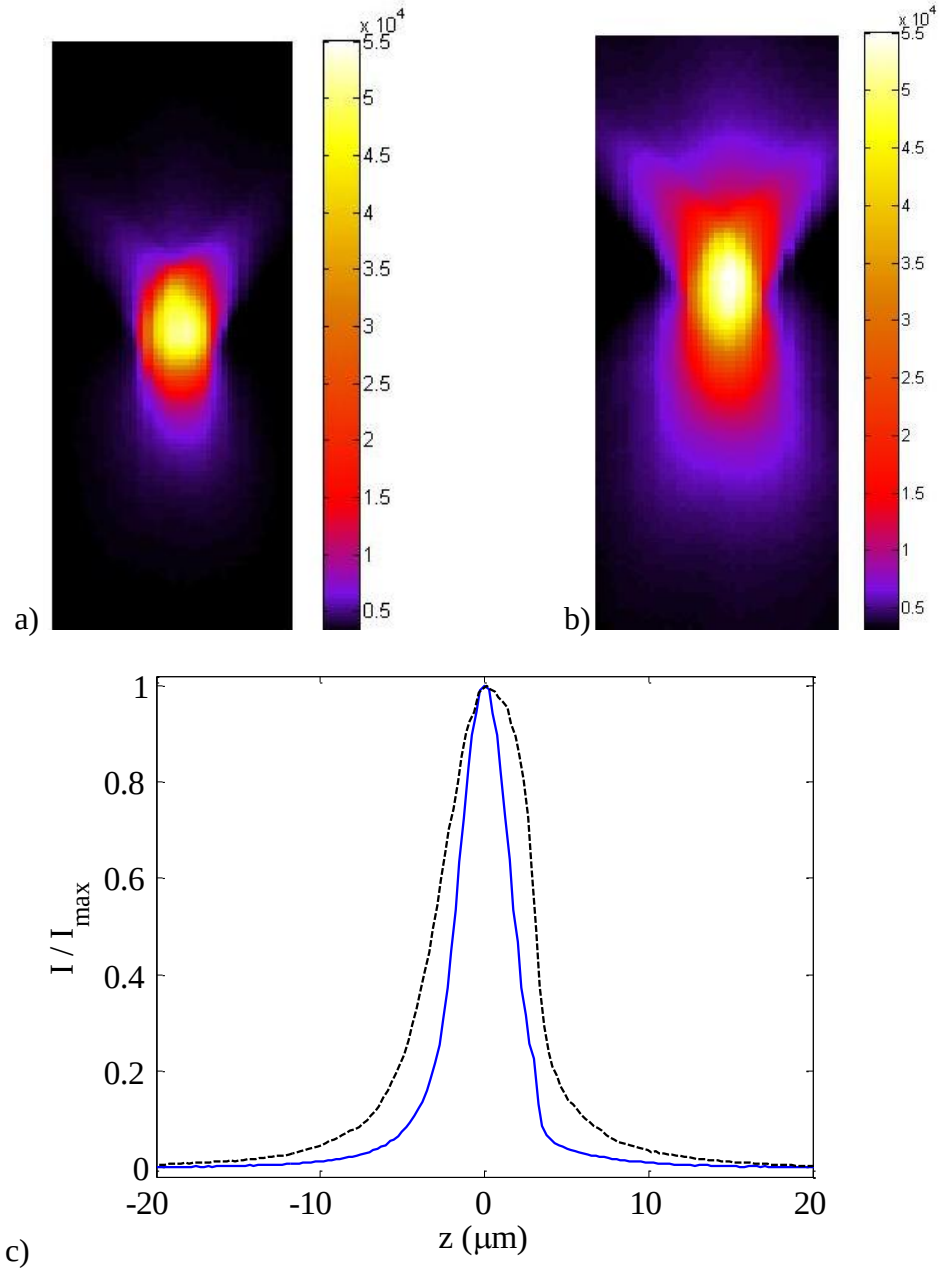

Figure 5. *X-Z* cross section of 3 μm polystyrene bead, (a) in confocal mode and (b) in widefield mode. Image scaling, emission intensity, and equipment are the same for (a) and (b). It is clear that the confocal system creates a more accurate image of the sphere with reduced diffraction effects. c) Intensity in depth direction along the center of the tracers, with the blue line showing confocal and dashed black line showing widefield.

The depth of field (DOF) is a term used to describe the distance in object space in the axial direction over which the microscope is acceptably in focus (Inoue and Oldenbourg 1994). In microscopy, the DOF is usually defined as ¼ of the axial distance between the first minima above and below the focal plane of the axial PSF, plus a geometric optical term that depends on the detector resolution (Inoue and Oldenbourg 1994),

$$DOF = \frac{\lambda_{em} n}{NA^2} + \frac{n}{MNA} e \qquad (9)$$

where M is the magnification of the objective, and e is the minimum resolvable distance on the detector (size of one pixel for modern digital cameras). The first term in this equation is also sometimes called the wave-optical depth of field. The second term is a measure of the spreading of the image over a pixel. Wilhelm et al. have developed a similar expression to the DOF for confocal microscopy that takes into account the finite size of the pinhole. This equation is called the optical sectioning thickness (OST) and is given in terms of the full width half maximum (FWHM) of the PSF, meaning the full width of the central peak at the point where the intensity reaches 50% of the in focus intensity, with an additional contribution from the geometrical optics of the pinhole (Wilhelm et al. 2003),

$$OST = \sqrt{\left(\frac{0.88\lambda_{em}}{n - \sqrt{n^2 - NA^2}} \right)^2 + \left(\frac{\sqrt{2} n \cdot PD}{NA} \right)^2} \qquad (10)$$

where PD is defined as the physical pinhole diameter divided by the magnification. It is important to note that Equation 4 is only valid when PD is

greater than the first diameter of the Airy Disk, or one Airy Unit (*AU*). Additional expressions developed by Wilhelm et al. describe the OST for $PD < 1$ *AU*. As shown by Wilson et al. the depth discrimination of a microscope is not very dependent on pinhole size for pinholes near 1 *AU* in size (Wilson and Carlini 1987, 1987). This, combined with the loss of light that occurs as the pinhole diameter is decreased below 1 *AU*, causes most confocal fluorescence microscopes to be designed with pinhole diameters > 1 *AU*. I will therefore not discuss confocal systems with pinhole diameters below 1 *AU* here.

It should be noted that the diffraction term in (9) (first term) is defined essentially as the full width of the axial PSF at approximately 80% of the in focus intensity, whereas the diffraction term in (10) is defined as the full width of the axial PSF at 50% of the in focus intensity. Contrary to some published articles, although the DOF and the OST both measure the full width of the axial PSF at a certain decay intensity with additional geometric terms, they cannot be used to directly compare the 'sectioning' ability of confocal and widefield microscopes because they are developed for different decay points of the PSF.

The OST and DOF are useful expressions for quantifying the depth over which light contributes usefully to the image of a point source; however the most important advantage of the confocal system for μPIV is the removal of out of focus light by the confocal system, which compensates for the noise caused by volume illumination (Park, Choi, and Kihm 2004). Sheppard and Wilson analytically derived the expressions for the integrated intensity (total intensity at a plane conjugate to the focal plane) of a point source for confocal and widefield

microscopes, which can be used as a measure of the depth discriminating power of an imaging system. They found, as expected from conservation of energy, that the integrated intensity for a widefield system is constant for every plane perpendicular to the optical axis. However, for a confocal system the integrated intensity was found to decrease monotonically with distance from the focal plane, establishing the confocal system's ability to remove light from the illuminated volume (Sheppard and Wilson 1978).

The μPIV measurement depth (Meinhart, Wereley, and Gray 2000) and μPIV depth of correlation (Olsen and Adrian 2000; Bourdon, Olsen, and Gorby 2006) are two expressions for the depth over which particles contribute to the correlation function. Both the measurement depth and depth of correlation are generally larger in magnitude than the DOF and FWHM of the microscope, and take into account the geometric effects caused by the finite size of the tracer particles as well as their point spread functions. These two expressions are derived differently from each other but describe the same phenomenon, which is that particles still contribute to μPIV correlations even outside the traditionally defined DOF.

The depth of correlation is defined as distance from the focal plane over which a particle contributes meaningfully to the PIV correlation. The depth of correlation for μPIV is given in (11) (Bourdon, Olsen, and Gorby 2006). It should be noted that there have been several papers published with modifications to (11) to account for Brownian motion, in and out of plane shear, etc.

$$z_{corr} = 2\left\{\frac{1-\sqrt{\varepsilon}}{\sqrt{\varepsilon}}\left[\frac{n^2 {d_p}^2}{4NA^2} + \frac{5.95(M+1)^2\lambda^2 n^4}{16M^2 NA^4}\right]\right\}^{1/2} \qquad (11)$$

where ε is the threshold weighting function value where the particles are no longer considered to contribute to the velocity field (usually 0.01), n is the index of refraction of the immersion medium of the objective, d_p is the particle diameter, NA is the numerical aperture of the objective, M is the magnification, and λ is the wavelength of the collected radiation.

The μPIV measurement depth is a similar expression. It is defined as the depth over which a particle contributes to uPIV cross correlations. It is found to be equal to twice the depth at which a particle reaches one tenth of it's in focus intensity (Meinhart, Wereley, and Gray 2000). An analytical estimate of this distance is given by the following expression:

$$\delta z_m = \frac{3n\lambda_0}{NA^2} + \frac{2.16 d_p}{\tan\theta} + d_p \qquad (12)$$

where $tan\theta$ is the tangent of the light collection half angle (reported above as α), and λ_0 is the wavelength of the collected radiation. The first term is a diffraction term, derived from the point spread function equations of Born and Wolf. The second term results from geometrical optics considerations as the particles move away from the focal plane, and the third term is the physical particle diameter. Experimental measurements of the measurement depth of the confocal and widefield systems used in this work are presented in section 3.4.

This chapter reviewed some existing literature and developed original figures to help describe the imaging properties of confocal microscopes, and how these properties relate to PIV and PTV measurements. Interesting future work in this area would be to develop analytical expressions to predict the confocal depth of correlation and/or confocal measurement depth. Some modeling of confocal measurement depth and depth of correlation is shown in section 3.4. However, no concise analytical relationships were developed. Existing literature on confocal PIV typically relies on experimental measurements as a substitute for these relationships, or incorrect comparisons that attempt to predict depth of correlation for confocal PIV and PTV.

CHAPTER 3

EXPERIMENTAL SYSTEM

In this chapter, the experimental system of a diagnostic for measuring 2D high-speed unsteady 2D microflows, and unsteady 3D3C microflows is presented. First, an overview of the components and general working of the system is given. This is followed by detailed measurements and characterizations of the important system components: the laser, CMOS camera, confocal disk, and timing equipment. Finally, equations are derived that predict the limits of parameters for the 3D3C measurements presented in Chapter 5. Although portions of this chapter are specific to the 3D3C measurements, the same system is used in Chapter 4 for measurements of unsteady 2D velocity fields.

3.1. Experimental Setup

In this section, the experimental setup for the volumetric micro particle velocimetry system is detailed. The system is described from the standpoint of 3D3C super resolution micro PIV as in Chapter 5; however, in Chapter 4 the same system is used for high-speed 2D2C measurements. The method described here determines 3D3C velocity fields at the microscale using super resolution confocal PIV and a piezo actuated objective positioner. The objective positioner displaces the objective along its optical axis, altering the focal plane as it does so. Images of tracer particles are acquired as the objective displaces. Particles are in-focus when their out of plane position lies within the depth of field (Inoue and Oldenbourg 1994) of the objective. The confocal system removes much of the light outside the depth of field, and the system scans the depth quickly, acquiring

many 2D images (slices) that are assembled into a 3D volumetric image or stack as shown in Figure 6b. Figure 6a shows how the slices are overlapped in the depthwise direction. The interslice spacing must be ≤ than the full width half maximum (FWHM) of the imaging system to fulfill the Nyquist sampling criterion (the system should sample twice as finely as information might exist) (Wilhelm et al 2001). The FWHM is the full width of the point spread function at 50% of the in focus intensity.

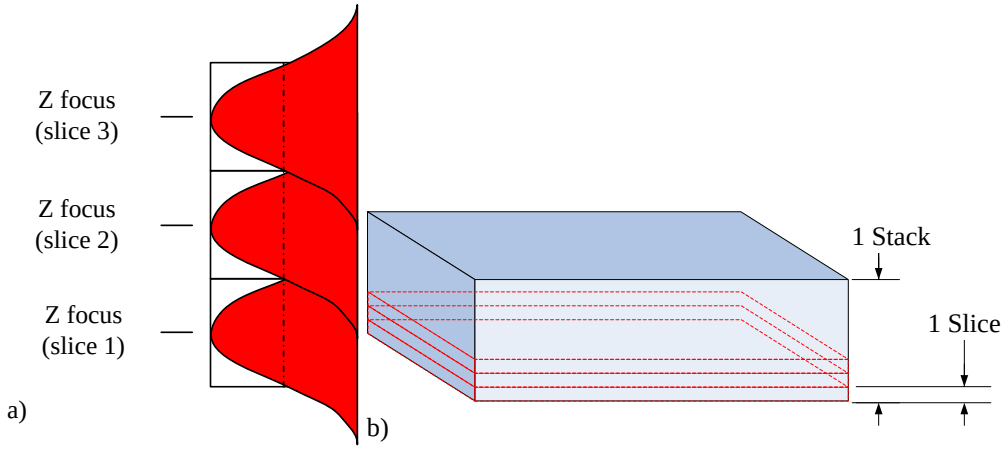

Figure 6. Schematic illustrating acquisition of 3D image stacks. (a) The maximum slice spacing should correspond to the full width half maximum of the point spread function of the imaging system from the Nyquist Criterion. (b) A stack is a 3D image made up of multiple slices.

The components of the 3D3C time resolved micro velocimetry system are the epifluorescent microscope, confocal system, laser, CMOS camera, piezo actuated objective positioner, and timing equipment. Figure 7 shows a schematic of the experimental setup. The specific components of the epifluorescent microscope include the microscope main body (TE2000, Nikon, Japan), a 60x water immersion (NA = 1.20) objective (MRD07601, Nikon), a 1.2 watt λ_{ex} = 532 nm diode-pumped solid-state (DPSS) laser (LLS 532-TH-1000, LaserGlow, Canada),

clean up filter (Semrock Inc, New York, FF01-520/35-25) to remove unwanted laser wavelengths, dichroic mirror (Semrock Inc, LPD01-532RS) and emission filter (BLP01-532R, Semrock Inc.). An expanded schematic of the light path and optical components inside the confocal microscope is depicted in Figure 8. Continuous laser light travels through a liquid light guide (3 mm diameter, 1 m length, Newport, Irvine, CA, USA) into the spinning disk confocal system (CARV II, BD Biosciences, San Jose, CA, USA) which optically sections the flow. The excitation light diverges from the liquid light guide and is collimated by the collimating adapter. The collimated light travels through a bandpass clean-up filter that passes light in the wavelength range between 515 and 560 nm. Using a spectrometer (USB4000, Ocean Optics, Florida), I found that the laser has some energy in the red/infrared (~800 nm) portion of the spectrum. The output from spectrometer is shown in Figure 16 of section 3.2. The cleanup filter prevents unwanted noise that results from this extra energy peak. After the excitation light is reflected by the dichroic mirror, it passes through the confocal disk, a tube lens, and into the back focal plane of the microscope objective. The excitation light is focused onto the sample (in this case fluorescent microspheres), exciting it. The spheres emit fluorescence with a wavelength of around 620 nm. This emission light passes back through the tube lens, is spatially filtered by the confocal disk, and passes through the dichroic filter, which blocks wavelengths between 528 and 541 nm. Finally, the light passes through an emission filter which only allows light in the wavelength range of the emitted fluorescence pass. A second tube lens focuses the light onto the CMOS camera sensor.

A 12 bit, high speed CMOS camera (Phantom v12.1, Vision Research, NJ 07470, USA) capable of 6242 frames per second at 1280 x 800 resolution (over a million frames per second at reduced resolution) records images of the tracer particles. Standard Nipkow disks in the CARV II system can operate up to 5000 rpm, which corresponds to a maximum frame rate of 1000 Hz. Our spinning disk has 70 μm diameter pinholes and is custom balanced to allow for speeds of 15000 rpm, which allows us to capture images at 3000 Hz. A syringe pump (PHD2000, Harvard Apparatus, Holliston, Massachusetts, USA) delivers fluid to the microchannels. The focal plane depth and the depth scanning of the imaging system is controlled using a calibrated piezo-electric objective positioning system (PI-725, Physik Instrumente, Auburn, MA) and amplifier/controller (LVPZT).

Synchronization of the objective positioner and the camera is integral to the method. An arbitrary waveform generator (Agilent 33220A, CA, USA) and a pulse delay generator (PDG) (Berkeley Nucleonics Corporation, Model 575, CA, USA) are used for controlling and synchronizing the piezo and camera. The PDG is the master in the synchronization process and controls both the function generator and the camera directly. A TTL pulse from the PDG signals the function generator to deliver a sine wave to the piezo amplifier. The amplifier drives the objective positioner, which reports its actual position to the oscilloscope. A delayed and synchronized TTL pulse commands the camera to acquire images. An oscilloscope (Agilent DSO6104A, CA, USA) displays the waveforms and assists in the synchronization of the two TTL pulses.

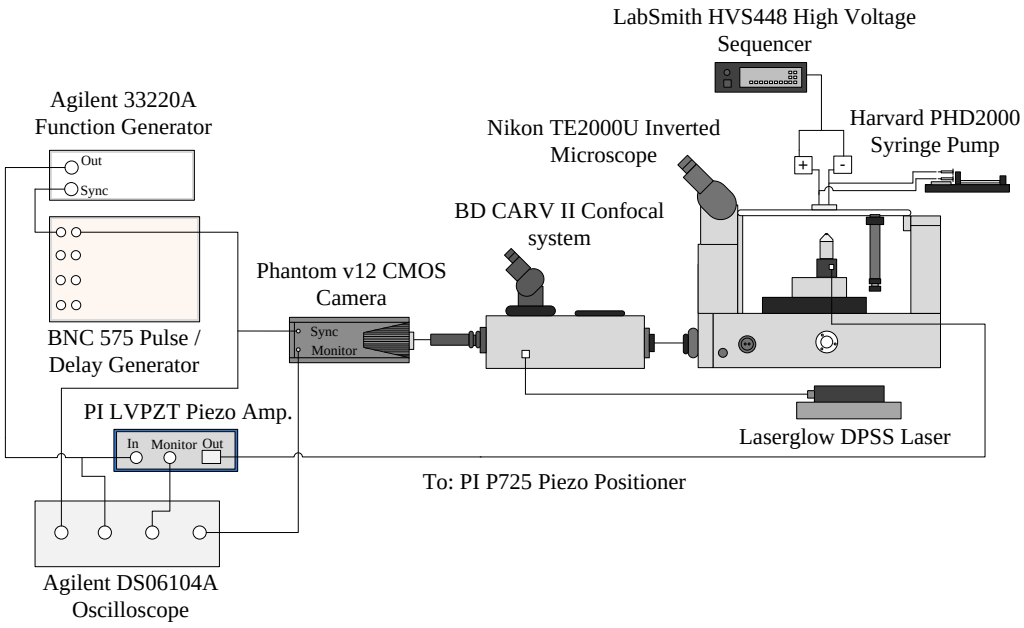

Figure 7. Schematic of the spinning disk confocal microscope.

Timing equipment synchronizes the objective positioner with the camera to ensure that slices occur at the same respective depth in each stack. A sine wave drives the positioner to avoid damped oscillations that can occur when driving the objective positioner quickly using a discontinuous driving signal (such as a triangle wave). Additionally, at high frequencies, the actual piezo displacement resembles a sine wave even for a triangle wave input waveform. This is because the damped system acts as a low pass filter (integrator) at high frequencies. This means that the actual position of the piezo at high speeds will be lagged in time behind the input waveform and will also have a gain that is less than 1 (actual displacement reduced compared to input waveform). Data is acquired using the nearly linear portion of the sine wave so that each slice is approximately the same distance apart in depth. However, because the depth positions of each slice are known from the piezo amplifier output, the slight non-linearity that occurs is

adjusted for. Additional details depicting the image capture method are included later in this chapter.

A piezo-electric objective positioning system (PI-725, Physik Instrumente, Auburn, MA, USA) and amplifier/controller (LVPZT, Physik Instrumente, Auburn, MA, USA) controls the focal plane depth and thereby the depth direction scanning of the imaging system. A syringe pump (PHD2000, Harvard Apparatus, Holliston, Massachusetts, USA) delivers fluid to the microchannels and two different electrical amplifiers are used. A high voltage sequencer (HVS448 6000D, LabSmith, Livermore, CA, USA) is used for the electrokinetic instability experiments presented in section 4.3.2. In the isotachophoresis experiments presented in Chapter 6, a sourcemeter is used in constant current mode (2410, Keithley Instruments, Cleveland, Ohio, USA) to apply the electrical field to the microchannel.

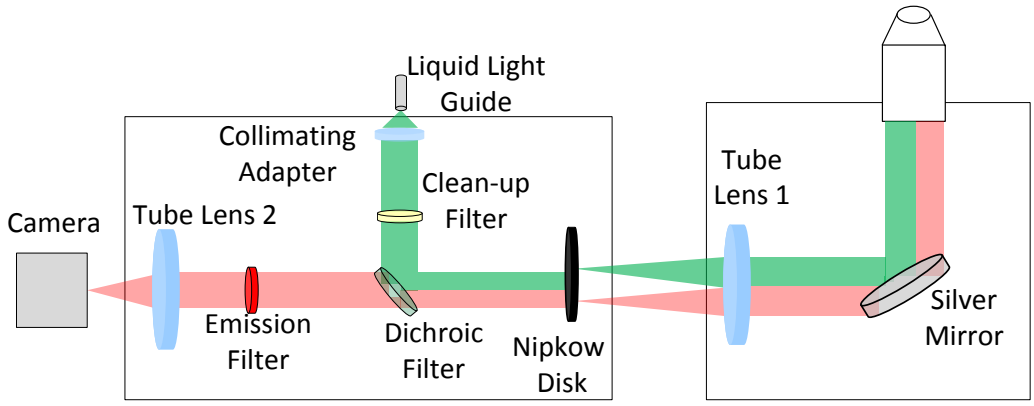

Figure 8. Optical components and path of excitation (green) and emission (red) light path in the confocal system.

3.2. Characterization of Laser System

The solid state laser used in this work can be used in time modulated or continuous mode. Its intensity can be adjusted by adjusting the voltage amplitude of a TTL input signal. Time modulated mode can be used to set the length of time that the particles are exposed to light, instead of using the camera's exposure time. This has the benefit of preventing smearing of the images for long exposure times. The power output of the laser was investigated as the frequency, voltage, and duty cycle of the TTL input signal was varied. Additionally, the confocal system was not designed to accept laser light but rather a white light source from a metal halide lamp, so the optimal coupling method was not apparent. Different methods of coupling the laser to the confocal system were investigated.

Figure 9 shows the output power of the laser with varying input voltage (duty cycle = 1) for various coupling methods. The black diamonds show the output power of the laser with a free beam before it passes through any optics. The red triangles line shows the power output of the laser after it exits the liquid light guide. The green circles depict the power output after the light passes through the liquid light guide, cleanup filter, dichroic filter, tube lens, and 40x microscope objective. The blue squares show the power output of the laser after the light passes through the liquid light guide, cleanup filter, dichroic filter, confocal disk, tube lens, and 40x microscope objective. This data was acquired using a Gentec laser power meter (Gentec Solo 2, USA). Although about 15% power is lost by coupling through the LLG, pictures of a uniformly filled capillary of fluorescent

dye shows that the beam quality and uniformity over the field of view is improved compared to the free beam coupling.

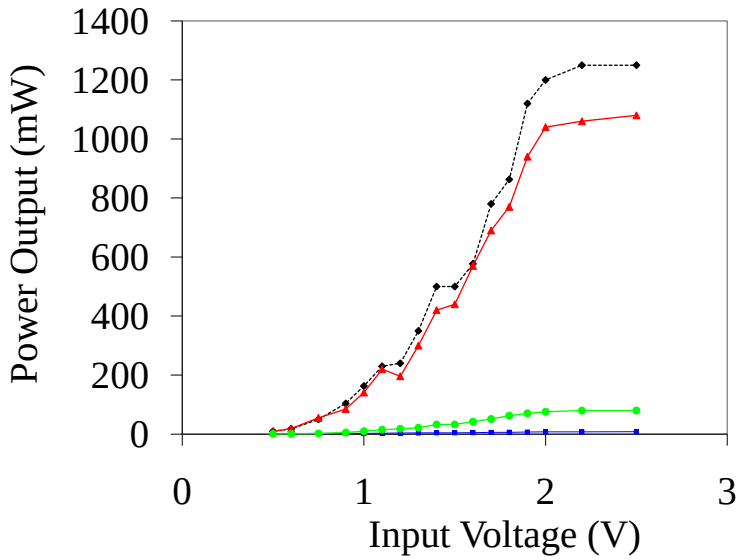

Figure 9. Power output of the laser with varying input voltage for liquid light guide coupling (red triangles), free beam (black diamonds), and through the confocal microscope using the 40x objective and LLG coupling with the disk in (blue squares) and disk out (green circles).

Next, the effect of varying the duty cycle and frequency of the TTL signal on the output power of the laser was investigated. Figure 10 shows the output power of the laser, measured using a diode photodetector because the laser power meter is too slow to resolve the quickly modulating laser signal (Thorlabs, DET 110, NJ, USA). The output of the photodetector is in volts and is converted to milliwatts by scaling with a power measurement from the Gentec Laser Power Meter. The blue line shows the baseline power output using a 99% duty cycle. As the frequency of the input signal increases the duty cycle is increasingly important in its effect on the output power.

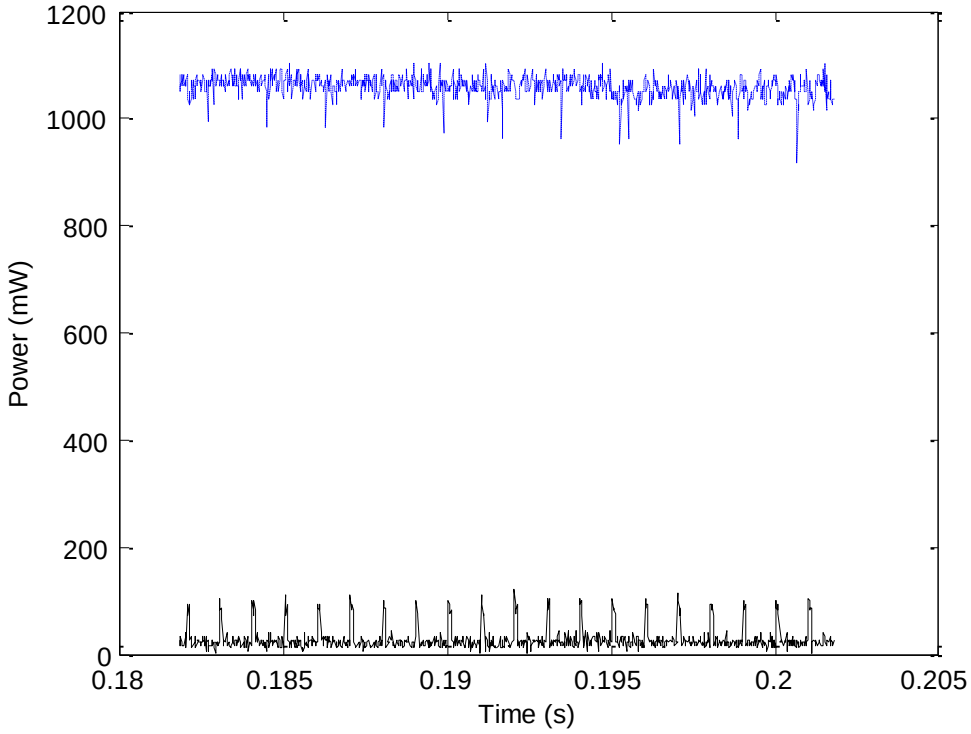

Figure 10. Laser output power in milliwatts at a 10% duty cycle and a frequency of 1000 Hz (black line). The blue line depicts the laser power at duty cycle of 99%.

Duty cycles of 10%, 50%, 70%, and 90%, at frequencies of 0.1, 1, 10, 100 and 1000 Hz are investigated. The results of this investigation are presented in Table 1. Each entry in the table shows the maximum of the laser output power for that experiment in milliwatts. At 10% duty cycle the laser power is at about 100 mW, except at the 0.1 Hz frequency, and as the duty cycles increases the laser power increases to 1000 mW. Similarly, at 1000 Hz the laser power is about 100 mW except at 90% duty cycle, and as the frequency decreases the laser power increases to 1000 mW. It is clear that the laser only has near optimal output power when it has either low frequency or high duty cycle. This means that the

laser is not very useful in time modulated mode. Therefore, in this work the laser is only used in continuous mode.

Table 1. Laser output power (instantaneous) vs. duty cycle and frequency

		Duty Cycle			
		10%	50%	70%	90%
Frequency	0.1 Hz	908	967	1062	1069
	1 Hz	314	836	879	986
	10 Hz	108	452	638	876
	100 Hz	101	183	507	912
	1000 Hz	105	108	850	1104

Additionally, the structure of the beam was characterized with the assistance of Dr. Michael Murphy and Professor Ronald Adrian at Arizona State University. Figure 11 through Figure 15 show an image of the beam projected onto a white target on the left and a line plot of the intensity of the beam on the right, at various output powers. At 100 and 300 mW, the beam shape is distinctly non-Gaussian and power is low. The shape of the beam changes with output power such that it is most Gaussian (single mode) between 600 and 850 mW. The beam quality is acceptable enough at 1200 mW that it is beneficial to run the experiments at this setting to take advantage of the extra light output.

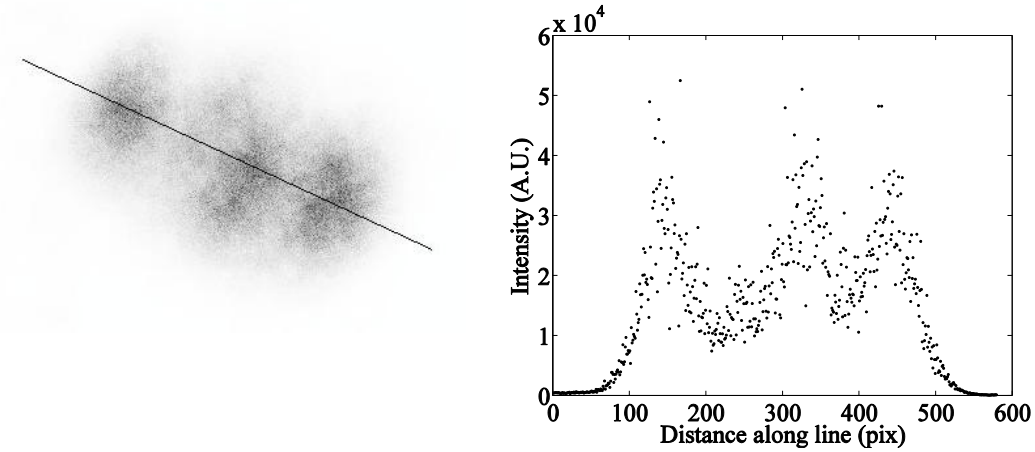

Figure 11. Image (left) and line plot (right) of laser intensity at 100 mW

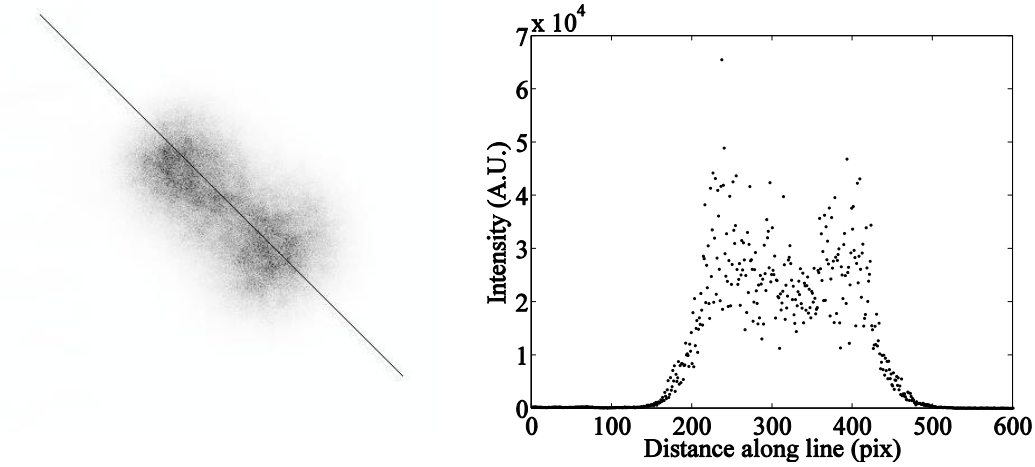

Figure 12. Image (left) and line plot (right) of laser intensity at 300 mW

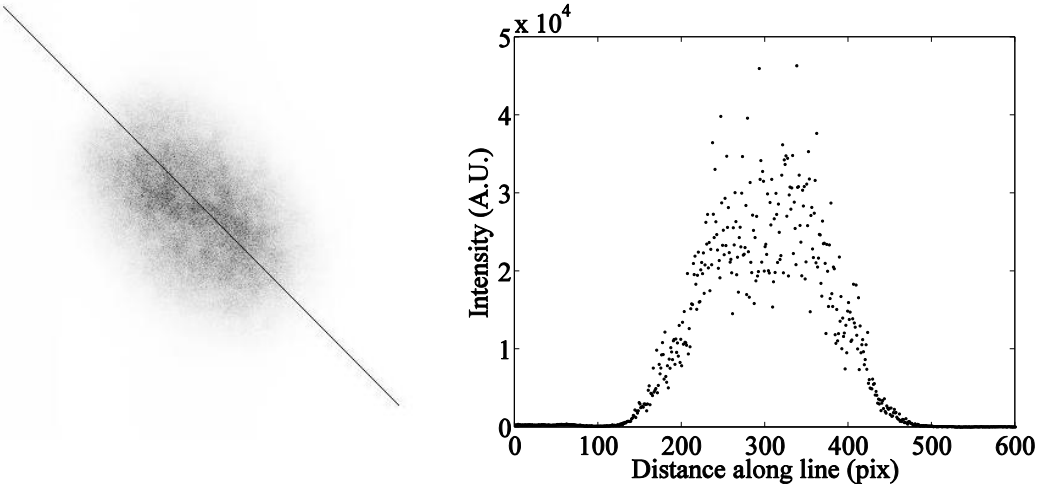

Figure 13. Image (left) and line plot (right) of laser intensity at 650 mW

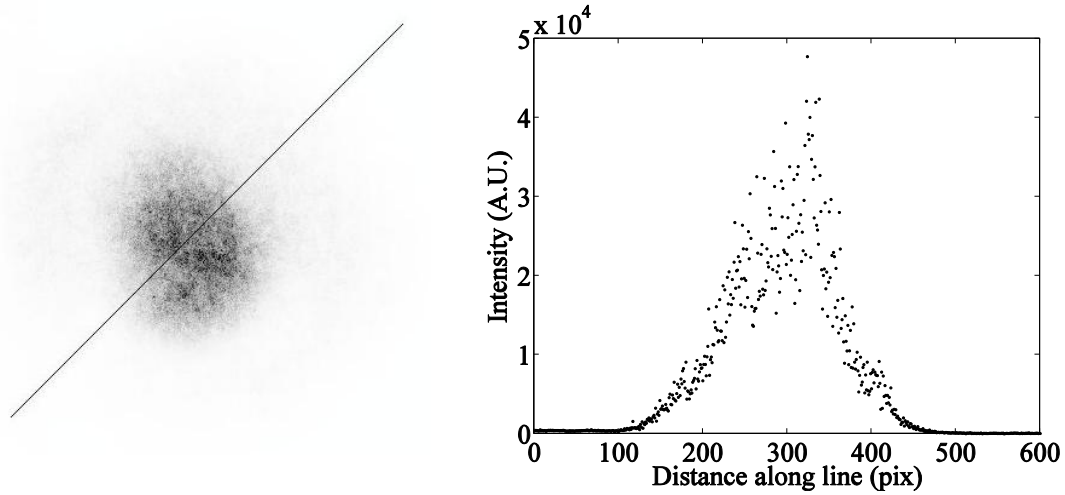

Figure 14. Image (left) and line plot (right) of laser intensity at 800 mW

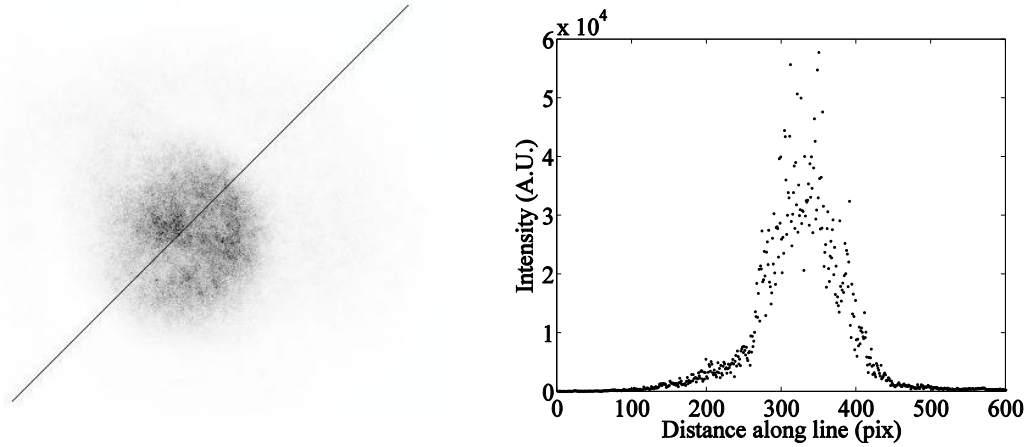

Figure 15. Image (left) and line plot (right) of laser intensity 1200 mW

When choosing the dichroic (Semrock Inc, New York, LPD01-532RS) and emission (BLP01-532R, Semrock Inc., New York) filters for the laser based epiflourescence experiments in this work, I first conducted a spectral analysis of the solid state laser. Figure 16 shows the results of this spectral analysis using a spectrometer (USB4000, Ocean Optics, Dunedin, Florida) on loan from Dr. Mark Hayes at Arizona State University. A large peak in intensity was observed at approximately 532 nm as expected. However, another peak in intensity was

present at 806 nm. Although this second peak accounts for only 5% of the maximum excitation light, it caused noise in the images because its energy was not completely removed by the dichroic and emission filters. Therefore, a cleanup filter (Semrock Inc, New York, FF01-520/35-25) was added in the image path to remove this unwanted noise.

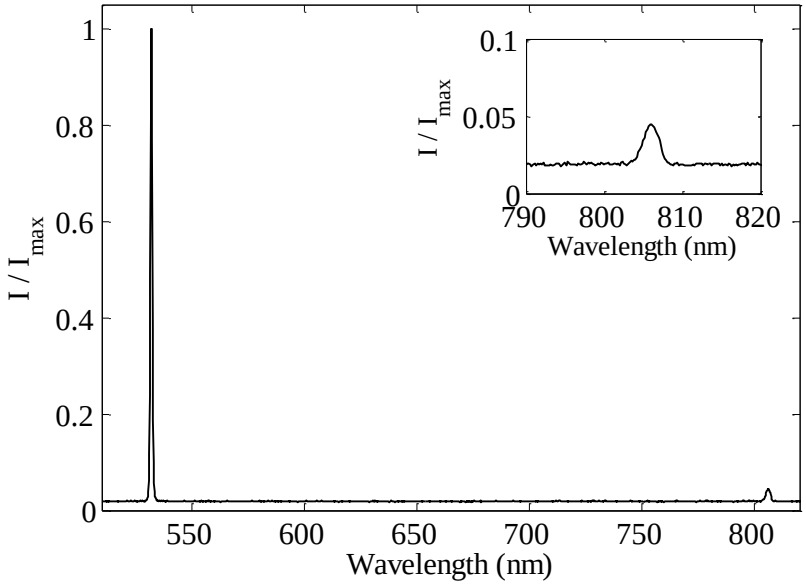

Figure 16. Spectral analysis of the solid state laser. The second peak at ~800 nm caused noise in the images. This was resolved by adding a cleanup filter into the light path.

3.3. Comparison of CMOS Cameras

During the design of the system various high speed CMOS camera models were investigated to determine which camera was the best fit for this system. The table below details the collected data on the various cameras that were investigated.

Table 2. Table depicting high speed camera characteristics

	Max Full Frame Rate (Hz)	Pixel Length (um)	Sensor size (pix)	Max memory (GB)	Bit depth	QE (%)	Min. exp. time (µs)	Inter-frame time (µs)	Price per GB ($1000 / GB)	Min. price ($1000)
Photron APX	2000	N/A	1024 x 1024	8	10	N/A	4	N/A	N/A	N/A
Photron 1024 pci	1000	17	1024 x 1024	12	10	N/A	1.5	N/A	N/A	N/A
Photron SV200i	2000	16	512 x 512	N/A	10	25-35	5	N/A	N/A	N/A
Photron APX RS	3000	17	1024 x 1024	16	10	N/A	2	N/A	N/A	55
Photron SA1.1	5400	20	1024 x 1024	32	12	N/A	0.38	0.675	3.13	80
Phantom Miro 3	1265	22	800 x 600	2	12	30-40	2	2.5	14.0	28
Phantom 7.3	6688	22	800 x 600	32	14	30-40	1	< 2	2.92	61
Phantom v5.2	1000	11.5	1152 x 896	12	8, 10,or 12	20-25	2	2.75	3.50	29
Phantom v9.1	1000	11.5	1632 x 1200	24	14	20-30	2	N/A	3.00	45
Phantom v12	6200	20	1280 x 800	32	12	30-40	0.3	0.5	3.66	87
IDT X3	1000	12	1280 x 1024	4	10	N/A	N/A	N/A	N/A	N/A
IDT X3+	2000	12	1280 x 1024	4	10	N/A	N/A	N/A	9.25	37
IDT X3I	2000	12	1280 x 1024	4	10	35-40	N/A	0.1	22.5	90

The first column shows the maximum frame rate for each camera at full resolution. As the region of interest is decreased, faster frame rates are possible. The next column is the size of one pixel in microns, an important parameter for spatial resolution. The sensor size in pixels, sometimes called the resolution, can be multiplied by the pixel length to get the area of the detector. The max memory column lists the largest available on board memory, however additional memory

is available externally in some cases. The bit depth column indicates the level of detail with which the intensity of an image can be recorded (for example: an 8-bit camera has a maximum intensity of 2^8 or 256 bits). QE is the quantum efficiency of the camera, which is the ratio of absorbed photons to electrons produced, a parameter related to sensitivity. The min. exp. time is the minimum exposure time, and the interframe time is the minimum time between frames. Both of these are important when recording very fast phenomena. The final two columns relate to the price of the cameras, the price per GB is calculated using the maximum available on-board memory price, whereas the minimum price is the price of the camera with no addons and the minimum amount of memory available.

For this diagnostic system, the highest speed camera available was desired so that the camera would not be the limiting factor for the total system speed. Additionally, high sensitivity was important, because the fluorescent tracer particles used in the experiments are not very bright. Smaller pixel size improves the ability of the system to resolve particle centroids, so this parameter is also important. Based on speed, the optimal choices were the SA1.1, the v7.3, and the v12. The v12 and SA1.1 have a smaller pixel size, so these two models were investigated further. After conducting in-house tests using demos of both cameras, the v12 was chosen. It is slightly faster, and performed better when imaging flow in microfluidic channels due to the rectangular sensor and slightly increased sensistivity.

3.4. Confocal Depth of Correlation and Measurement Depth

The confocal system allows for a better image of the tracer particles in PTV and PIV as shown in section 2.2. Figure 5 in Chapter 2 shows the *X*-*Z* cross section of a 3 μm fluorescent polystyrene sphere acquired using both the confocal and widefield systems. The removal of the 'wings' in the image of the sphere is apparent. This ability of the confocal to remove out of focus light and reduce the effect of the wings of the PSF also affects PIV measurements by affecting the PIV depth of correlation and measurement depth. Both the depth of correlation and measurement depth of the system (see Chapter 2) are important parameters for μPIV. The measurement depth is simpler to measure because it is based on the intensity of the particle itself, rather than the slope of the correlation peak (Bourdon, Olsen, and Gorby 2004). Figure 17 shows the axial intensity profile for a 500 nm polystyrene bead affixed to a coverslip and immersed in DI water. The traces consist of 200 frames with an axial shift of 0.1 μm per frame. Particle intensity and background noise levels are matched between the confocal and widefield modes. Traces are normalized by the maximum intensity and background noise level, and positive values indicate increasing distance into the sample. The full width of each axial intensity profile at 10% intensity is the experimental measurement depth. Figure 17 shows that the confocal system reduces the measurement depth of a 500 nm bead from 5.7 to about 4 μm, or by about 30% compared to the widefield system. Next, experimental measurements are compared to theoretical predictions of measurement depth for both systems.

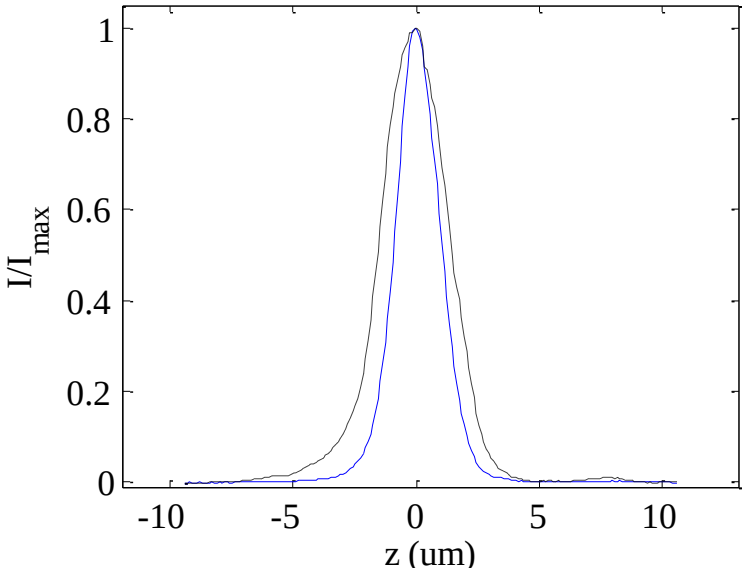

Figure 17. Intensity profile for 500 nm polystyrene bead affixed to cover slip immersed in water. Solid line is the confocal intensity trace and the dashed line is the widefield intensity trace. Traces consist of 200 frames with an axial shift of 0.1 μm per frame. Particle intensity and background noise level are matched between the confocal and widefield modes. Traces are normalized by their respective maximum intensity and background noise levels. Positive values indicate increasing distance into the sample.

Figure 18 shows the experimental and theoretical μPIV measurement depth for 0.2, 0.5, 3, and 7 μm diameter particles. The experimental and theoretical measurement depth is calculated as the sum of the distance above and below the focal plane at which the particles reach 10% of their in focus intensity. The theoretical data is computed for the WF case from discretized versions of (5) - (7) convolved with the spherical particle of appropriate diameter, whereas the confocal case is acquired from the square of (5) - (7) convolved with the

spherical particle of appropriate diameter. The experimental and theoretical measurements do not match quantitatively but appear to have the same trend.

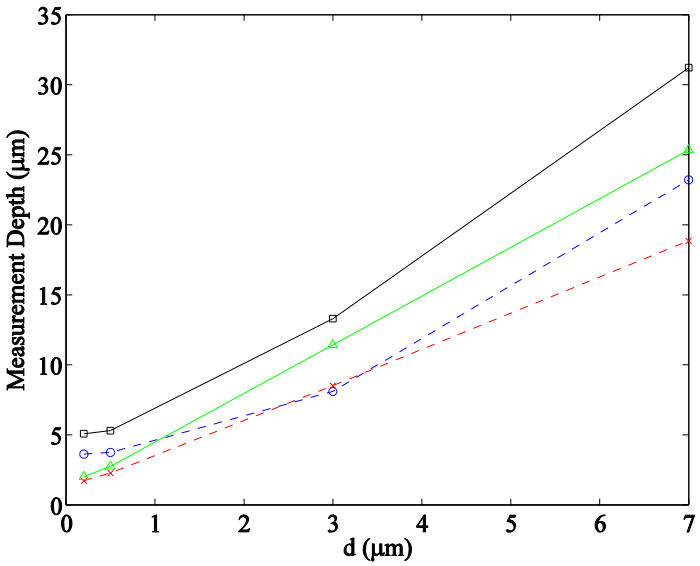

Figure 18. Depth of correlation for particle diameters ranging from 0.2 to 7 µm. Confocal experiment (o) and simulation (x) along with widefield experiment (square) and simulation (triangle). The experimental data matches the trends predicted by theory, and the confocal system is seen to decrease the measurement depth in every tested case.

It would appear from Figure 18 that at small particle sizes diffraction dominates the measurement depth in the system as expected, with optical system aberrations likely accounting for the remaining discrepancy. Although spherically corrected high *NA* objectives are used with matched immersion media and coverslip correction, inevitably some spherical aberration will be present in the system. The shift from predicted measurement depth values may be due to remaining system wide aberrations such as spherical aberration. Both experimental measurements and theoretical predictions show that the µPIV

measurement depth is reduced for a confocal system as compared with a widefield system. This is true even for systems with finite sized pinholes in which the *z* resolution is not actually improved but the confocal pinholes still remove out of focus light and flare from the particle images. Confocal systems can therefore be used in μPIV measurements to remove out of focus particle noise and improve the accuracy of the velocity measurements in the *z* direction (Park and Kihm 2006), and to improve two frame cross correlation signal to noise ratio allowing high speed μPIV measurements of unsteady flows (Klein and Posner 2010).

3.5. Confocal Disk Timing

A Nipkow spinning confocal disk contains an array of micron scale pinholes that are used to optically section the image of a flow. This allows much faster acquisition times than traditional confocal microscopy (Webb 1996). The disk used in this work contains pinholes in an Archimedean spiral (concentric lines of pinholes that spiral slightly inward toward the center of the disk). An image of the pinholes in our confocal disk is depicted in Figure 19. A sector is defined as 1/12th of the disk, or $\pi/6$ radians. This is the portion of the disk that must pass the camera sensor during one exposure time to avoid image artifacts (Chong et al. 2004). This requirement of one sector per exposure constrains the minimum exposure time of the system and frame rate and depends on the angular velocity of the disk. The maximum camera frame rate (inverse of minimum exposure time) depends on the confocal disk speed (assuming adequate fluorescence intensity) as shown in (13) below,

$$\Delta t_{slice,\min} \geq \frac{n\pi}{6\omega} \qquad (13)$$

where ω is the disk speed in rad/s, n is a positive integer, and $\Delta t_{slice,min}$ is the minimum exposure time of the camera. This equation states that the confocal disk must rotate an integer multiple of $\pi/6$ radians (one sector of the disk) during an exposure to avoid image artifacts (Klein and Posner 2010; Chong et al. 2004). For short exposure times ($\Delta t < 5\ \Delta t_{slice,min}$) this equation should be satisfied to avoid artifacts, but for long exposure times the artifacts are averaged out. Our disk spins up to 15000 RPM, allowing a maximum camera frame rate with the confocal disk of 3000 fps. The maximum camera frame rate without the confocal disk in the light path depends on the illumination, magnification and *NA* of the objective, and size of the particles used (Inoue and Oldenbourg 1994). For a 60x objective with an *NA* of 1.2, and the laser power reduced to 120 mW to protect the microscope objective, the max frame rate without the confocal disk is about 10000 Hz for 1 μm diameter particles and 5000 Hz for 500 nm particles. The maximum frame rate is simply $f = 1/\Delta t_{slice,min}$ assuming no interframe delays.

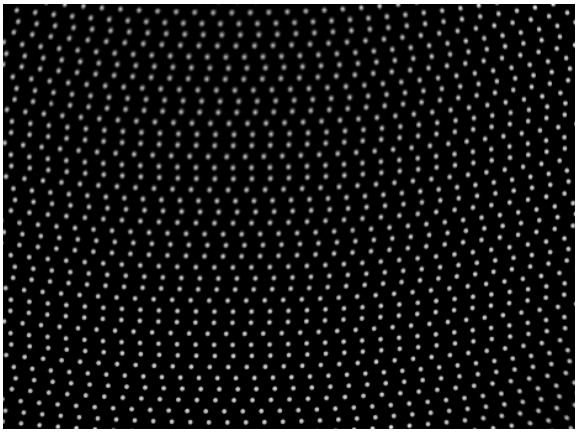

Figure 19. Image of pinhole pattern for spinning disk confocal system.

Note that the disk pattern is continuous such that no synchronization is required between the rotation of the disk and the start of each exposure. In this work, I use short exposures equal to a single $\Delta t_{slice,min}$ for the EKI experiments and 3D3C volumetric particle velocimetry experiments. I use exactly $3\Delta t_{slice,min}$ in the experiments to quantify the improvements in correlation S/N granted by the confocal system. Figure 20 shows images of a uniform concentration of rhodamine dye taken (a) with and (b) without satisfying (13). The concentric lines that are seen in Figure 20b are the result of partially scanned sectors.

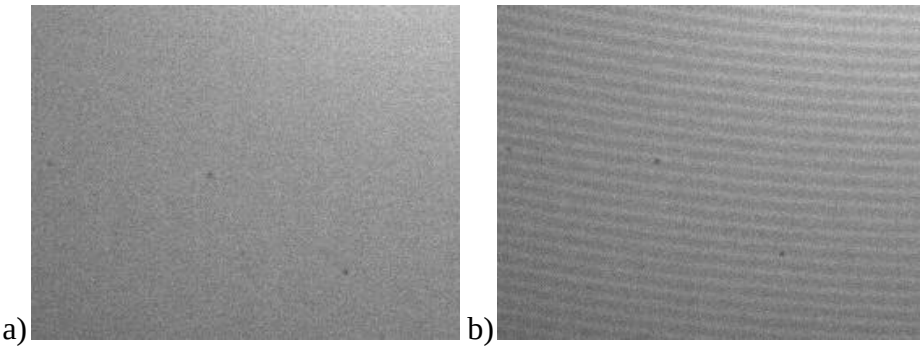

Figure 20. Images of Rhodamine B dye imaged with the confocal system for a) integer Δt_{min} or long exposure times, and b) short, non-integer Δt_{min} exposure times.

3.6. Piezo and Camera Timing

Synchronization of the piezo actuated objective positioner and the CMOS camera is integral to the 3D3C volumetric velocimetry method described in section 3.1. When the equipment is synchronized, respective slices in each stack correspond to the same depthwise position. A description of the equipment used in Figure 21 is given in section 3.1.

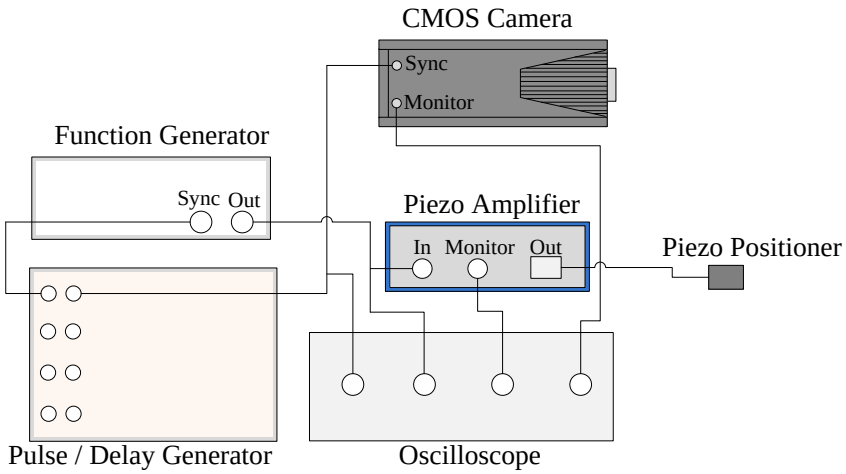

Figure 21. Timing equipment setup for synchronization of piezo and camera.

The 3D scanning method uses a piezo positioner to displace the objective, translating the focal plane of the microscope through the depth of the structure under examination. The high speed camera is synchronized using the equipment in Figure 21 to capture individual 2D images as the microscope objective scans the depth of the microchannel. Each 2D frame captured by the camera is referred to as one slice and the set of slices for each scan is referred to as a stack.

A sine wave is used to drive the piezo to reduce oscillations observed when the system is driven at high speed by a discontinuous driving signal. The approximately linear portion of the sine wave is used for measurements. The portion of the sine wave that is assumed to be linear fits a linear function with a correlation coefficient of $R^2 = 0.9969$ as shown in Figure 22.

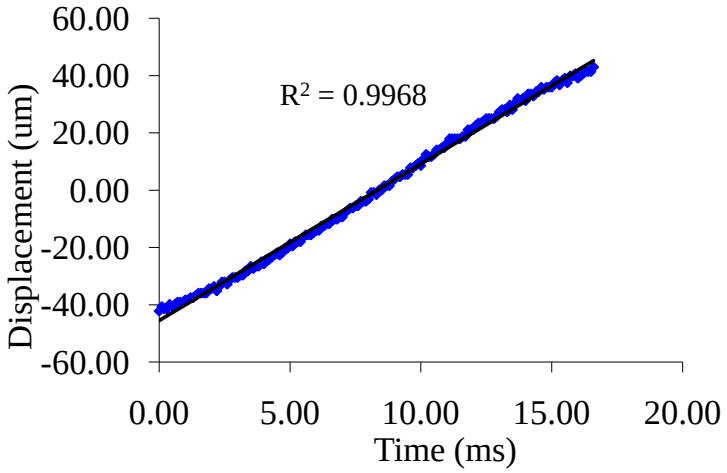

Figure 22. Linear fit to portion of sine wave used for experiments. Position of piezo at every slice is recorded and used to correct for non-linearity.

Figure 23 shows the waveforms as they would appear on the oscilloscope during the timing synchronization process for capturing stacks on only the upward scan. The red curve has a high value when the camera is exposing. The blue curve depicts the input to the piezo amplifier and the black curve represents the actual position of the piezo from the output of the piezo amplifier. The actual position of the piezo is lagged from the input waveform and the distance traveled attenuated compared to the input signal as the piezo approaches its maximum translation velocity. The oscilloscope is used to measure the level of attentuation and lag, and adjust accordingly. Further details about the piezo and camera timing are given in section 3.9.

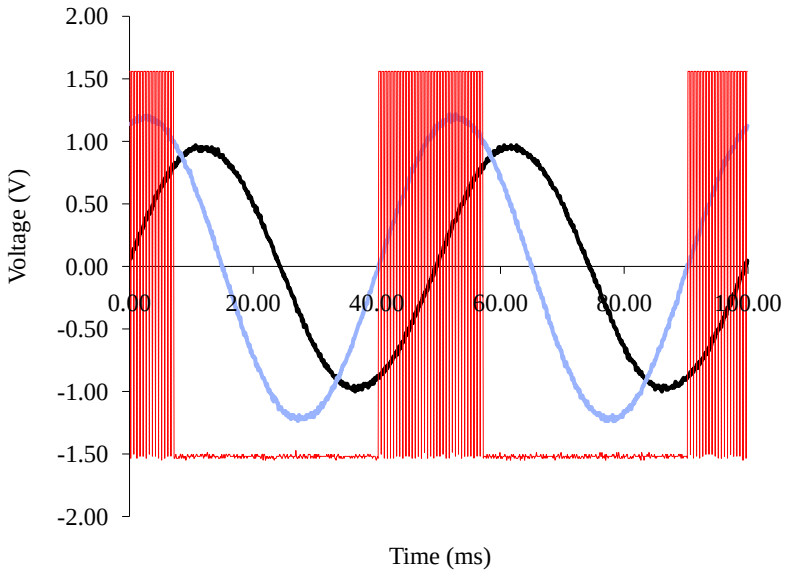

Figure 23. Timing waveforms for synchronization of the piezo and camera. The red curve has a high value when the camera is exposing. The blue curve depicts the input to the piezo amplifier and the black curve represents the actual position of the piezo from the output of the piezo amplifier.

3.7. Super Resolution PIV Algorithm

A super resolution algorithm determines the 3D3C velocity fields for the experimental data shown in Chapter 5. Super resolution PIV increases spatial resolution in particle velocimetry by combining PIV and PTV (Keane, Adrian, and Zhang 1995). The technique uses a PIV vector field as an initial predictor for PTV measurements (Keane, Adrian, and Zhang 1995; Devasenathipathy et al. 2003; Stitou and Riethmuller 2001; Kim and Lee 2002; Bastiaans, van der Plas, and Kieft 2002; Takehara et al. 2000; Vedula and Adrian 2005; Adrian 1997; Yamamoto and Uemura 2003). In PTV, the distance that particles travel between frames should be less than the distance between adjacent particle images in the same frame. In general, using a PIV predictor field for PTV shrinks the required search radius, thus increasing the possible particle image density for the same

particle displacements compared to PTV (Adrian 1997). Super resolution techniques increase the spatial resolution of the velocity data compared to PIV because the particle image density rather than the interrogation window size defines the resolution (assuming that the particle displacement is of the same order as the inter-particle spacing) (Keane, Adrian, and Zhang 1995).

The PIV predictor vector field is acquired using an in-house 3D3C PIV code adapted from a 2D algorithm (Mori and Chang 2003). The algorithm can currently process 3D3C PIV images, but is quite basic. Window shifting and other advanced PIV techniques are not yet implemented. Improvement of the 3D3C PIV code should improve the results beyond what is presented in this work. For the experiments shown in Chapter 5, an interrogation window size of 64 by 64 by 8 pixels is used, in the *x*,*y*, and *z* directions respectively.

The super resolution PIV code uses the 3D3C PIV results to predict the displacement of individually tracked particles. The 3D particle tracking algorithm used here was developed by Crocker, Grier, and Weeks (Crocker and Grier 1996; Weeks et al. 2000). Some modification to the algorithm was required to allow batch processing of multiple volumes, and to include the displacement estimates from the PIV code. The algorithm is able to locate particle centers with a theoretical accuracy of 0.1 pixels and track them in three dimensions, and has optional bandpass filtering and background subtraction options to preprocess the images before calculating particle centers. The main inputs to the algorithm are: tracking radius, minimum trajectory length, and centroid search radius. The tracking radius is the radius in 3D around which the algorithm searches the next

frame for the matching particle. The minimum trajectory length is the minimum number of frames that a trajectory must be in order to be considered, and the centroid search radius is the 3D radius that determines which pixels near each local maximum are used to determine the subpixel centroid of the particle. For the experiments in Chapter 5, at volume fractions of φ = 0.004 and φ = 0.001, tracking search radii of 1.75 μm and 3.5 μm are used, respectively.

3.8. Synthetic Image Generator to Validate Algorithms

This section details a volumetric synthetic particle image generation (SIG) code created in collaboration with Joshua James, an undergraduate researcher who I mentored in the Fulton Undergraduate Research Initiative (FURI) program. There are a variety of SIG codes that have been created for the testing of PIV and PTV algorithms (Westerweel and Lecordier 2003; Okamoto et al. 2000), however available codes are not capable of volumetric image creation, instead creating projected 2D images. The SIG code is used to validate the PTV and PIV algorithms as a first step to ensure that they work as expected in 3D and with sufficient accuracy to measure particle motion. The analysis performed here is preliminary and gives a simple estimate of the accuracy of the 3D3C PIV and PTV algorithms in use in this work.

The intensity distribution of the synthetic particles is produced using equations from Olsen and Adrian's paper on depth of correlation in micro PIV (Olsen and Adrian 2000). Equations (14) and (15) below describe the particle intensity distribution (Bourdon, Olsen, and Gorby 2004).

$$I(x,y,z) = \frac{\left(J_p / I_o\right) D_a{}^2 \beta^2}{4\pi d_e{}^2 (s_o + z)^2} \exp\left(\frac{-4\beta^2 \left(\sqrt{x^2 + y^2}\right)^2}{d_e{}^2} \right) \qquad (14)$$

$$de^2 = M^2 dp^2 + 5.95(M+1)^2 \lambda^2 \left(\frac{n}{2NA}\right)^2 + \frac{M^2 dz^2}{\left(n/(2NA)\right)^2} \qquad (15)$$

Here, x and y are the positions of the particle in the image plane, z is the distance from the object plane, d_e is the particle image diameter, M is the magnification, s_0 is the object distance of the objective, D_a is the aperture diameter of the microscope objective, λ is the wavelength of emitted light, and (J_p/I_0) is the total flux of light emitted from the particle surface per unit of illumination intensity. β is a fitting parameter which best approximates the Airy function with a Gaussian distribution. Adrian and Yao (Adrian and Yao 1985) determined that a value of $\beta^2 = 3.67$ provided the best fit. These synthetic image equations do not include any effects of the confocal system.

The SIG code has the following adjustable parameters to allow it to conform to typical experimental conditions. These include: pixel length, detector size (in plane), number of slices (out of plane resolution), physical channel depth, particle diameter, number of particles per volume, objective magnification, objective numerical aperture, immersion medium index of refraction, number of volumes, and intervolume displacement in the x,y, and z directions.

The synthetic images parameters are set to approximate typical values in a µPTV or µPIV experiment. The detector size is set to 512 x 512 pixels, the

number of slices is 25, the pixel length = 20 μm, the particle diameter is 1 μm, the total measured magnification is 66, the number of particles is 50 for the PTV experiments and 1000 for the PIV experiments, the NA is set to 1.2 with index of refraction at 1.33 (for water), the number of volumes is set to 10 for PTV and 2 for PIV, and the physical channel depth is set to 50 μm.

To determine the accuracy of the PTV code in measuring particle centroids, 50 synthetic images are created at random locations in a 3D volumetric image. The PTV code detects the centroids of the particles and compares the detected centroids with the known particle positions. Table 3 shows the results. The mean error in determining the centroid location is on the order of 0.1 pixels, and the standard deviation of the error is about 0.06 pixels for each dimension. This indicates that the code is of acceptable accuracy for these measurements.

Table 3. Table Centroid calculation error for PTV algorithm

# Particles	*X* Mean Error (pix)	*Y* Mean Error (pix)	*Z* Mean Error (pix)	*X* Error STD (pix)	*Y* Error STD (pix)	*Z* Error STD (pix)
50	0.077	0.094	0.136	0.059	0.069	0.057

A uniform displacement of $dx = dy = dz = -2$ pixels is applied to synthetic images and measured using the 3D PIV algorithm. The difference between the true and calculated displacements is then investigated. The results are presented in 3D vector form in Figure 24. The images are processed at an interrogation window size of 128 by 128 by 8 pixels with no post processing nor outlier detection. Qualitatively, the vectors seem to agree with the true displacements, but there is some error in the quantitative results, as depicted in Table 4. The

error is on the same order as expected for standard cross correlation PIV with a Gaussian subpixel interpolator ($1/10^{th}$ of a pixel).

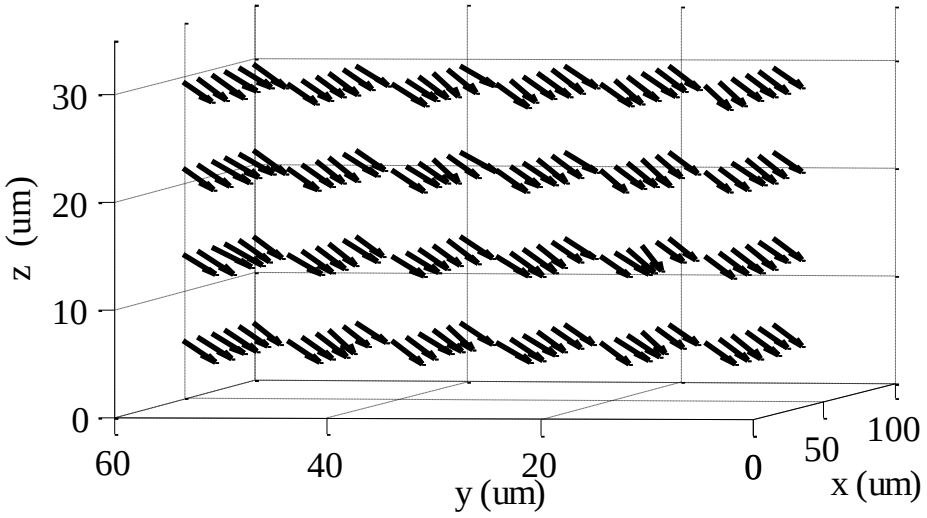

Figure 24. 3D PIV results for synthetic images with uniform displacement of $dx = dy = dz = -2$ pixels.

Table 4. Error in PIV algorithm using synthetic images

	x	y	z
True Value (pix)	-2	-2	-2
Mean displacement (pix)	-1.98	-1.96	-2.15
Standard deviation of displacement (pix)	0.20	0.17	0.34

3.9. Maximum Measurable Velocity for Volumetric 3D3C Super Resolution PIV

This section discusses the maximum measurable velocity of the system as a function of the experimental parameters, including the average piezo speed, camera frame rate, volume fraction, and the flow conditions. The maximum velocity is predicted based on three conditions: PIV and PTV constraints from

the literature ($\bar{U}_{max,PIV}$ and $\bar{U}_{max,PTV}$), and a constraint on the allowable particle deformation ($\bar{U}_{max,scan}$). An overbar indicates a vector quantity. The system acquires stacks with a period of Δt_{stack}, with N slices in each stack, and acquires slices with a period of Δt_{slice}. The distance that the objective travels between slices, P_z, becomes the pixel size in the z-direction. As mentioned earlier, P_z should be less than the FWHM of the point spread function (PSF) of the imaging system. The FWHM for this equipment is measured to be around 2 μm using the method of Meinhart et al. (Meinhart, Wereley, and Gray 2000). In brief, a diffraction-limit sized (500 nm) fluorescent particle was affixed to a glass slide and its intensity was measured as the focal plane of the objective was translated. The depth of the acquired 3D image, D, is given by $D = P_z N$. Figure 25 shows a detailed diagram of D, P_z, N, Δt_{stack}, and Δt_{slice}. Analysis in this section assumes that the: 1) data is only acquired on the upward scan of the piezo positioner; 2) data is only acquired in the portion of the sine wave between $-\pi/4$ and $\pi/4$ radians (¼ of the period of the sine); and 3) the scanned depth, D, takes up the entire region from $-\pi/4$ to $\pi/4$. Figure 22 shows a linear fit to the portion of the sine wave mentioned in assumption 2.

Other parameters of interest include: the average piezo speed (over one full period of the sine wave) $U_{piezo,avg}$; the interparticle spacing δs; the tracer particle diameter d; and the volume fraction of particle tracers φ. The volumetric object space interrogation window size $\bar{I}_w = (I_x, I_y, I_z)$ depends on the image space interrogation window $\bar{I}_p = (I_{xp}, I_{yp}, I_{zp})$, the 3D image space pixel size $\bar{P} = (P_x, P_y, P_z)$, and the magnification, M, as $\bar{I}_w = \bar{I}_p \bar{P}/M$. The maximum piezo

speed, $U_{piezo,max}$ is measured to be approximately 4.1 mm/s. Two of the system parameters, Δt_{slice} and $U_{piezo,avg}$, have additional constraints placed on them. For the current system, Δt_{slice}, and therefore the maximum camera frame rate (inverse of minimum exposure time) is limited by the angular velocity of the confocal disk. Assuming 100% duty cycle of the camera, the minimum exposure time of the camera is approximately equal to the interframe time as shown in (13), reprinted here for convenience,

$$\Delta t_{slice,min} \geq \frac{n\pi}{6\omega} \qquad (13)$$

where ω is the disk speed in rad/s, and n is a positive integer. This equation states that the confocal disk must rotate an integer multiple of $\pi/6$ radians (one sector of the disk) during an exposure to avoid image artifacts (Klein and Posner 2010; Chong et al. 2004). The disk in this work spins up to 15000 RPM, allowing a maximum camera frame rate of 3000 fps. The maximum camera frame rate without the confocal disk in the light path depends on the illumination, magnification and NA of the objective, and size of the particles used (Inoue and Oldenbourg 1994). For a 60x objective with an *NA* of 1.2, reduced laser power of 120 mW to protect the system optics, and 1 μm diameter particles, the max frame rate for this experiment is about 10000 Hz.

The other limitation on the system is based on assumptions 2 and 3. If the system is utilizing only the nearly linear region of the sine wave, then $N\Delta t_{slice} \leq F\Delta t_{stack}$, where F is the fraction of the sine wave that is deemed nearly linear. In this work, as stated in assumption 2, F = ¼. Substituting $\Delta t_{stack} = 2C_d D/U_{piezo,avg}$ and $N = D/P_z$,

$$U_{piezo,avg} \leq \frac{C_d P_z}{2\Delta t_{slice}} \quad (16)$$

where C_d is a coefficient representing the extra distance traveled by the piezo compared to the linear region (from assumption 2, $C_d = \sqrt{2}$ for our work).

Equation (16) indicates that the time between slices must be short enough relative to the average piezo speed that the stack is acquired in the linear portion of the sine wave. If Δt_{slice} is reduced, then $U_{piezo,avg}$ can be increased, which increases the maximum measurable velocity. The total distance traveled by the piezo is $C_d D$. The maximum travel distance of the objective positioner is 340 µm. This corresponds to the maximum scan depth for 3D measurements for very slow 3D acquisition rates (~ 1 Hz) where discontinuous waveforms can be used. The maximum average piezo speed, $U_{piezo,max}$ was measured to be about 4200 µm/s.

The maximum measurable velocity can be predicted by adapting equations from literature to this scanning technique. PTV directly tracks particles in a 3D volume, and PIV estimators predict the location of the particles. This technique is often called super resolution PIV in the literature, but PTV determines the final velocity. The maximum displacement of the particles should be less than ¼ of the size of the interrogation window in the PIV step (Adrian 1991). Substituting the maximum velocity, $\bar{U}_{max,PIV}$, multiplied by Δt_{stack} for the maximum displacement results in (17):

$$\bar{U}_{max,PIV} \leq \frac{\overline{IP}}{4M\Delta t_{stack}} \quad (17)$$

The time between stacks is $\Delta t_{stack} = 2C_d D / U_{piezo,avg}$ because the system only acquires data on the upward scan, therefore the distance traveled by the piezo is double the total travel distance. Substituting this relationship for Δt_{stack} results in:

$$\bar{U}_{max,PIV} \leq \frac{\overline{I_p}\overline{P}U_{piezo,avg}}{8C_d M D} \quad (18)$$

The maximum velocity from the PIV constraint is both a function of the average piezo speed and experimental parameters (i.e. window size, pixel size, and magnification) as well as the scanned depth of interest *D*.

Typical PTV algorithms require the displacement of the particles between images (volumetric in this case) to be less than the interparticle spacing in a single image. In super resolution PIV this requirement is relaxed, with the amount of relaxation depending on the accuracy of the PIV estimator used to predict the position of the particle. As a conservative estimate, the maximum velocity can be estimated based on the typical PTV criterion. Again, $\bar{U}_{max,PIV}\Delta t_{stack}$ is substituted for the displacement. The interparticle spacing is estimated as $\delta s \sim 0.3\pi^{1/3} d\varphi^{-1/3}$ (Chandrasekhar 1943). Substituting this relation for δs results in:

$$\bar{U}_{max,PTV} \leq \frac{0.3\pi^{1/3} d U_{piezo,avg}}{2C_d D \varphi^{1/3}} \quad (19)$$

The maximum velocity based on PTV constraints is directly proportional to $U_{piezo,avg}$ and d, and is affected inversely by φ and D.

The third constraint limits the amount of deformation of the particle images due to particle displacement during the upward scan of the objective positioner. For a particle image of diameter $P_z N_p$, where N_p is the number of slices the

particle image takes up in z, the maximum particle displacement is $U_{max}\Delta t_{slice}N_p$. The angle of the particle image deformation is $\tan^{-1}\left(\frac{P_z}{U_{max}\Delta t_{slice}}\right)$ as shown in Figure 25 (N_p drops out). If the angle of deformation is limited to ±5 degrees from the vertical, this results in:

$$\boldsymbol{U_{max,scan} \leq \frac{P_z}{C_\theta \Delta t_{slice}}} \qquad (20)$$

where C_θ is 11.45 (tangent of 85°) for $U_{max} > 0$. For the experimental parameters given in Table 1, θ = 88.2°. This indicates that system is not limited by $U_{max,scan}$ in this work.

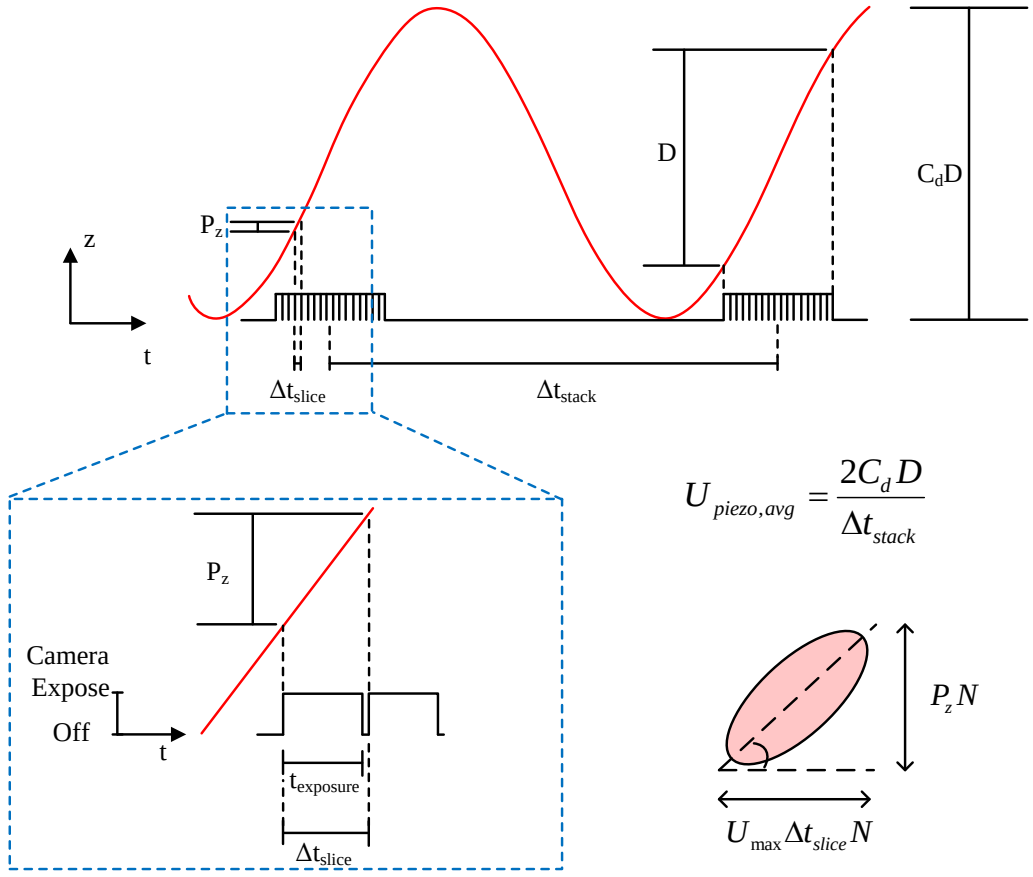

Figure 25. Schematic of parameters for 3D3C volumetric particle velocimetry. The camera exposes with exposure time $t_{exposure}$ and a time between images of Δt_{slice}. The distance over which the camera is taking images is D, and the total distance traveled by the piezo is C_dD. The piezo travels a distance P_z between images (slices). The lower right corner shows how a particle image could be deformed by displacing during the scan.

The values of the parameters for this work appear in Table 5. Using these parameters (at a volume fraction, $\varphi = 0.004$) results in a maximum PIV x and y velocity of $U_{max,PIV,xy}$ = 145 μm/s, a maximum PIV z velocity of $U_{max,PIV,z}$ = 62 μm/s, and a maximum $U_{max,PTV}$ of 84 μm/s. Allowing θ to be as large as 85°, the maximum measurable velocity based on the scan speed, $U_{max,scan}$, is 275 μm/s. The highest experimental velocity in the x and y directions at $\varphi = 0.004$ is about 95 μm/s. This equates to velocities of about 1 field of view per second or 95 particle diameters per second, and a Peclet number of 100. This work does not optimize the experiments for maximum velocity, so this measured velocity simply represents example data and higher values are possible. In this case the system is able to exceed the maximum velocity prescribed by the PTV limitations because it is using PIV as a predictor for the PTV particle matching which allows it to successfully pair particles outside the classical PTV search area. For a constant φ, the number of PTV outliers should increase as the predicted maximum velocities are approached, because as the displacements increase and more particles are incorrectly matched. In section 5.5 I provide some qualitative evidence of this, but do not perform an exhaustive study here.

Table 5. Values of parameters for 3D3C channel flow

I_x, I_y (pix)	I_z (pix)	P_x, P_y (μm)	P_z (μm)	$U_{piezo,avg}$ (μm/s)	$U_{piezo,max}$ (μm/s)	D (μm)	M	d (μm)	φ (%)
64	8	20	1.04	2120	4200	25	66	1	0.1, 0.4

Table 6. Maximum values of velocity for 3D3C channel flow

φ (%)	$U_{max,PIV,xy}$ (μm/s)	$U_{max,PIV,z}$ (μm/s)	$U_{max,PTV}$ (μm/s)	$U_{max,scan}$ (μm/s)	$U_{max,exper,x}$ (μm/s)	$U_{max,exper,y}$ (μm/s)	$U_{max,exper,z}$ (μm/s)
0.1	145	62	133	275	87	26	27
0.4	145	62	84	275	95	30	39

Pixel locking occurs in PIV applications when the subpixel interpolator breaks down, and in PTV when the centroid algorithm cannot accurately pinpoint the particle centroid. To prevent pixel locking, the ratio of particle image diameter the pixel size, $d_{\tau xy}$ for the *x* and *y* directions and $d_{\tau z}$ for the *z* direction, should be greater than or equal to 2 (Prasad et al. 1992). Using equations from Adrian (Adrian 1984, 1991) to predict the in-plane particle image diameter, $d_{Ixy,}$ and the parameters in Table 1, d_{Ixy} = 1.29 μm, and $d_{\tau xy}$ = 4.28. Similar equations exist for the particle image diameter in the *z* direction, d_{Iz}. As in the *x*-*y* direction, the particle image diameter can be approximated by a diffraction term and a term for the physical particle diameter. The diffraction term is equal to the 'airy disk diameter', which is the distance between the first minima in the point spread function. Using the relations for the point spread function of a spherical lens (Born and Wolf 1997), the airy disk diameter in the *z* direction and the corresponding equation for particle image diameter are:

$$\boldsymbol{d_{dz} = \frac{3.34 n \lambda}{NA^2}} \quad (21)$$

$$\boldsymbol{d_{Iz} = \sqrt{{d_{sz}}^2 + {d_p}^2}} \quad (22)$$

where d_p is the physical particle diameter. Equation (22) does not take into account the improvements in the point spread function granted by the confocal system (Sheppard and Choudhury 1977). Nevertheless, (22) under predicts the airy disk diameter (1.89 μm) compared with experimental measurements of the *z* direction airy disk (confocal – 4.64 μm, widefield – 6.23 μm). Using the experimental d_{dz} of 4.64 results in $d_{\tau z} = 4.2$.

In this work, the system only acquires data on the upward scan of the objective positioner. However, it is possible to acquire stacks on both the downward and upward scan of the positioner. This effectively doubles the stack acquisition rate for the same piezo travel rate. Acquiring data on both the upward and downward results in a different time between stacks (Δt_{stack}) for every slice. This can affect the ability of the measurement system to capture velocity data, by altering the dynamic velocity range depending on where in the depth the measurement occurs. For example, assuming a uniform flow, the system would be able to measure larger particle displacements in the upper portion of the channel than the lower portion (assuming that it scans from bottom to top), meaning a larger U_{max} at those planes. Another complication of acquiring data on the upward and downward scans is a reduction in the time between stacks (Δt_{stack}) for some of the slices. One effect of this could be a change in the error due to Brownian motion because Brownian uncertainty scales inversely with the time between stacks.

In summary, there are several parameters that can be adjusted to increase the maximum measureable velocity. Reducing the window size and interparticle

spacing (volume fraction) will increase the maximum velocity but reduce the spatial resolution of the measurement, which may not be desirable. For the parameters used in this work, the maximum measurable velocity is most limited by Δt_{slice}, which is limited by the confocal disk speed according to (13). Increasing the disk speed to 30000 RPM or removing the disk would allow a minimum Δt_{slice} of 16.7 ms, which would allow us to increase $U_{piezo,avg}$ to $U_{piezo,max}$ = 4000 μm/s, according to (16). Increasing $U_{piezo,avg}$ increases the maximum measurable velocity according to (18) and (19). With a Δt_{slice} of 16.7 ms, we can achieve scan rates of 60 Hz for D = 26 μm. Additionally, using channels with smaller depths will allow for 3D acquisition rates of > 60 Hz. Equation (20), which defines the maximum velocity based on the deformation of the particles, is not limiting in our system because we scan fast enough to obtain spherical images of the particles.

3.10. Motion Correction Algorithm

One result of acquiring 3D data by scanning the microchannel depth is that some particle motion occurs during the scan. For some applications, it is beneficial to know the positions of all of the velocity vectors in a 3D volume at the same instant in time. The motion of the particles during the scan can be corrected for, using the particle displacement estimate from the super resolution algorithm and the known position of the particles in the depthwise direction. The particles are corrected to the center of the depth, Z_c = 13 μm. To perform this

correction, the algorithm assumes that the particle vector does not change direction during the correction time scale. The motion correction algorithm discussed in this section was completed in collaboration with Dr. David Frakes at Arizona State University.

The motion correction algorithm corrects for the change in particle tracer position that occurs during the scan. Figure 26 shows a schematic of the displacement of the particles during the scan for a uniform flow in the *x* direction. Black particles and blue particles show corrected particle locations at the time when the piezo is focused on $z = z_c$ in two different stacks. The green particles and red particles show the measured positions of the particles.

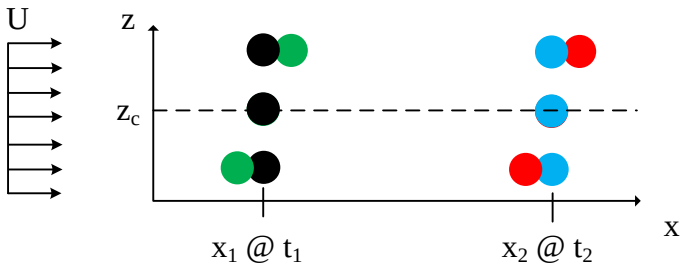

Figure 26. Schematic showing displacement of particles during scan. Black particles and blue particles show actual particle locations at the time when the piezo is focused on $z = z_c$ in two different stacks. The green particles and red particles show the measured positions of the particles which are then corrected to the actual positions using the motion correction algorithm.

The following equation is derived to estimate the position of the particles at the time when the objective is focused on the center plane of the scanned volume. To correct for the particle displacement that occurs during the translation of the objective, the particle motion estimate and the particle *z* location are used. Tracers that have large displacements and are far from the center plane require the largest corrections. The correction equation is written as,

$$\vec{X}_{cor} = \vec{X}_0 - \Delta\vec{X}\frac{(Z-Z_c)\Delta t_{slice}}{P_z} \quad (23)$$

Here, x_{cor} is the corrected position of the tracer, x_0 is the uncorrected position measured by the super resolution PIV code, $\Delta\vec{X}$ is the displacement of the particle between stacks, Δt_{stack} is the time between stacks, Z is the z position of the particle, and Z_c is the center position of the scanned microchannel. If (Z-Z_c) is positive, then the new position will be upstream of the old position. Intuitively, the magnitude of the correction decreases with increasing instantaneous piezo scan speed (P_z / Δt_{slice}) and for particle locations closer to the center vertical plane (Z-Z_c~0).

Figure 27 shows the results of the motion correction algorithm. Figure 27a – c show the x, y, and z correction ($x_{cor} - x_0$) compared to the x, y, and z displacement. Maximum position correction for the vectors in the x direction is about 0.15 µm (about 1/3 of a pixel), the y direction is 0.05 µm (about 1/10th of a pixel), and the z direction is 0.1 µm (about 1/5th of a slice). For the particle velocities and scan rates present in this study, the magnitude of the position correction is small relative to the total displacement. This means that the displacement of the particles during the scan is considerably less than the displacement of the particles between scans.

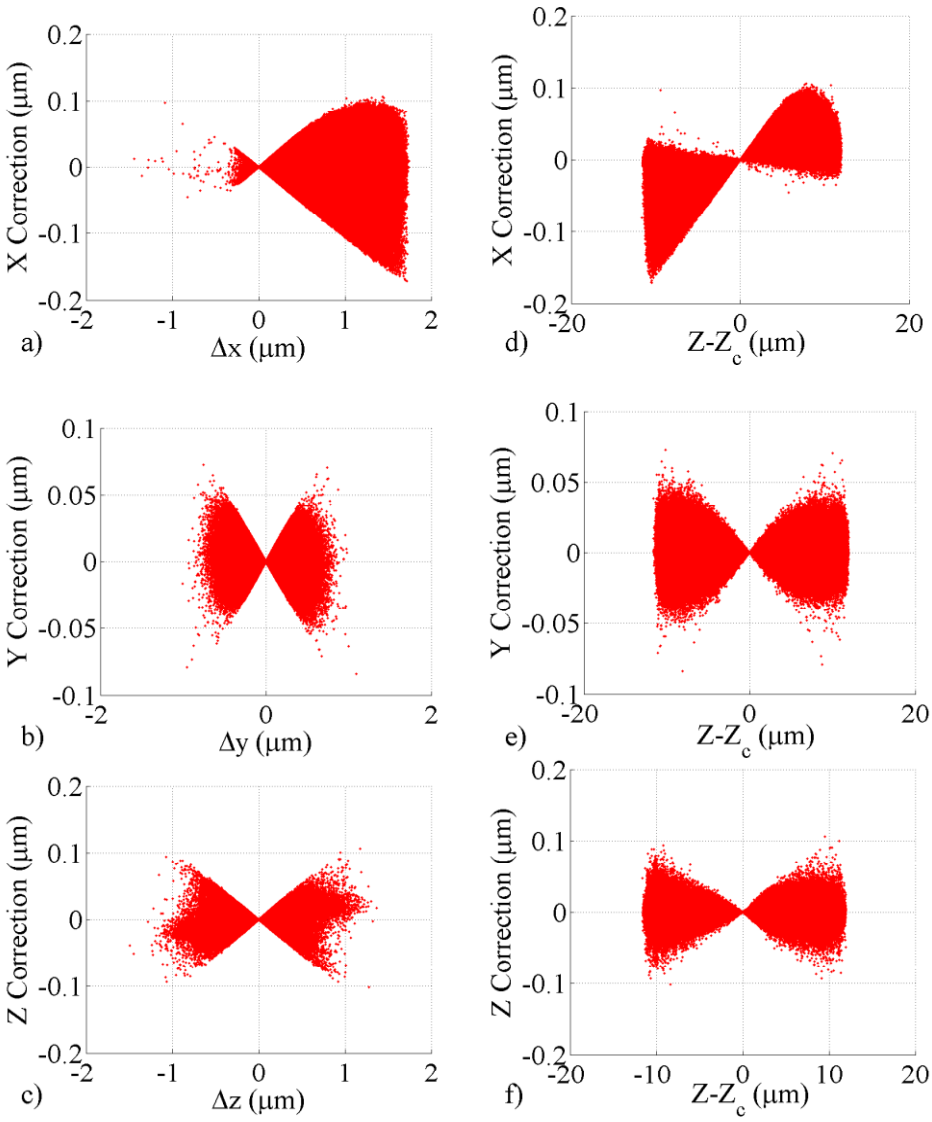

Figure 27. Results of Motion Correction algorithm. Corrections increase with increasing distance from the center plane and with increasing displacement, as expected. Corrections are small compared to displacements, indicating that the particle displacement during the scan is less than the displacement between scans.

In the next chapter, the improvement that the confocal system grants to two-frame cross correlation μPIV of unsteady microflows is quantified. The measurement system's ability to measure high speed unsteady 2D velocity fields is demonstrated by measuring the unsteady 2D2C velocity field created using an electrokinetic instability.

CHAPTER 4

IMPROVEMENT IN 2D2C TWO FRAME PIV CORRELATIONS BY CONFOCAL MICROSCOPY

4.1. Introduction

This chapter quantifies the improvement that a spinning disk confocal system grants to two-frame μPIV correlations. The impact of the optical sectioning of the confocal imaging system is quantified using the correlation space signal to noise ratio (defined as the ratio of the highest to second highest peak in correlation space) and universal outlier detection (UOD) (Westerweel and Scarano 2005). The effect of the confocal system on image signal to noise ratio (defined as the maximum image intensity divided by the mean image intensity) is well documented but also investigated here. It is shown that the confocal system generally increases the correlation S/N and reduces the percent of vectors removed during validation, depending on the particle volume fraction and focal depth. The confocal system for temporally (1250 Hz) resolved μPIV is demonstrated in an unsteady example flow created using an electrokinetic instability. Demonstrating that the confocal system can improve temporally resolved measurements for 2D2C flows is a first step to utilizing the confocal for temporally resolved measurements of 3D3C flows.

4.2. Experimental Method

Experiments were performed in Y-shaped PDMS microchannels fabricated using soft lithography. The channels have a rectangular cross-section with a width of w = 100 μm, depth d = 24 μm, and total length of 15 mm. A schematic of the

Y-shaped microchannel is shown in Figure 28 (figure not to scale). Flow is from left to right with input reservoirs at the north and south (labeled N and S) and a single output reservoir in the east (E). Pressure-driven flow was maintained by a dual-syringe pump (KDS200P, KD Scientific, Holliston, MA, USA). The syringes were connected to the chip using Tygon tubing (ID 0.02", OD 0.06", VWR, Brisbane, CA, USA) which was interfaced to the PDMS reservoirs via stainless steel tubes (0.025" OD×0.017" ID, 0.5" length, New England Small Tube, Litchfield, NH, USA).

For the electrokinetic instability measurements, electric potentials were applied using platinum electrodes (Omega Engineering Inc., Stamford, CT, USA) inserted into the Tygon tubing approximately 5 mm above the top chip surface. A negligible drop in the electrical potential between the wire insertion point and the channel entrance is expected, since the area of the tube is about four orders of magnitude larger than the cross-sectional area of the microchannel. The potential drop in the tube is estimated to be less than 0.1 V under all conditions (Navaneetham and Posner 2009). The electric potentials were applied using a high voltage sequencer (HVS448 6000D, Labsmith, Livermore, CA, USA).

4.2.1. Particle and Buffer Chemistry

Two background buffer electrolyte solutions are used. In the pressure driven flow experiments used to validate the performance of the confocal system, the background buffer solution was 0.3 mM phosphate buffer prepared by titration to pH 6 from monosodium phosphate (NaH_2PO_4) conjugate acid with disodium

hydrogen phosphate (Na_2HPO_4) conjugate base (Sigma Aldrich, St. Louis, MO, USA). For the electrokinetic instability (EKI) experiments, a lower pH buffer (pH 4) is used in an attempt to reduce the particle zeta potential and thus dampen the electrophoretic motion of the particles. For the EKI experiments, the background buffer solution was 1 mM acetate buffer prepared by titration of acetic acid (CH_3COOH) with sodium acetate trihydrate ($CH_3COONa\ 3H_2O$) (Sigma Aldrich, St. Louis, MO, USA). The buffer was titrated to a pH of 4, resulting in a conductivity of 53.5 μS/cm. This background solution was chosen as it allowed for large modifications in the bulk fluid conductivity for (by addition of KCl) and also buffered against changes in the pH due to electrolytic reactions at the electrodes.

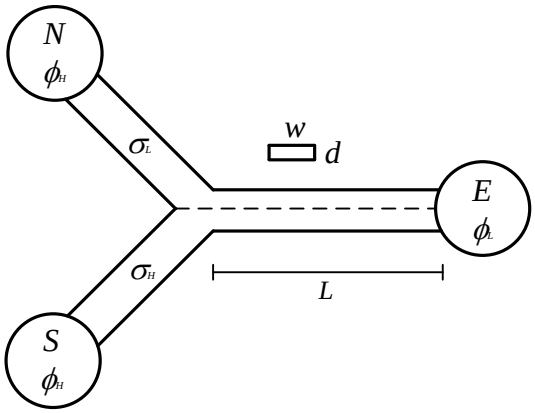

Figure 28. Schematic of *Y*–shaped microchannel. Channels are d = 24 μm deep and w = 100 μm in wide. Flow is from left to right from the north (N) and south (S) wells towards the east (E) well. The length of the straight section is L = 10 mm. In the two-frame μPIV experiments, the north and south input streams contain identical buffered colloidal suspensions. In the EKI experiments, high conductivity, σ_H and low conductivity, σ_L solutions with particles are in the south and north wells, respectively. During the EKI experiments, I apply equal high potentials φ_H at the north and south wells and low potential φ_L at the east well.

Measurements of pH and conductivity were made using a combination pH/conductivity meter (Corning, NY, USA). The buffered solutions were filtered prior to making the particle suspensions, using a 450 nm syringe filter (Millipore, Billerica, MA, USA). Fluorescent polystyrene tracer particles with excitation at 542 nm, emission at 612 nm, and diameter 500 nm were seeded into the flow (Duke Scientific, Fremont, CA, USA). The volume fraction of tracer particles was varied from 0.05% - 1.0% to study their impact on PIV correlations.

4.2.2. Microfabrication of PDMS Devices

Soft lithography of PDMS was used to fabricate the Y-shaped microchannels. Details of this process can be found elsewhere (Duffy et al. 1998), but a brief procedure is included (Navaneetham and Posner 2009; Jain and Posner 2008). Masks were produced on transparent mylar sheets using a high resolution (50,000 dpi) printing system (Fineline Imaging, Colorado Springs, CO, USA). SU-8-2025 patterned on a 4" silicon wafer served as the master for soft lithography. The surface of the master was silanized with trichloro methyl silane (TCMS) vapor for about 30 minutes. PDMS (Dow Corning Corporation, Midland, MI, USA) in a 10:1 polymer: fixing agent ratio was poured over the master, degassed at low pressure in a dessicator and baked at 80 °C in a convection oven for 60 minutes. The resultant structures were then exposed to oxygen plasma (Tegal Plasmaline Asher, Rocklin, CA, USA) at a power of 200 W and 400 mTorr pressure for 60 seconds.

4.2.3. Measurement Methodology

Steady Poiseuille flow is analyzed in a 100 μm wide by 24 μm deep microchannel as shown in Figure 28 to quantify the improvements that the confocal system provides in two frame μPIV correlations. Velocity is measured at a location 2.0 mm downstream from the channel intersection, and the input wells are connected to syringes containing identical fluids. The volume fraction of tracer particles was varied as 0.05%, 0.15%, 0.30%, 0.45%, 0.60%, 0.75% and 1.00%. Measurements were also conducted at three focal planes of 3, 12, and 21 μm, measured from the bottom surface. For each of these 21 separate test cases, the confocal and widefield systems were compared by recording 1000 raw frames, computing μPIV correlations, and generating statistics based on the correlations. The same imaging equipment and settings were used to evaluate both cases except for the insertion of the confocal disk into the optical path and the increase in the laser intensity to compensate for the lost illumination in the confocal test cases. The particle fluorescence intensity captured by the camera is carefully matched between the confocal and widefield conditions to minimize the influence of light intensity on the measurements.

Following the analysis of Adrian et al. (Adrian 1984), and using a measured total magnification of 66, numerical aperture of 1.2, a particle diameter of 500 nm, and emission wavelength of 612 nm, the number of pixels per particle (d_τ) in this work is 2.55. A d_τ of 2-3 pixels reduces pixel locking in most applications (Prasad et al. 1992). Additionally, following the analysis of Santiago et al. (Santiago et al. 1998), and using the viscosity for water at 293 K, a particle

diameter of 500 nm, a representative velocity of 0.86 mm/s, and a time interval of 5 ms, the average error due to Brownian motion is 2.28% near the center of the channel.

A recursive window PIV algorithm with interrogation window refinement was used to generate the PIV velocity vectors (Scarano and Riethmuller 1999). This algorithm uses interrogation window refinement, making an initial calculation for particle displacement in a large interrogation window and then refining the window size and displacing the refined second window by the initial calculation and re-computing the displacements. For the confocal vs. widefield experiments, initial window size was 128 by 128 pixels with two refinement steps resulting in a final window size of 32 by 32 pixels with 50% overlap.

For all experiments in this comparison, images are acquired using an exposure time of 1.2 ms and a delay between exposures of 5.0 ms. The maximum pixel displacement for a focal depth of 12 μm (in the center of the channel in depth direction) and at $y = 0$ (center channel in spanwise direction) was 16 pixels. The vector fields are validated using two criteria. The correlation map S/N ratio is used for the PVR-S/N results, using a threshold S/N of 1.2, and a universal outlier detection algorithm (UOD) is used for the PVR-UOD data, with a threshold of 2. Validation is not conducted between passes, but only at the end of the interrogations. At the maximum displacement, in the center of the channel and the center focal plane, there was a ~3 pixel blur, however this could not be avoided without introducing other complications since the exposure time was constant for all experiments. Although the blurred particles will negatively affect the

performance of the Gaussian sub pixel estimator they should not affect the results of the comparison between the confocal and widefield as the same blur should occur in both systems. A disk speed of 12500 RPM was used, corresponding to a Δt_{min} of exactly 1/3 the exposure time, preventing noise associated with partially scanned sectors.

The flow rate was set to 2 μL/hr with a corresponding Reynolds number of about 0.05. Using the maximum velocity (averaged in time) and assuming Poiseuille flow the measured flow rate is 1.99 μL/hr. Syringe pumps are known to introduce some amount of unsteadiness into the flow. By inspecting the local time averaged velocity at various points in each data set, the average RMS velocity is less than 2%, indicating that the unsteadiness caused by the syringe pump is not significant within each data set.

4.3. Results and Discussion

4.3.1. Improvement in S/N Using Confocal Imaging

The confocal system improves both image signal to noise ratio (I-S/N) and correlation map signal to noise ratio (denoted simply -- S/N). The I-S/N is defined as the maximum image intensity divided by the mean image intensity, and the S/N is defined as the ratio of the highest to second highest peak in correlation space. Figure 29 shows images of the particle tracers at a volume fraction of 0.60% and heights of 3, 12, and 21 μm for the confocal and widefield. The contrast of the images is improved for the confocal system indicating an increase in I-S/N. Figure 30 shows correlation maps for single interrogation windows for

the widefield and confocal system at 0.60% volume fraction and a height of 3 μm. Figure 30a,d shows the correlation maps for an example "good" correlation using the confocal and widefield, respectively. Figure 30b,e shows an example "poor" correlation using the confocal and widefield, respectively. Additionally, ensemble averaged correlation maps are shown using 20 different images in Figure 30c,f for confocal and widefield, respectively. Different interrogation windows will have differently shaped correlation maps, however in general the confocal system appears to improve both I-S/N and S/N. This effect is investigated further later in this section.

This section uses S/N and percent vectors removed based both on S/N (PVR-S/N) and universal outlier detection (PVR-UOD) to quantitatively compare the widefield and confocal imaging systems. An outlier detection analysis using the UOD algorithm given by Westerweel et al (Westerweel and Scarano 2005) is conducted. S/N based validation is used in this work in addition to UOD because S/N is what is expected to improve with the confocal system. Also, S/N based validation has advantages over UOD, such as being insensitive to large areas of spurious vectors and usable on the borders of the images.

Here, correlation S/N is defined as the ratio of the highest correlation peak to the second highest peak for each interrogation window (Keane and Adrian 1992; Angele et al. 2006; Scarano 2002). This chapter primarily refers to correlation map signal to noise as simply S/N. Using this definition, unity is the minimum possible S/N and a value near unity occurs when the two highest correlation peaks

are similar in magnitude. This can occur most often when both the highest and second highest peaks are poor correlations or noisy.

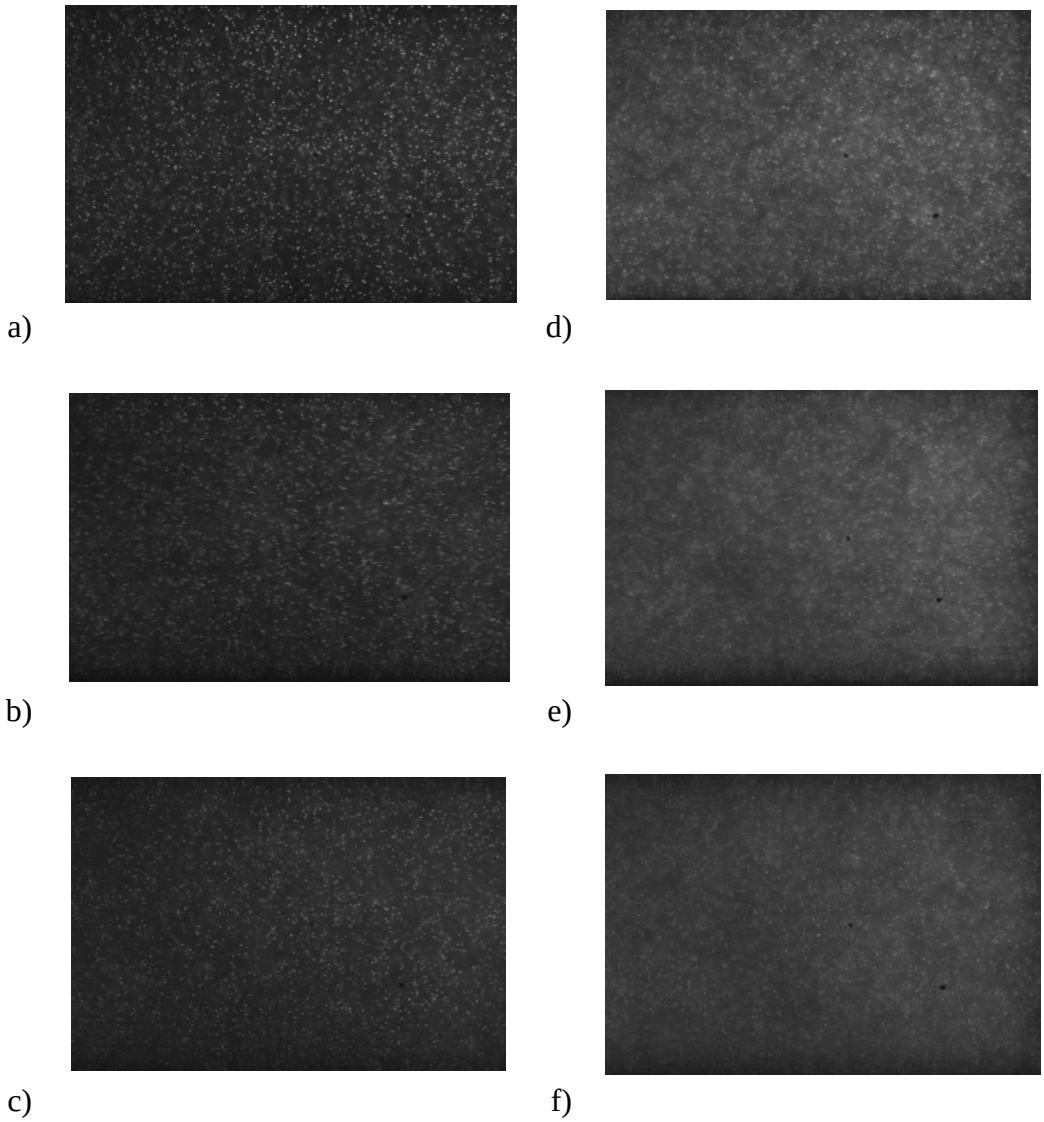

Figure 29. Particle images at a volume fraction of 0.60% for the confocal at focal depths of (a) 3 μm (b) 12 μm and (c) 21 μm and widefield at focal depths of (d) 3 μm (e) 12 μm and (f) 21 μm.

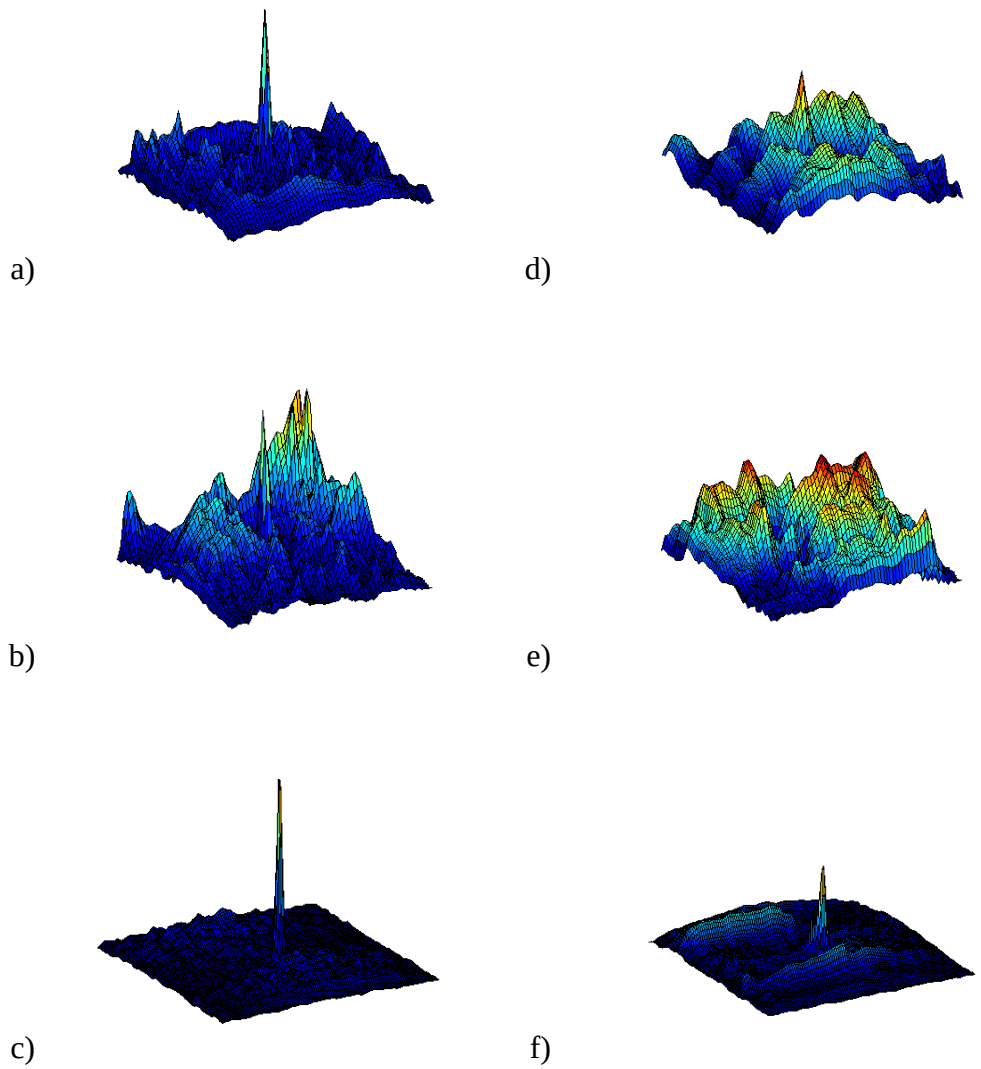

Figure 30. Correlation maps for individual interrogation windows. a) and d) show "good" correlation maps for the confocal and widefield, respectively; b) and e) show "poor" correlation maps for the confocal and widefield, respectively; and c) and f) show ensemble averaged correlation maps using 20 images for the confocal and widefield, respectively.

Under each condition tested, S/N histogram is generated and the mean S/N ($\overline{S/N}$) value is calculated. The number of vectors removed for each experiment is obtained by setting a threshold S/N value and replacing vectors that have S/N below this threshold with an average of their nearest neighbors, making the

number of removed vectors dependent on the user's choice of validation acceptable S/N. The percent vectors removed based on S/N (PVR-SN) is then calculated by taking the ratio of number of vectors removed to the total number of vectors in each experiment. As suggested by Keane and Adrian, a validation S/N of 1.2 is used (Keane and Adrian 1992). The validation threshold is an important parameter because if it is set too high, then accurate vectors are removed and there is unnecessary local velocity averaging, and if it is set too low erroneous vectors are not removed and the velocity measurement suffers. The statistics for S/N, PVR-S/N, and PVR-UOD are obtained from 1000 vector fields and over 620,000 individual correlations. Increasing the number of vector fields to 1100 changes the reported statistics by less than 1%, indicating that the results are converged.

Figure 31 shows histograms of S/N for 620,000 individual correlations at volume fractions of (a) 0.05% (b) 0.30%, (c) 1.00% using the confocal system and (d) 0.05% (e) 0.30%, (f) 1.00% using the widefield system. These histograms generally show that the confocal system increases the $\overline{S/N}$ compared to the widefield system for volume fractions greater than 0.05%. For example, Figure 31b has a $\overline{S/N}$ of 3.05 compared to the $\overline{S/N}$ for the widefield system of 2.41 shown in Figure 31e. Bimodal distributions with one peak near 1, as shown in Figure 31a, e, c, and f indicate a significant number of poor correlations for that experiment. In Figure 31a, this second peak at S/N~1 is due to an insufficient number of particles per interrogation window resulting from a low volume fraction coupled with the optical sectioning of the confocal system. In Figure 31e

and Figure 31f the peaks at S/N~1 are attributed to the increased number of out of focus particles at the higher volume fractions which reduces the signal to noise in the raw image translating to reduced S/N in correlation space. The widefield (WF) system has a lower number of poor vectors (S/N~1) than the confocal system at 0.05% volume fraction because the WF system captures a larger number of particles in each interrogation window. This is due to the increased measurement depth for the WF compared to the confocal. This effect is important in low volume fraction conditions where the number of particles per interrogation window is small (~0-2). At low volume fraction, noise from out of focus particles does not have a very strong effect on the correlations. Figure 31b shows that at 0.30% particles by volume, there is no second peak in the S/N statistics for the confocal system, suggesting a small PVR-S/N and strong correlations. As volume fraction increases to 1.00%, as shown in Figure 31c and f, a secondary peak near an S/N of unity appears for both the WF and confocal systems. This second peak is attributed to poor correlations caused by light that is captured from out of focus particles. However, the confocal $\overline{S/N}$ is significantly higher than the widefield $\overline{S/N}$, demonstrating the importance of optical sectioning of the confocal system to significantly improve S/N in two frame correlations at higher volume fractions.

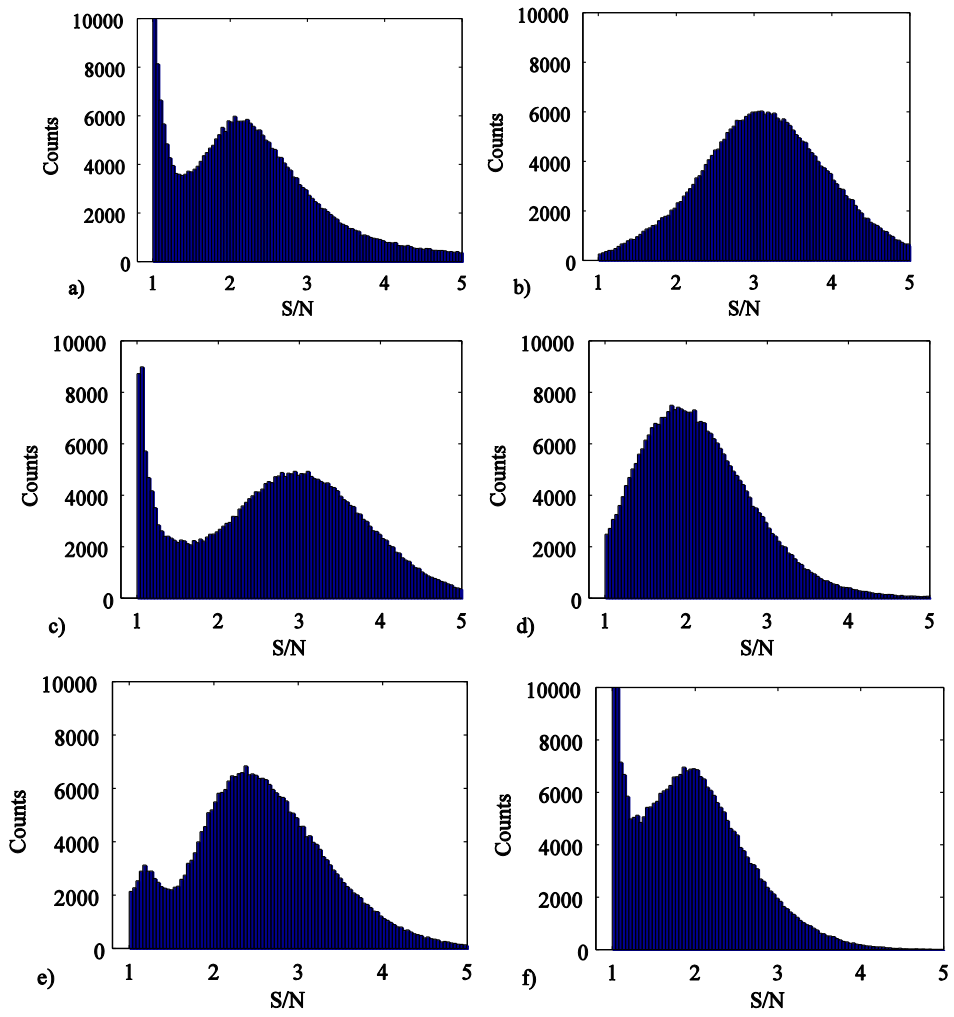

Figure 31. Histograms of correlation S/N values for the confocal (a-c) and widefield (d-f) systems at a constant focal depth of 12 um and three particle volume fractions, (a) and (d) 0.05%, (b) and (e) 0.30%, and (c) and (f) 1.00%. Each histogram is generated from 620,000 individual vector correlations. The confocal system at 0.05% particles by volume has a second peak near unity indicating a group of poor correlations as shown in (a). This second peak is due to insufficient particle seeding coupled with the optical sectioning of the confocal system. In (b), at 0.30% particle volume fraction there exists only a single peak and the confocal system exhibits a higher mean S/N than the widefield system. As the volume fraction increases to 1.00% in (c), I observe a second peak near an S/N of unity due to light from out of focus particles.

A plot of correlation $\overline{S/N}$ vs. particle volume fraction is shown in Figure 32a for the confocal and widefield systems at volume fractions from 0.05% to 1.00% and focal depths of 3, 12, and 21 μm in a 24 μm deep channel. Figure 32a shows that

the $\overline{S/N}$ increases with volume fraction until a maximum at 0.45% and then decreases. The initial increase in $\overline{S/N}$ is attributed to the increasing number of particles per interrogation window, and the following decrease to the background noise caused by out of focus particles. Figure 30b shows that the image S/N consistently decreases with increasing volume fraction, supporting this hypothesis. The error bars show one standard deviation for the 3 μm focal depth in the confocal and the 21 μm focal depth in the widefield system. The error bars are shown for only one focal depth to preserve the clarity of the figure, but the error bars are consistent across the other data sets. For all volume fractions and depths tested, the confocal system achieves greater $\overline{S/N}$ compared to the widefield system. The $\overline{S/N}$ decreases, in general, with increasing focal depth into the channel due to out of focus fluorescent particles between the objective and the focal plane.

The valid vector S/N threshold used to calculate PVR-S/N can provide information on what fraction of the correlations provide acceptable confidence to be good in resolving the local velocity vector. Figure 33a shows plots of PVR-S/N vs. particle volume fraction for the confocal and widefield systems at volume fractions from 0.05% to 1.00% and focal depths of 3, 12, and 21 μm. The high PVR-S/N at low volume fractions is attributed to low particle seeding coupled with the optical sectioning capability of the confocal system. At high volume fractions the confocal PVR-S/N increases, which is attributed to light from out of focus particles entering neighboring pinholes on the disk (Corle and Kino 1996). Figure 33a indicates that the confocal system operates optimally at a volume

fraction of 0.45%, achieving less than 1% removed vectors for all depths. The confocal system has lower PVR-S/N than the widefield system for every depth and volume fraction except at 0.05% particles by volume. The WF PVR increases more dramatically with increasing focal depth into the channel, exceeding 5% even for moderate volume fractions at deeper focal planes.

The results of the UOD analysis are depicted in Figure 33b. Between the volume fractions of 0.45% and 1.0% the $\overline{S/N}$ decreases, with a corresponding increase in PVR-UOD for the widefield system, particularly at the 21 μm depth. However, the confocal PVR-UOD stays approximately constant in this volume fraction range, indicating that the confocal system improves the PVR-UOD at high volume fractions. The confocal system improves the PIV results by achieving fewer removed vectors for larger volume fractions and deep focal planes. However, for low volume fractions and shallow focal planes where there are fewer out of focus particles to degrade the S/N ratio the WF system performs better (fewer removed vectors) based on the UOD criterion. For volume fractions > 0.45%, the confocal system outperforms the widefield system at every depth. The PVR-UOD for the WF system exceeds 10% for the 21 μm depth and 1.0% volume fraction, whereas the confocal system achieves less than 4% PVR-UOD.

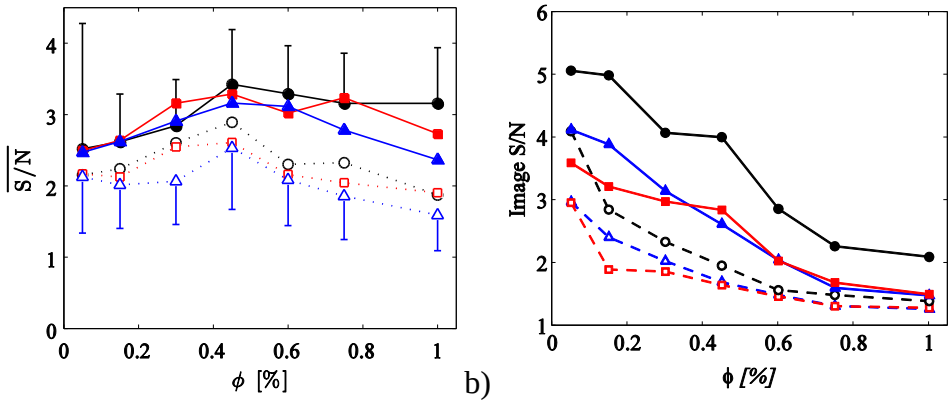

a) b)

Figure 32. a) Mean correlation signal to noise ratio, $\overline{S/N}$, for confocal (filled) and widefield (open) systems as a function of the particle volume fraction φ and three focal depths of 3 (circle), 12 (square), and 21 μm (triangle). b) Image signal to noise ratio as a function of volume fraction, with the same symbols as a).

Figure 34 shows plots of the normalized streamwise *u* and spanwise *v* velocity for the confocal and widefield systems along with an analytical solution for the flow in a rectangular duct (Shah and London 1978). These velocity profiles are generated from spatially averaging a single invalidated (no vectors removed) two-frame velocity field in the streamwise direction. Park et al. showed that confocal systems more accurately measure ensemble averaged velocity fields due to the reduction in depth averaging and improves the confocal image (Park, Choi, and Kihm 2004). Here, the capability of the WF and confocal systems for making two frame measurements is compared and the two frame velocity fields are related to the statistics for PVR and correlation S/N. Figure 34 shows that confocal system measurements deviate less from the theoretical solution compared to the widefield system.

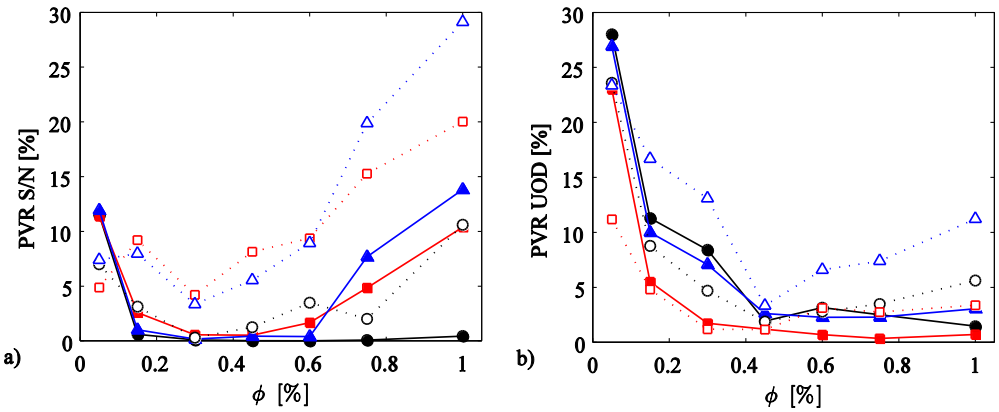

Figure 33. Percent vectors removed based on (a) S/N (PVR S/N) and (b) UOD (PVR-UOD) for the confocal (filled – solid line) and widefield (open – dotted line) systems as a function of volume fraction and three focal depths of 3 (circle), 12 (square), and 21 μm (triangle). Vectors are considered erroneous when their correlation S/N value is below 1.2 and the UOD detection threshold is set to 2.

Figure 34a, b, and c show the streamwise *u* velocity for the confocal and widefield systems compared with the analytical solution for particle volume fractions of 0.05%, 0.45% and 1.00%, respectively. For particle volume fractions at 0.45% and 1.00% the confocal system velocity profile more closely follows the shape of the analytical profile and has fewer erroneous velocity values than the widefield system. However, Figure 34a shows that the widefield system more closely follows the calculated profile for the 0.05% volume fraction due to a large number of erroneous vectors for the confocal system. Erroneous vectors have a significant effect in the measurement of the spanwise *v* velocity profiles as shown in Figure 34e, f, and g for particle volume fractions of 0.05%, 0.45%, and 1.00%, respectively. Here the spanwise velocity is normalized by the maximum streamwise *u* velocity for that data set. The confocal system measures nearly zero spanwise velocity direction velocity at 0.45% and 1.00% particle fractions, measuring a maximum spanwise velocity of 1.2% of U_{max} for the 0.45% volume

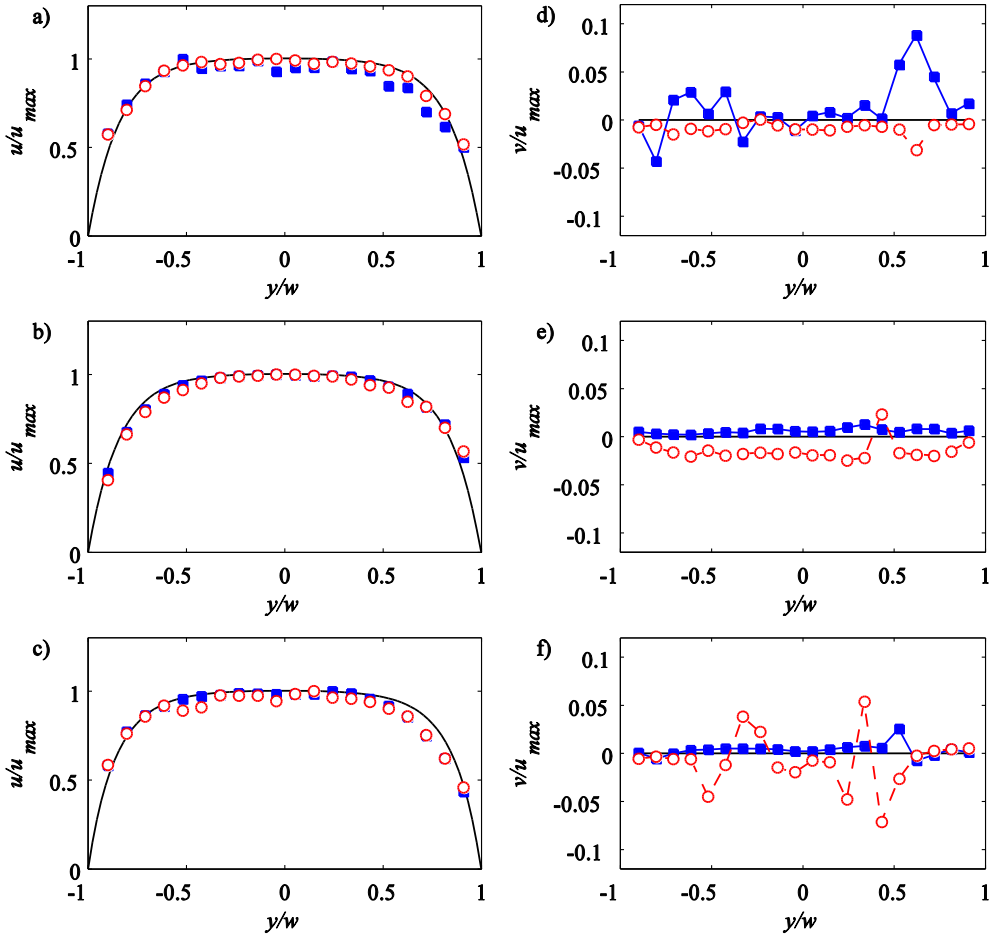

Figure 34. Measured and computed (solid black line) streamwise (a-c) and and spanwise (d-f) velocity profiles using the confocal (filled squares) and widefield (open circles). Profiles recorded at focal depth of 12 μm and particle volume fractions of (a,d) 0.05%, (b,e) 0.45% , and (c,f) 1.00%. PIV data is taken from a single two frame cross correlation spatially averaged in the streamwise direction over 10 streamwise locations.

fraction. The widefield system has larger deviations from nonzero velocity for these volume fractions, measuring up to 3% of U_{max} for 0.45% volume fraction and over 7% of U_{max} for 1.00% volume fraction, but smaller deviations from nonzero velocity measurements at a particle volume fraction of 0.05% compared with the confocal. The results from Figure 34 are consistent with the results from the $\overline{S/N}$ and PVR analysis. The confocal system was found to more accurately

(fewer erroneous vectors) measure Poiseuille flow than the widefield system for high volume fractions. In the next section, a spinning disk confocal μPIV system is utilized for measuring time-resolved unsteady flow fields created using an electrokinetic instability.

4.3.2. Demonstration of 2D High Speed Confocal PIV System on Unsteady Microflows

Electrokinetic instabilities (EKIs) are caused by a coupling of electric fields and ionic conductivity gradients that results in an electric body force (per unit volume) of the form $\rho_e E = (\varepsilon E \cdot \nabla\sigma / \sigma)E$ where ε, E, and σ are the local permittivity, electric field and ionic conductivity, respectively. Electrohydrodyamic (EHD) instabilities were first observed by Melcher and Taylor in the late 1960s (Melcher and Taylor 1969). Hoburg & Melcher (Hoburg and Melcher 1976) performed experiments in dielectric liquids (corn oil) which always resulted in unstable flows. More recently, there has been interest in electric-field-induced instabilities in microchannels, in part due to the importance of electric-field-driven transport in micro total analytical system (μTAS) devices (see (Chen et al. 2005; Ozen et al. 2006; Posner and Santiago 2006)). This work in electrolyte systems is distinct from EHD instabilities performed in dielectric liquids in that they are conducted in miscible, high-ionic-conductivity electrolyte solutions in which ion diffusion is important. EK instabilities are distinguished from EHD instabilities by the importance of the smearing of conductivity interfaces by ionic diffusion, the role of electroosmotic (EO) flow in advection

and the conditional instability that depends on the electric field and conductivity gradient magnitude. A diffuse interface results in conditional stability that primarily depends on the applied field and the magnitude of the conductivity gradient. Electrokinetic flows with conductivity gradients become unstable when the electroviscous stretching and folding of conductivity interfaces grows faster than the dissipative effect of molecular diffusion (Posner and Santiago 2006). Numerous linear stability analyses (Baygents and Baldessari 1998; Chen et al. 2005), numerical simulations (Lin et al. 2004; Oddy and Santiago 2005; Santos and Storey 2008; Storey 2005), and detailed experimental investigations (Oddy, Santiago, and Mikkelsen 2001; Chen et al. 2005; Posner and Santiago 2006; Navaneetham and Posner 2009) collectively provide a fundamental understanding of EKIs, identify key controlling parameters, predict qualitative flow features, describe the critical conditions required for instability, and demonstrate nonlinear chaotic flow. Lin (Lin 2009) reviews the contributions and remaining challenges of electrokinetic instabilities.

EKIs have been studied quantitatively by various groups using various tools. Measurements are conducted of the time varying velocity field of EKIs in a *Y*-shaped microchannel with a single conductivity interface. One of the primary assumptions of PIV is that the particles follow the local fluid flow. In electric field-driven flows, charged particles will have an electrophoretic migration velocity parallel to the local electric field vector. The velocity measured by PIV in electrokinetic flow is the total velocity which is has contributions from both the bulk flow as well as the drift electrophoretic velocity. Uncharged particles would

not have a drift velocity, but would result in rapid aggregation and fouling of the channel walls. The most straightforward method to determine the true electro-osmotic velocity field in an electrokinetically driven flow is to subtract the electrophoretic velocity component, which can be calculated if the particle zeta potential, ζ_p, and local electric field are known (Devasenathipathy, Santiago, and Takehara 2002; Ichiyanagi et al. 2009). In order to measure transient velocity fields during the start up of an electrokinetically driven flow, Yan et al. developed a method that utilizes the different time scales between electro-osmosis and electrophoresis (Yan et al. 2006; Yan et al. 2007).

The average zeta potential of the particles was measured using a dynamic light scattering (DLS) instrument (PSS Nicomp, Santa Barbara, CA, USA). Particle zeta potential measurements were made at a particle volume fraction of 0.002%, which is much smaller than the particle volume fraction used for the EKI experiments (0.30%). Zeta potential for charged particles is known to vary with ionic strength and pH (Bolt, Goodwin, and Ottewill 2005; Hunter 1981) as well as particle volume fraction (Hunter 1981). The variation in particle mobility, μ, for varying volume fraction, φ, has been shown to follow the relation $\mu/\mu_o = (1-k\varphi)$ where μ_o is the dilute mobility and k is a constant (Zukoski and Saville 1987). Since the mobility is directly dependent on the zeta potential, the zeta potentials of the particles should follow this trend. Navaneetham and Posner have measured μ/μ_o for particle volume fractions from 0 to 2.0% for the particles used here (500 nm polystyrene) (Navaneetham and Posner 2009). They found that the mobility ratio obeyed the expression $(1-k\varphi)$, but that k was small such that there was little

to no variation in mobility over these volume fractions for 500 nm polystyrene particles in phosphate buffer solution.

An electrokinetic instability is used to demonstrate the measurement of an unsteady flow field with high temporal resolution. EKIs are an example flow which consist, in this case, of the superposition of pressure driven and electroosmotic flow fields with an electrophoretic particle drift velocity. The existing methods for determining the electrokinetic velocity field can only be implemented for steady flows without variations in ζ_p. For this reason, electrophoretic component of the flow is dampened using buffer chemistry. In an effort to reduce the effect of the electrophoretic drift velocity low pH buffers are used to obtain a low zeta potential. Here a pH of 4 is used, which results in an average zeta potential of -52.9 ± 3.80 mV as measured by using DLS in the low conductivity solution. This potential is about 30% less than the zeta potential of the particles at pH = 7.5 (-73.4 ± 1.27 mV). At lower pH and zeta potentials the particles can aggregate and settle, making the measurements impossible. The chosen pH of 4 offers a good compromise between ensuring particle stability and dampening electrophoretic velocity. Additionally, the zeta potential and therefore electrokinetic velocity of the particles will be different for the different conductivity streams. I am aware that this affects the velocity measurement, but nevertheless do not compensate for this effect. The EKI is used to obtain an unsteady microscale flow with which to demonstrate high-speed, time resolved velocity measurements and the goal is not a thorough analysis of the velocity field in EKIs.

A high conductivity solution flows from the south well (50 μL/hr) and a low conductivity solution (50 μL/hr) from the north well towards the east well. The low conductivity solution is the buffer described in section 2.2. The high conductivity solution contains potassium chloride (KCl) and has a conductivity of 442 μS/cm, yielding a conductivity ratio of 8.21. Images are recorded 3.4 mm downstream from the Y intersection. Both solutions contain tracer particles at a volume fraction of 0.30%. A framerate of 1250 fps with an exposure time of 400 μs resulted in PIV vector fields with 800 μs temporal resolution. Although this exposure time corresponds to an achievable framerate of 2500 fps, an inter-frame time corresponding to 1250 fps is used to allow sufficient particle displacement between frames to obtain low uncertainty, but not too high of a displacement that the particles can no longer be correlated or do not represent the local Eulerian velocity (Scarano and Riethmuller 1999). The inter-frame times used here result in a maximum pixel displacement of 16 pixels, which is 1/4 of the initial interrogation window size and less than the maximum allowable in-plane displacement of 30% of the interrogation window (Keane and Adrian 1993). There is slight blurring that results in the areas of maximum displacement, however, these areas are few, and the average displacements are smaller in magnitude with less blur. The initial interrogation window size is 64 by 64 pixels with two refinement steps resulting in a final window size of 16 by 16 pixels with 50% overlap, producing vector fields with 4.9 by 4.9 μm spatial resolution.

Figure 35a shows the instantaneous velocity field of an electrokinetic instability (EKI) for an applied electric field strength of 1866 V/cm and a focal

plane depth of 11 μm from the bottom wall of the channel. The contour maps in Figure 35a and b are instantaneous vorticity maps normalized by the maximum vorticity of 650 s^{-1}. Shown to the bottom-left of the vector field in Figure 35a is a scalar representation of a similar instability imaged using uncharged Rhodamine dye at the same electric field and in the same microchannel at reduced magnification (10x). Figure 35a displays a crashing wave in the instability similar to the type seen in the scalar image. High positive vorticity can be seen on the top of the wave and high negative vorticity along the bottom, denoting counter rotating vortices. Strong vortical motion can be observed in Figure 35b where the instantaneous velocity has the time-ensemble averaged velocity field subtracted.

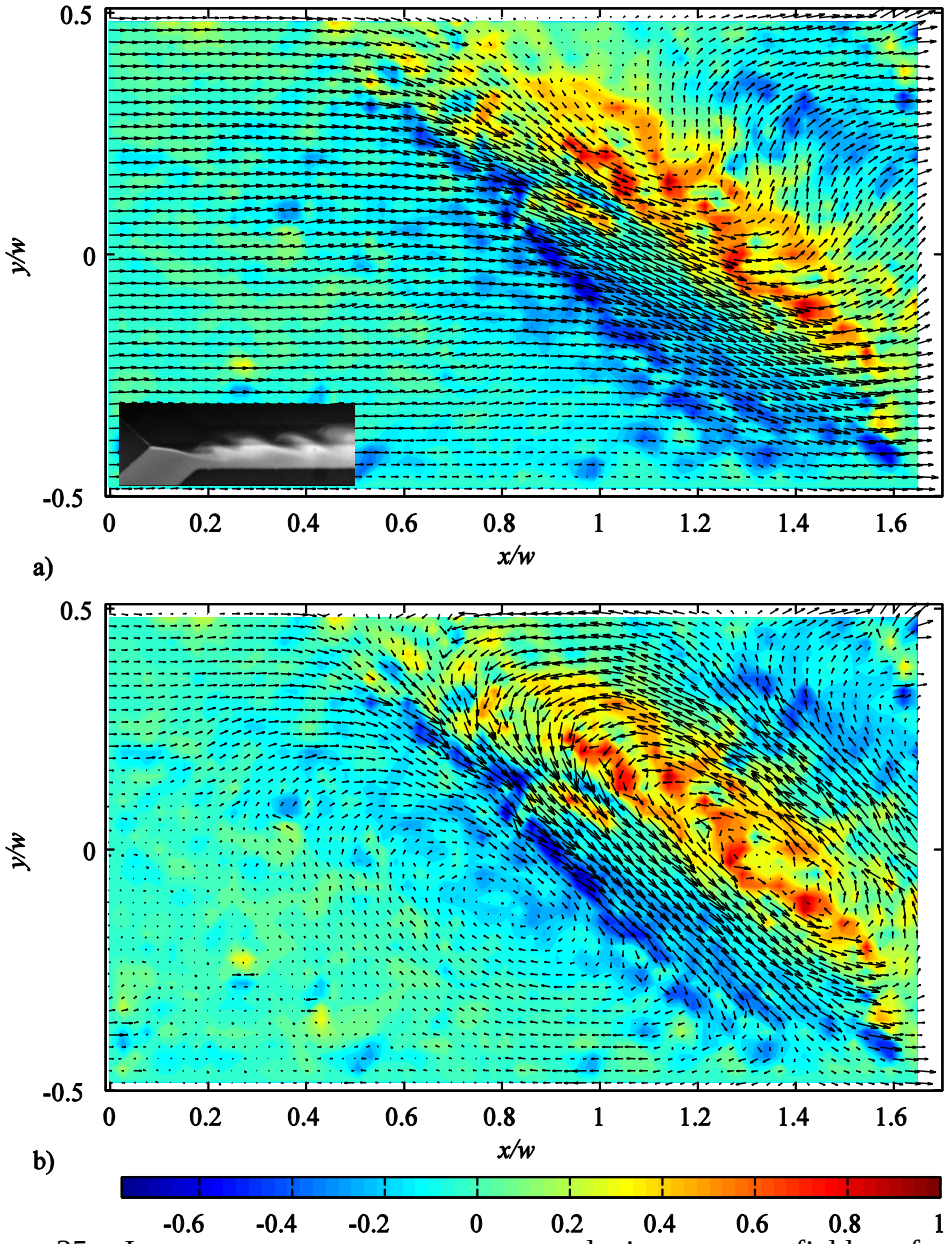

Figure 35. Instantaneous two-component velocity vector fields of an electrokinetic instability calculated from two-frame cross-correlations using a spinning disk confocal microscope is shown in (a). The contour map shows the vorticity and a scalar image is shown in the lower left hand corner. The velocity field with the average velocity field subtracted in shown in (b). Applied electric field strength is 1866 V/cm with a conductivity ratio of 8.21. Wave-like motion is observed in (a) with positive vorticity on the upper part of the wave with negative vorticity below.

When the μPIV data is animated in time, vortices of the type seen in Figure 35b periodically advect through the field of view. Figure 36 depicts the velocity magnitude RMS calculated using 1000 vector fields. The RMS field is normalized by the absolute maximum velocity of 7.5 mm/s. The RMS shows that the fluctuations are largest at the conductivity interface ($y/w = 0$) where strong electric body forces are expected. These measurements of unsteady EKI flows demonstrate that spinning disk confocal μPIV can be used to obtain high S/N correlations of microscale flows using two-frame correlations. I have demonstrated that the system can temporally resolve the unsteady microscale flow field with confocal μPIV at a frame rate of 1250 fps and 400 μs exposure times.

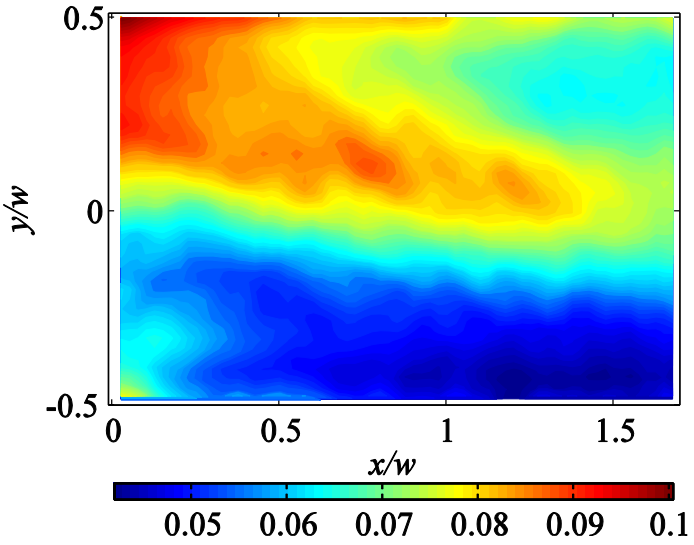

Figure 36. Velocity magnitude RMS for an applied field of 1866 V/cm and conductivity ratio of 8.21. The RMS values are normalized by the maximum velocity in the flow (7.5 mm/s). The RMS shows that the largest velocity fluctuations are near the conductivity interface at y/w=0.

4.4. Summary

Statistics of correlation S/N and PVR-SN show that the confocal system improves μPIV correlations over a wide range of particle volume fractions and imaging depths. UOD analysis shows that the confocal system outperforms the WF system at the 21 μm focal plane for every tested volume fraction. Additionally, the confocal system performs better than the WF at all focal planes for volume fractions > 0.45%.

As long as adequate particle seeding is used and enough excitation light is available, confocal systems should improve temporally resolved μPIV measurements for cases where there are many out of focus particles, such as when high NA objectives, deep channels, and high seeding densities are used. The increase in signal to noise ratio of two frame correlations provided by the confocal system facilitates the measurement of flow fields with less removed vectors and could possibly lead to higher spatial resolution by allowing higher particle volume fractions to be acceptably used and therefore smaller windows. However, since the disk speed limits the minimum exposure time, these systems cannot currently be used for flows that require extremely short exposure times (< 333 μs) or high frame rates (> 3000 Hz). Additionally, if the particle volume fraction is low, then the confocal system can be detrimental by reducing the number of particles per window in the system.

This chapter has demonstrated the use of the two frame high–speed SDμPIV system to measure the time-resolved unsteady velocity field of an electrokinetic instability. The vorticity and average subtracted velocity fields qualitatively agree

with the scalar images. The RMS velocity field shows that the largest fluctuations occur in the region of the conductivity interface. Since these velocity fields are a superposition of pressure driven, electro-osmotic, and electrophoretic flow fields, they should not be inferred as a precise measurement of the fluid velocity, but rather as representative sample of an unsteady EKI flow field.

In the next section, I present 3D3C measurements of the velocity in a depthwise expanding microchannel with the goal of validating the volumetric 3D3C super resolution PIV measurement system.

CHAPTER 5

3D3C VELOCIMETRY IN AN EXPANDING CHANNEL

5.1. Introduction

This chapter quantifies the ability of the volumetric scanning super resolution confocal PIV system to measure temporally resolved measurements of three-component three-dimensional microflows. The steady flow in a microchannel with an depthwise and spanwise expanding section is investigated. The temporal resolution of 3D confocal depth scanning (Besseling et al. 2009) is improved using a high speed Nipkow disk based confocal system, a piezo actuated objective positioner, a high speed camera, and timing equipment, allowing the capture of 3D stacks at 30 Hz (or higher for smaller channel depths than used here) and 2D confocal images at up to 3000 Hz. A 3D3C variant of super-resolution PIV estimates the flow velocity (Keane, Adrian, and Zhang 1995) improving the spatial resolution compared to PIV or PTV alone. Experimental measurements of the 3D3C flow field in an expanding channel are acquired at 30 Hz and compared with a computational simulation of the flow field. Particle traces and vector fields demonstrate temporally resolved velocity measurements that compare well the simulations. A motion correction algorithm corrects the positions of the vectors for their displacement during the scan. Three-dimensional three-component super resolution measurements are shown to result in less outliers and larger maximum velocities compared to PTV alone. Gridded vector plots and line profiles of

velocity show quantitative comparison between the simulated and experimental flows.

5.2. Microchannel Fabrication and Geometry

A 3D polydimethylsiloxane (PDMS) microchannel with T-shaped depthwise and spanwise expanding section is shown in Figure 37. This geometry provides a flow field with three components of velocity, allowing validation of the method. Figure 37 shows the microchannel intersection at the midpoint of the 1 cm total length. The height of the lower section D_2 is 10 μm and the height of the upper section D_1 is 16 μm for a total height of 26 μm. The T channel is W_c = 40 μm wide long, and both the length of the expanding section and width of the lower channel are W = 80 μm. The chamfers shown are an artifact of the fabrication process.

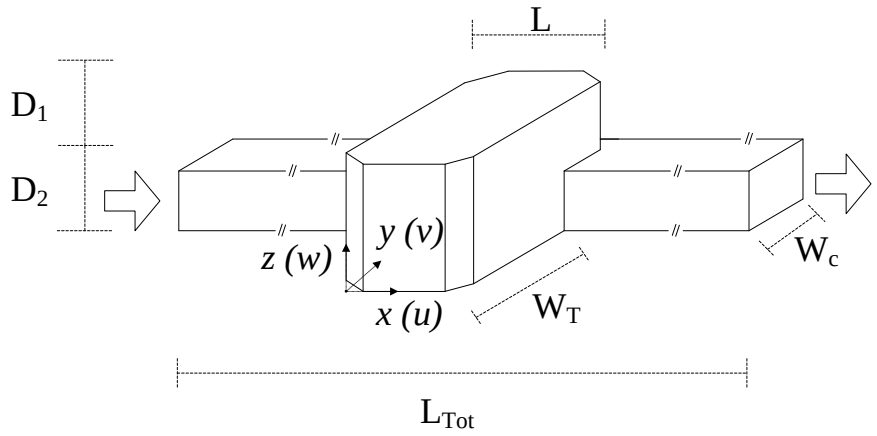

Figure 37. Geometry for the 3D microchannel. In this work, L_{Tot}= 10 mm, $L = W_c$ = 80 μm, D_1 = 16 μm, D_2 = 10 μm, and W_T = 40 μm. Flow is from left to right (in the positive *x*-direction). The dimensions for the field of view used in the experiments are L = 80 μm, W = 120 μm, and D = 26 μm.

The channel is patterned using two level SU8 photolithography (Anderson et al. 2000). The methodology for the fabrication process is depicted in Figure 38.

First, SU8 2010 photo resist is spun onto a silicon wafer, baked for 6 minutes at 95 º C, and exposed to 400 mJ/cm^2 of UV light for 30 s. After a post exposure bake at 95 º C for 6 minutes, the same wafer is spun with another layer of photoresist and baked. A contact aligner (HTG System III, San Jose, CA) aligns the second mask to the first level structures. Only the alignment marks are developed with drops of SU8 developer solution for 20 minutes to make the registration (alignment) step easier. The registration step is normally difficult due to the low contrast of undeveloped structures. After registration, the master is exposed to UV light at 400 mJ/cm^2 for 30 s and baked for 6 minutes at 95 º C on a hotplate. SU8 developer solution develops the master by light agitation in a small dish. A profilometer (DekTak II, Plainview, NY) measures the SU8 channel heights. The flow field simulations use this geometrical information to create the computational domain (see section 5.3). A 10:1 mix (PartA:PartB) of PDMS elastomer is poured over the master after silanization in tri-chloro-methyl-siloxane (TCMS). TCMS helps prevent the PDMS from adhering to the photoresist.

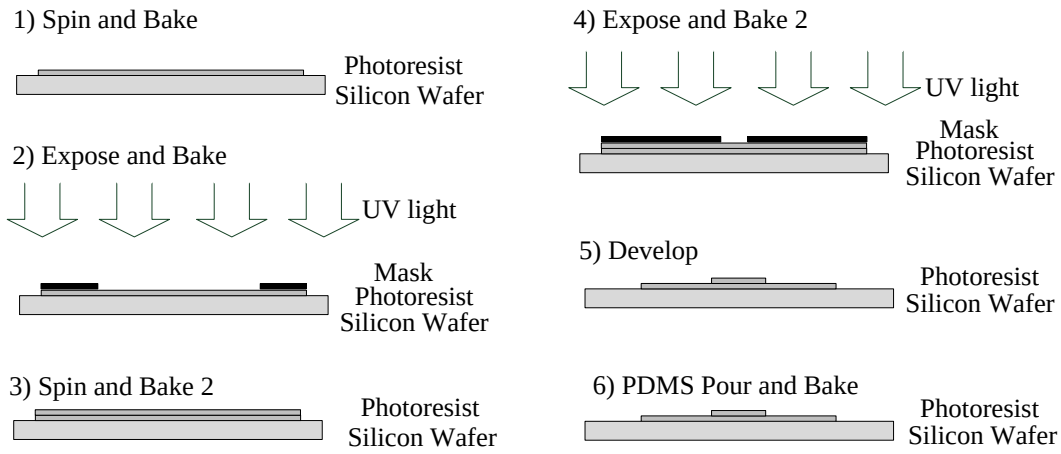

Figure 38. Schematic of soft lithography process for microchannel fabrication.

5.3. Simulation Methodology

The experimental velocity measurements are compared with computational fluid dynamics (CFD) simulations. The simulations were carried out with the assistance of a collaborator, Jeffrey L. Moran. The flow is simulated in a 3D domain with dimensions identical to those in Figure 37, with a working fluid of pure water at room temperature. Any variations in viscosity or density caused by the presence of the particles and sucrose are ignored. The simulations are conducted using COMSOL multi-physics finite element software. The Reynolds number is on the order of Re ~ $2\text{x}10^{-3}$, and therefore the steady, incompressible Stokes equations are solved,

$$\begin{aligned} \nabla \cdot \vec{u} &= 0, \\ \nabla p &= \mu \nabla^2 \vec{u}, \end{aligned} \qquad (24)$$

to obtain the velocity and pressure fields. The no-slip boundary condition, $\vec{u} = 0,$ is applied on all interior channel walls. As in the experiments, an applied pressure gradient drives the flow in the simulations. The pressure gradient is set such that

the u (streamwise) velocity at the midpoint of the T-section (x = 40 μm, y = 60 μm, z = 13 μm) in the simulation data matches with the velocity at the same location in the experimental data. This one point calibration allows us to match the velocity profiles without having to measure the volume flow rate in the experiments.

5.4. Experimental methodology

Images of 1 μm diameter particle tracers flowing through the microchannel are acquired at the location of the T expansion shown in Figure 37. The density of the water (.988 g / cm^3) is matched to the density of the particles (1.05 g / cm^3) by adding sucrose (2.125 g / cm^3) to reduce the settling the velocity of the particles. Experimental data is presented at volume fractions of φ = 0.004 and φ = 0.001. The flow rate is set to 5 μL/hr. The slice exposure time, number of slices per stack, and number of stacks per experiment are 330 μs, 25 slices, and 640 stacks, respectively. The microchannel has a total height of 26 μm in the expansion so the slice spacing, P_z, is 1.04 μm. The system is configured to collect a stack on only the upward scan of the positioner as explained in section 3.9. The positioner scans at a rate of 30 Hz, and the camera frame rate is set to 3000 Hz.

See section 3.6 for an explanation of the camera and piezo synchronization procedure and section 3.9 for equations that predict the limits of parameters for the system.

5.5. Volumetric time resolved micro particle velocimetry

The method measures temporally resolved 3D3C super resolution PIV measurements in a microchannel flow. Figure 39 shows isosurfaces of particle image intensity superimposed with temporally resolved particle tracks. The simulation of the flow field is included for comparison. The isosurface algorithm allows direct visualization of the Lagrangian particle motion. Both the top and side views show agreement between the experimental data and the simulation. The particle motion is as expected, with the particles expanding outward into the T and upward into the expansion, following the streamlines of the flow. Brownian motion can be detected in the particle trajectories, exhibiting the system's ability to measure temporally resolved flows. The viewing angle of the experimental data is completely adjustable, and a movie of the particle motion with a rotating view is available in the supplementary information of Klein et al. (Klein et al. 2011). Instantaneous vector fields at φ = 0.001 and φ = 0.004 are shown in Figure 40a and Figure 40b respectively. Spatial resolutions in PTV techniques can be reported as either time averaged or time resolved. Time averaged spatial resolutions can only be reported for steady or periodic flows, and can be increased (magnitude reduced) by an arbitrary amount depending on the amount of time data is acquired for. For this reason, the time resolved or instantaneous spatial resolution is reported for this technique. At a temporal resolution of 33 ms, the technique achieves an instantaneous spatial resolution of 2.8 by 2.8 by 2.8 μm at φ = 0.004 and 4.5 by 4.5 by 4.5 μm at φ = 0.001. The spatial resolution reported here is estimated from the interparticle spacing

estimate and without any averaging of velocities. Particle volume fraction also directly affects the spatial resolution and maximum measurable velocity in this method, as it does in all particle tracking velocimetry techniques. As particle volume fraction increases, the interparticle spacing and therefore the spatial resolution becomes finer. Spatial resolution is not optimized here, and higher spatial resolutions can be achieved. The maximum measurable velocity of the system is discussed in section 3.9.

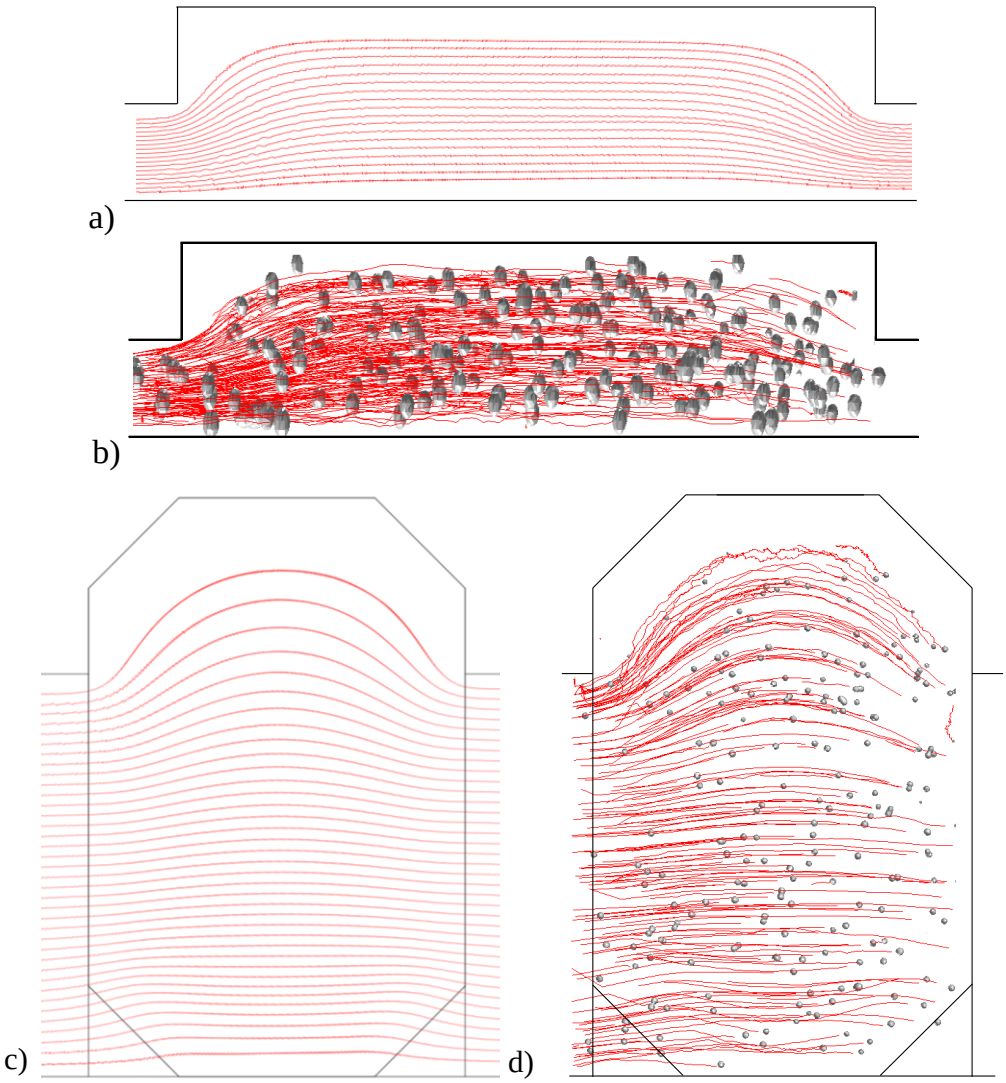

Figure 39. Time resolved 3D particle tracer images created using isosurfaces with 3D3C trajectories shown at 0.1% volume fraction. a) Computational side view and b) experimental side view, as well as c) computational top view and d) experimental top view, show good agreement.

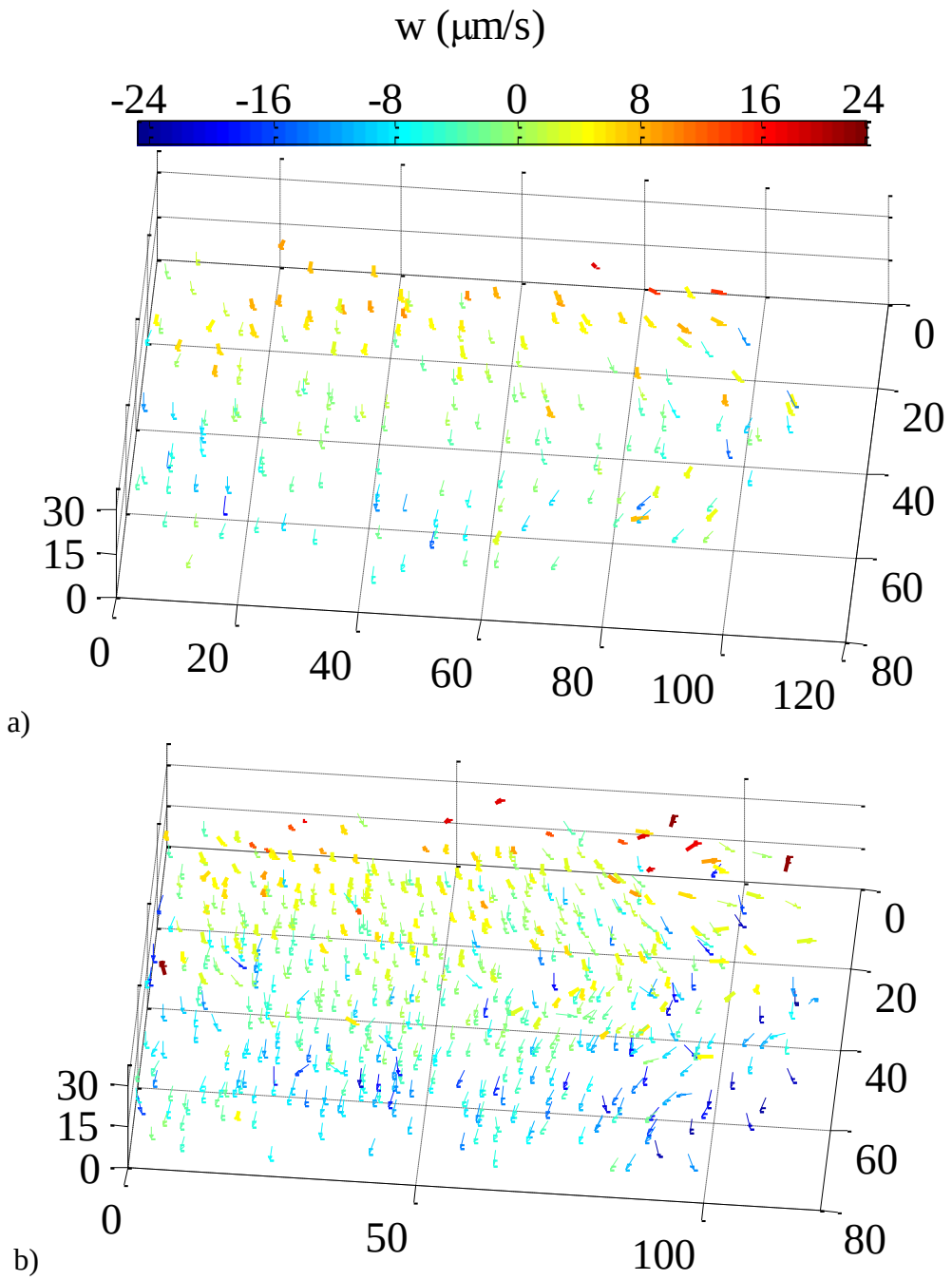

Figure 40. Time resolved 3D vector fields shown at an isometric view for a) 0.1% volume fraction and b) 0.4% volume fraction. The 0.4% case has many more vectors than the 0.1% case, but also has more erroneous vectors.

5.6. Quantitative Comparison Between Experiment and Model

Here, super resolution and classic PTV velocity measurements are compared using scatter plots. The velocity component (*u*,*v*, or *w*) to plot is chosen as well as

the coordinates for the line. For example, in the case of Figure 41a, I plot *u* along the *x* direction at location of *y* = 60 μm and *z* = 7.5 μm. To construct these plots, I choose the coordinates for the line, and then collect all velocities whose coordinates fall within ±5% of full range of the chosen coordinates (for *y* and *z*, 5% of 120 and 26 μm respectively). Figure 41 shows line plots for super resolution (a-c) and classic 3D PTV (d-f). Figure 41a and Figure 41d show *u* vs. *x* along the line at *y* = 60 μm, *z* = 7.5 μm. Figure 41b and Figure 41e depict *u* vs. *z* at *x* = 40 μm, *y* = 60 μm, and Figure 41c and Figure 41f show the *w* vs. *x* velocity at *y* = 60 μm, *z* = 6 μm. From Figure 41 it is clear that the PIV predictor field used in super resolution PIV allows the measurement of larger magnitude velocities compared to PTV for the same search radius. Classic PTV cannot accurately resolve the velocity in Figure 41d nor Figure 41f, but does resolve the velocity in Figure 41e. However, in Figure 41e and Figure 41d there are more outliers for the PTV algorithm compared with super resolution. This effect is seen in other data sets as well, as expected. The use of an accurate PIV predictor field should help prevent mistracked particles, because the algorithm has a guess of where the particle will be in the next frame and doesn't search in the wrong direction.

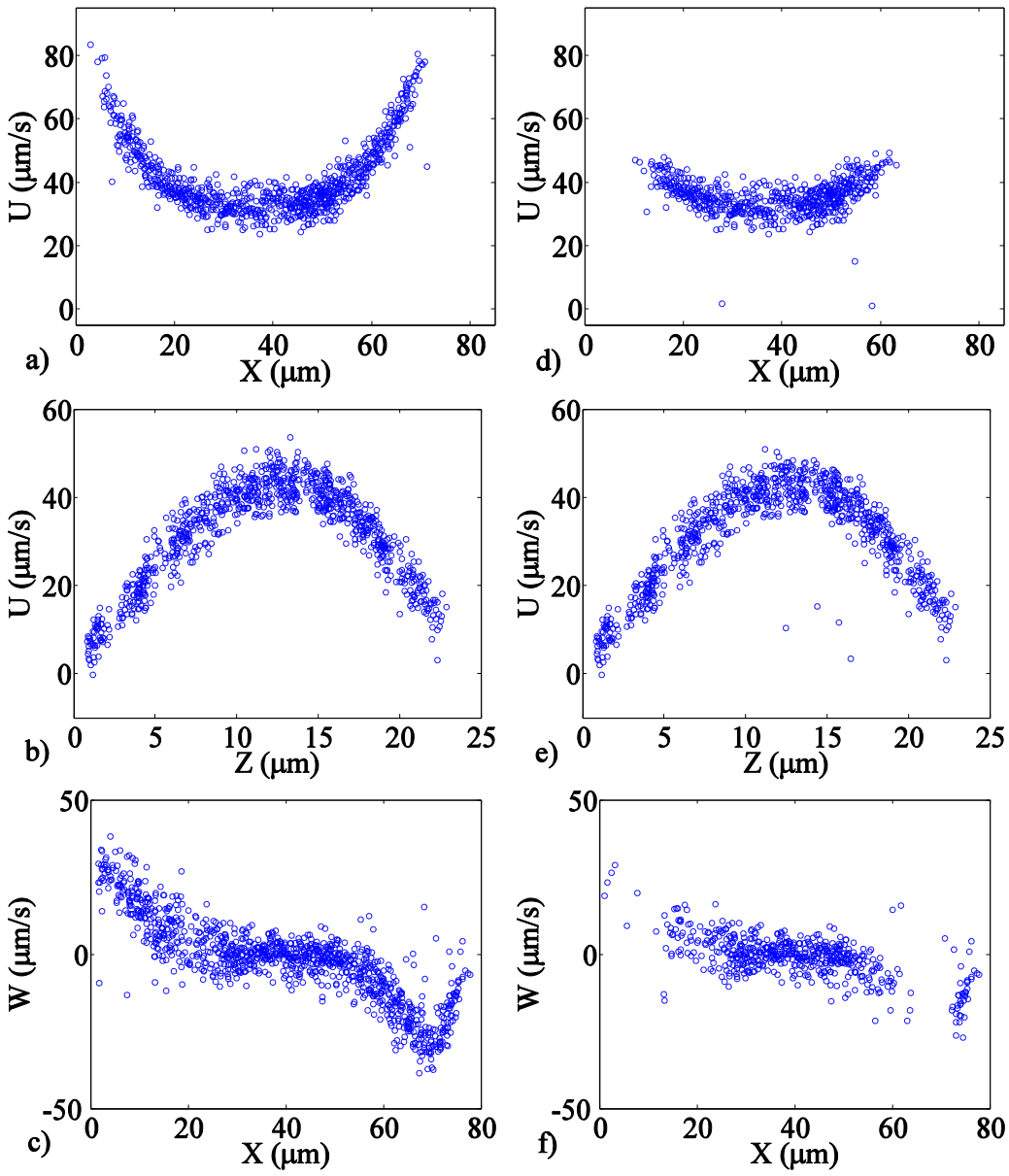

Figure 41. Scattered data line plots comparing super resolution algorithm (left) to traditional PTV (right) using a search region of 1.75 µm for both cases.

I map the irregularly spaced velocity data to a uniform grid to compare to the simulated flow field. The data is collected into 3D bins and the velocities in these bins are averaged (time average). Next, I perform universal outlier detection (UOD) on the gridded data using a threshold of 2 (Duncan et al. 2010; Westerweel and Scarano 2005). UOD removes 3.08% of the vectors at a volume

fraction of 0.004. For classical PTV, UOD removes 5.8% of outliers. Figure 42 shows 3D vector representations of the experimental and computational data at a time-averaged spatial resolution of 3 x 3 x 3 μm. The time-averaged spatial resolution of this plot could be reduced further but this value shows the velocity values clearly and is small enough to resolve the flow. Some outliers appear to exist even after the UOD algorithm is performed. These are likely at the edges of the domain where UOD is not applicable. The arrow color indicates the value of the out of plane velocity as shown by the colorbar. Red indicates high positive out of plane velocity, blue indicates high negative out of plane velocity, and green indicates small out of plane velocity. Figure 42 shows that the 3D3C velocity fields for the simulated and experimental flow field are qualitatively similar, have a structure one would expect from this geometry, and quantitatively match in the magnitude of velocity. Figure 43 shows the time averaged velocity fields from both top and side views. The computational and experimental results compare well in magnitude and profile. The top views show the plane at z = 13 μm, and the side views show the plane at y = 40 μm. The experimental data and simulated data can further be compared using line plots. Figure 44 shows line plots of experimental data versus simulated data. The line plots are acquired in the same manner as in Figure 44. The blue circles show the median of each bin after binning the non-gridded data, the error bars show one standard deviation, and the red lines show the simulated data. The median of the binned data better ignores the outliers in the data set and so the median is plotted in the line plots presented here. To the right of each of the line plots is a schematic of the location of the

line. Figure 44a shows the comparison between the simulation and the experimental data for out of plane velocity vs. streamwise direction (w vs. x) at y = 60 µm and z = 6 µm. Figure 44a demonstrates that the depth scanning confocal system can accurately measure the out of plane component of velocity in a 3D3C flow through a depthwise expanding microchannel at 30 Hz.

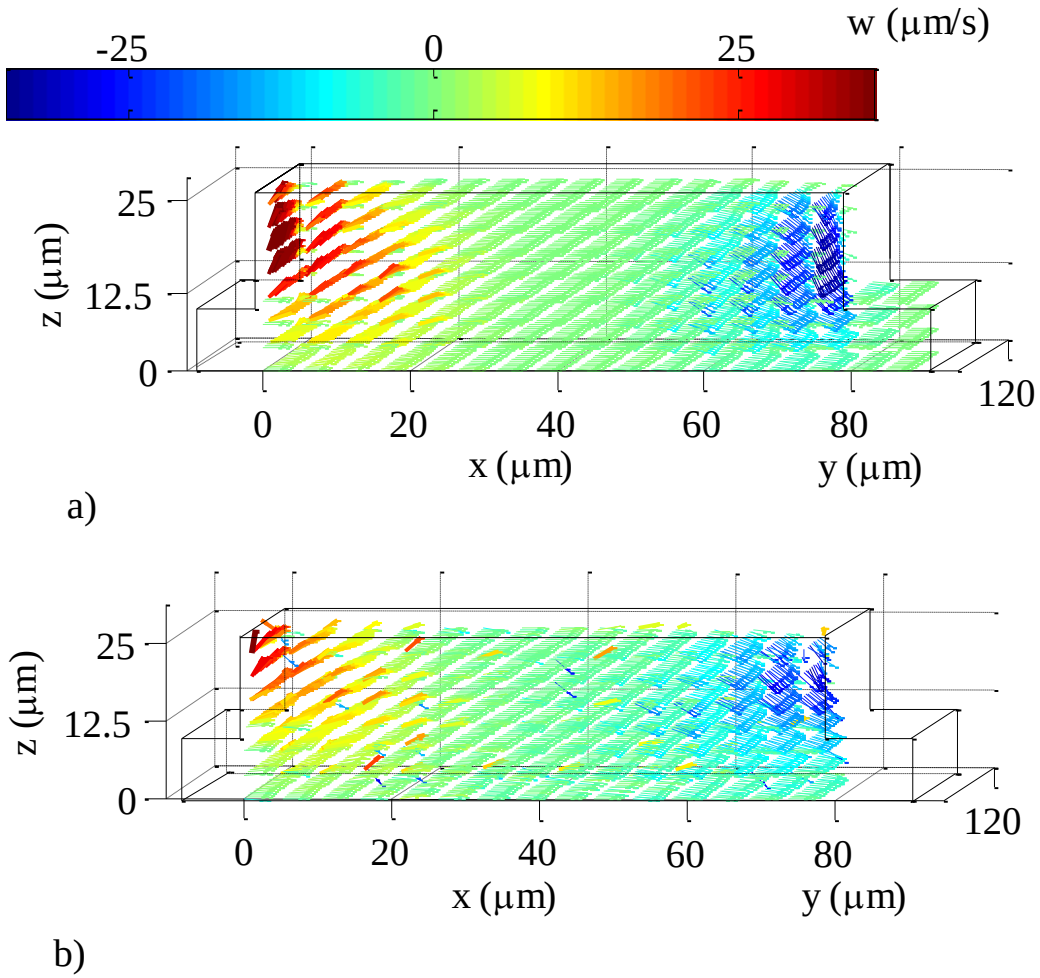

Figure 42. 3D3C vector plots for expanding T channel comparing (a) Simulation solution, and (b) super resolution experimental data. Red indicates positive w velocity and blue indicates negative w velocity. Vector spacing is set to 3 µm by 3µm by 3 µm.

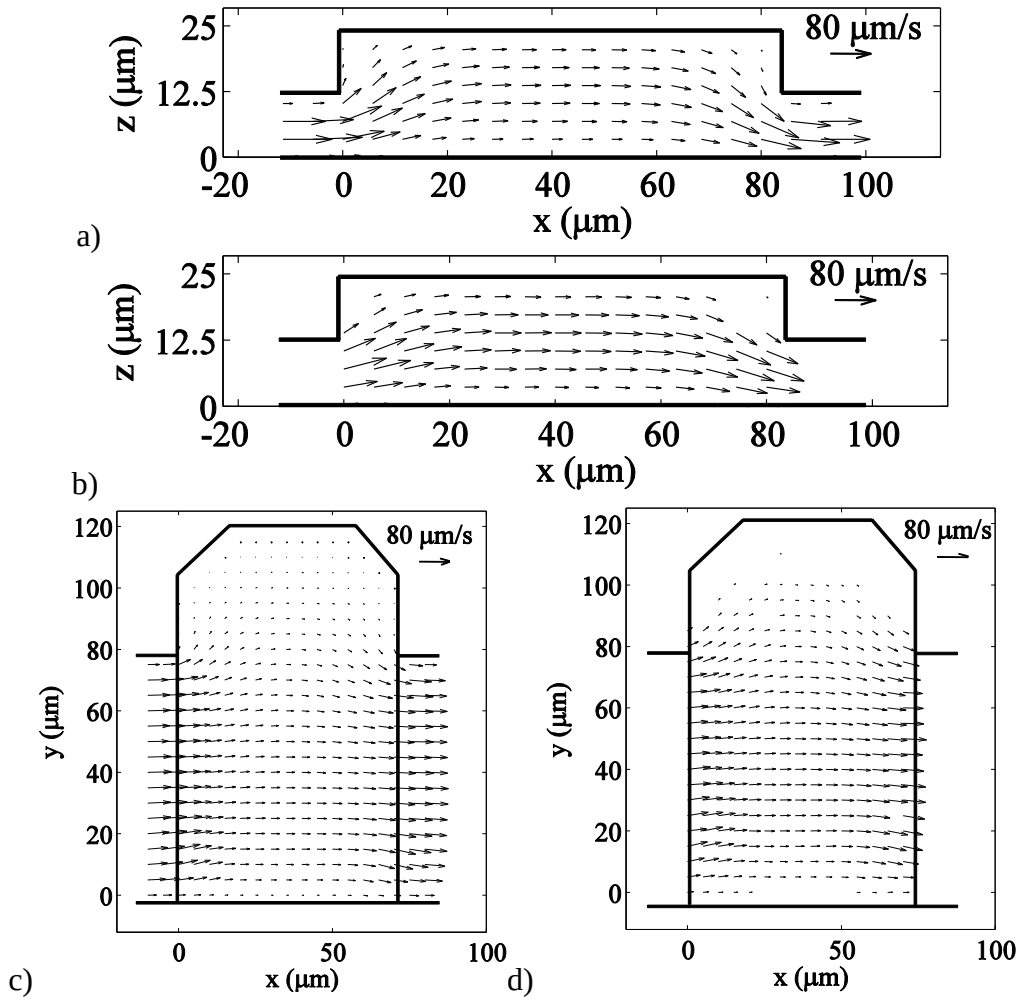

Figure 43. a) Time averaged velocity fields for 3D3C flow. a) Computational side view and b) experimental side view, as well as c) computational top view and d) experimental top view, show good agreement.

The streamwise velocity (u) vs. the spanwise coordinate (y) is plotted at x = 40 and z = 12 μm in Figure 44b. The velocity has a skewed parabolic profile. Figure 44c-e shows the development of the streamwise (u) velocity versus the out of plane (z) coordinate as the flow enters the expansion. Schematics of the line plot locations for all three appear in Figure 44i-k. Figure 44c shows the velocity profile at a location just after the expansion entrance (x = 5 μm) and in the center of the channel in the spanwise direction (y = 60 μm). The velocity is small in the

streamwise direction in the upper part of the channel because viscous forces have not yet developed the flow. Figure 44d shows the flow continuing to develop as it moves into the expansion (x = 11 μm) and Figure 44e shows the fully developed flow at the center of the expansion (x = 40 μm). Figure 44f depicts the spanwise velocity (v) vs. streamwise (x) coordinate in at y = 45 μm and z = 12.5 μm. Along this line, the spanwise velocity first expands into the T expansion and then converges back into the channel. The simulation and experimental data compare well.

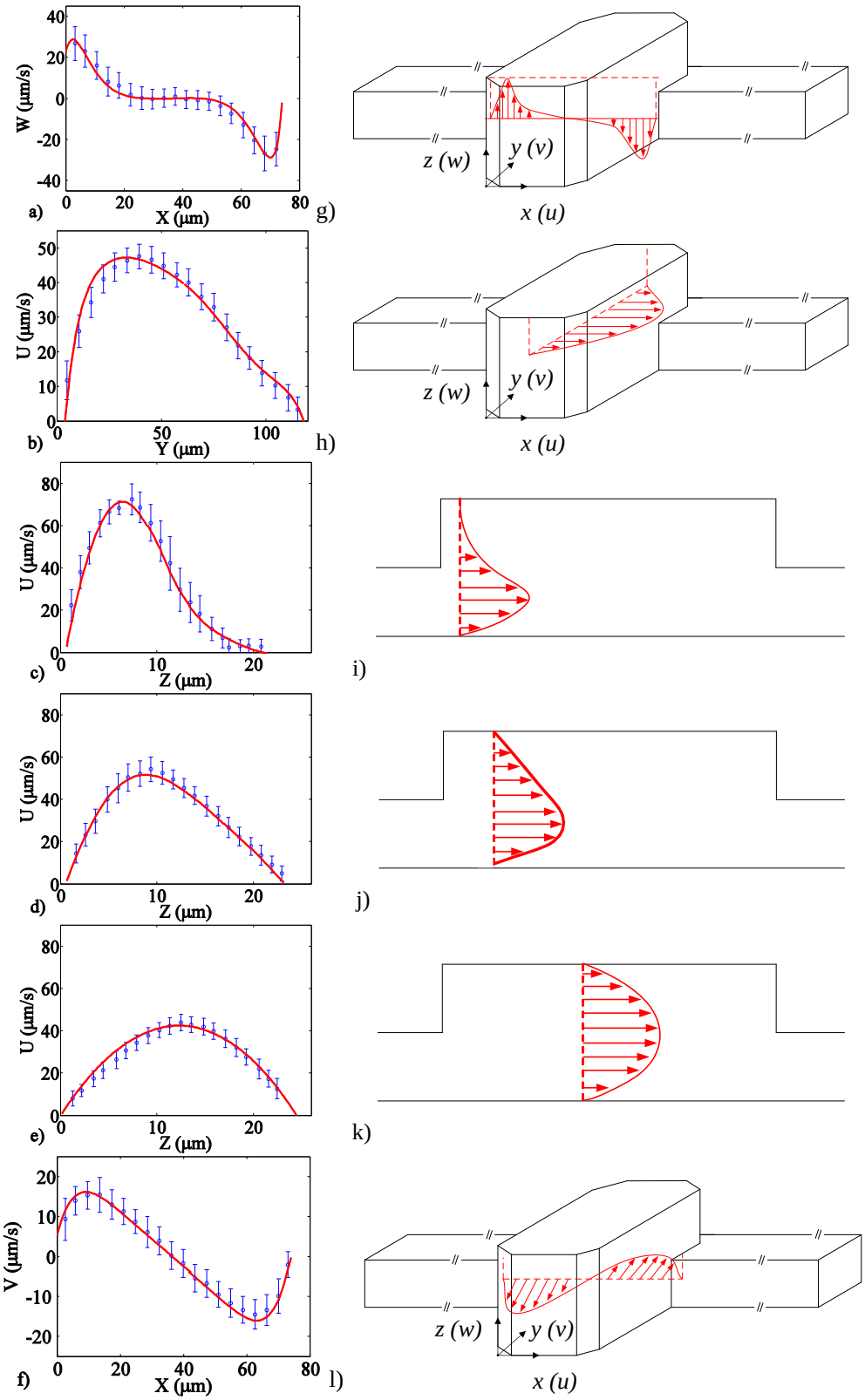

Figure 44. (a-f) Super resolution median velocity (blue circles) and simulated velocity (red squares). (g-l) The relative positions in the microchannel of each of the line plots on the left is shown in the right column.

A simple uncertainty analysis is conducted to compare the error bars in these plots to the expected experimental uncertainty. Uncertainty in PIV and PTV is an ongoing research area, and the following analysis is not complete. For more information on advanced PIV uncertainty analysis, see work by Adrian and others at a recent workshop on uncertainty in PIV (Adrian 2011). Sources of uncertainty in these line plots include Brownian motion of the spheres, $1/10^{th}$ of a pixel uncertainty in correlation peak finding and particle centroid identification, and mistracked particles. The simulation flow rate is based on a one-point calibration to the experimental data as explained in section 5.3. A glass microsyringe is used with hard tubing to reduce capacitance in the system and prevent mismatch between the actual flow rate and set flow rate, but found that the mismatch was still too high. Using a microfluidic flow meter or other flow measurement system would be another way to match the flow rate to the simulation.

Following the analysis of Santiago et al., the percentage of the particle displacement that is due to Brownian motion (Santiago et al. 1998) is estimated as about 11% for flow regions of 50 μm/s. Equation 25a,b below show the equations for estimating the Brownian velocity, where D_{Br} is the diffusivity of the particles, k is Boltzmann's constant, T is the temperature in Kelvin, and μ is the viscosity of water at room temperature.

$$U_{Br} = \sqrt{\frac{2D_{Br}}{\Delta t_{stack}}} \tag{25a}$$

$$D_{Br} = \frac{kT}{6\pi\mu d} \tag{25b}$$

Brownian motion velocities for 1 μm particles should be on the order of 5.3 μm/s. The uncertainty in the camera frame rate and exposure time 20 ns, the PDG is accurate to 5 ns, and the FG has 6 ns jitter. As stated above, centroid identification has an uncertainty of about C_τ = 0.114 μm. Uncertainty propagation analysis can predict the uncertainty in the technique and the total uncertainty including Brownian motion. Again, this analysis is simplified and does not take into account many possible sources of uncertainty, such as invalid vectors, magnification uncertainty, uncertainty from noise in the correlation plane, particle lag, acceleration jerk (Adrian 2011). Equations 26a,b below show the uncertainty analysis.

$$U = \frac{\Delta x}{\Delta t} \tag{26a}$$

$$E_U = \sqrt{\frac{\delta U}{\delta x}^2 {E_x}^2 + \frac{\delta U}{\delta t}^2 {E_t}^2} \tag{26b}$$

where E_t is the uncertainty from the timing equipment (~20 ns), E_x is the error in determining the centroid of the particles (0.114 μm from synthetic image analysis), $\delta U / \delta x = 1 / \Delta t_{stack} = f_{stack}$ = 30 Hz, and $\delta U / \delta t = -\Delta x_{mean} / \Delta t_{stack}^2$ = 1102 μm / s^2 . Using these values, E_U = 3.4 μm / s. Then the following equation determines the uncertainty due to Brownian motion and the method,

$$E_t = \sqrt{{E_U}^2 + {E_{Br}}^2} \tag{27}$$

From uncertainty propagation analysis, the uncertainty due to the method and Brownian motion is 6.4 μm/s. This value roughly corresponds with the error bars in Figure 44. The largest component of the error in this analysis is due to

Brownian motion, which is not related to the technique but rather to the physics of small-scale fluid motion at low Peclet numbers. Increasing the particle diameter to 2 μm would reduce the total uncertainty to 5.1 μm/s. The uncertainty in the technique independent of Brownian motion is on the order 3.4 μm/s or 6.8% of the mean *u* velocity.

The dynamic spatial range (DSR) for PIV is defined as the ratio of the field of view and the smallest resolvable spatial variation. A related quantity, the dynamic velocity range (DVR) is defined as the ratio of the maximum velocity that can be measured divided by the minimum resolvable velocity measurement (Adrian 1997). For 3D systems, Ooms et al. developed equations for DSR_{xy}, DVR_{xy}, DSR_z, and DVR_z (Ooms, Lindken, and Westerweel 2009). Following the procedure from Ooms et al. and using the parameters from Table 1 with $\varphi = 0.004$, $DSR_{xy} = 83.55$, $DVR_{xy} = 71.5$, $DSR_z = 8.95$ and $DVR_z = 43.44$. These values are for time resolved measurements (not averaged in time). The low DSR_z results from the low aspect ratio of the channel in the *z* dimension. These values represent the DSR and DVR for our specific set of parameters. Increasing the volume fraction has the effect of increasing DSR and reducing DVR as shown in the equations of Ooms et al.. Additionally, this analysis assumes classic PTV as a conservative estimate, and does not take into account improvements in maximum particle displacement due to the super resolution algorithm.

5.7. Summary

This chapter has demonstrated that the confocal volumetric scanning method can accurately measure temporally resolved 3D3C velocity fields at the microscale. The system can measure velocities at up to 60 Hz using super resolution PIV and a piezo objective positioner, with sufficient illumination and confocal disk speed. The equations that estimate the limits of parameters of the system show U_{max} can be increased by increasing the average piezo speed, $U_{piezo,avg}$, or decreasing the scanned depth, D. $U_{piezo,avg}$ is limited in these experiments by the confocal disk speed, and using a faster disk or no confocal disk would allow scan rates of up to 60 Hz for the 26 µm deep channel used in this work. Using a channel with a smaller depth would also allow higher 3D scan rates. In general, to prevent smearing of the particle images in the direction of motion, the Δt_{slice} should be less than the slice spacing divided by $C_\theta U_{max}$, where C_θ is the tangent of the angle of acceptable smearing. However, this constraint is not limiting in the current system.

Super resolution PIV increases the spatial resolution of the velocity data compared with classical PIV. Using super resolution PIV, the system improves the range of measurable velocities and reduces the number of outliers compared to classical PTV with the same search radius as shown in Figure 41. A motion correction algorithm partially corrects tracer particle positions for their displacement during the finite time it takes to scan the depth. The confocal improves correlation S/N as shown in my previous work (Klein and Posner 2010) and reduces smearing of the point spread function in the depthwise direction

(Kino and Corle 1989), however it also limits acquisition speed and reduces the illumination intensity. In preliminary experiments, it was determined that the technique functions without the confocal disk and allowed for faster camera speeds (reduction in Δt_{slice}). However, unless the particle volume fractions was kept low (lowering spatial resolution), out of focus light increased the error due to mistracked particles. A detailed comparison of the technique between confocal and widefield systems is beyond the scope of this work. Future work in this area may include comparing confocal to widefield systems for volumetric particle velocimetry measurements.

This method allows direct measurement of the time resolved three-dimensional motion of tracer particles in a microscale volume at 30 Hz and 4.5 μm by 4.5 μm by 4.5 μm spatial resolution. The experimental data collected using the 3D3C confocal volumetric scanning system matches well with the COMSOL simulation. Compared to other methods, this technique has a higher instantaneous spatial resolution (4.5 μm) than other temporally resolved 3D methods that I have seen reported. However, time resolved 3D methods that collect data from 2D projected images and infer the 3rd component of velocity using a stereo, holographic, or defocusing type imaging system can achieve superior temporal resolution at the expense of spatial resolution. Three dimensional data acquisition rates of thousands of frames per second are possible using these methods, with spatial resolutions in the range of 20 to several hundred microns. Stereoscopic techniques cannot temporally resolve 3D flow fields

unless the depth of the microchannel is smaller than the overlapped depth of field of the two objectives, or the depth is scanned.

The scanning of the flow field reduces the maximum measurable velocity of this technique compared to methods using projected images, however, no calibration or reconstruction algorithms are required for this technique. In addition, the technique directly estimates the out of plane velocity from 3D images of the actual particle displacements rather than inferring it from 2D projected images and is compatible with high numerical aperture objectives allowing high spatial resolution. Future work in this area includes applications to temporally resolved 3D3C flows at the microscale.

In the next section, quantitative fluorescence measurements of the structure of 3D isotachophoresis plugs are presented. A high-speed 3D system is required to visualize 3D structure of the plugs because they advect quickly through the microchannel.

CHAPTER 6

3D CONFOCAL IMAGING OF ISOTACHOPHORESIS PLUGS

6.1. Introduction

Isotachophoresis (ITP) is a technique, similar to electrophoresis, used to separate charged species or concentrate a single analyte. The method applies a discontinuous electric field to the sample (here a microchannel) that contains species with varying electrical mobility. The sample to be concentrated and/or separated is introduced between a high mobility leading electrolyte (LE) and low mobility trailing electrolyte (TE), where the mobility, μ, of the electrolyte is the velocity per unit of applied electric field. The analytes to be separated and/or concentrated must have a mobility between that of the terminating and leading electrolytes. A schematic of the ITP process after the application of the electric field is shown in Figure 45.

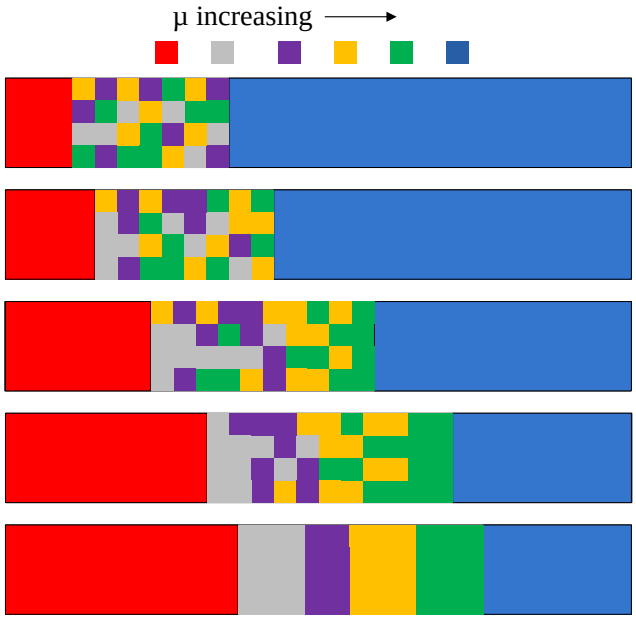

Figure 45. Schematic of ITP process. Blue: leading electrolyte; Red: terminating electrolyte; hatched: the analytes.

The shape of ITP plugs is an area of interest for researchers but it is difficult to investigate their shape in the out of plane dimension because they advect quickly through the microchannel. A 2D view of a ITP plug viewed in a typical epilflourescence microscope is shown in Figure 46. In this chapter, a brief demonstration of an application for the high-speed 3D scanning confocal system by investigating the 3D structure of fluorescent ITP zones is presented. The computational modeling presented in this section was performed in collaboration with Giancarlo Garcia, Moran Bervovici, and Prof. Juan Santiago at Stanford.

Figure 46. ITP plug advecting through microchannel.

6.2. Experimental Method

A detailed depiction of the experimental setup used here is given in section 3 and section 3.9. The equipment used here is the same, replacing the Lab Smith high voltage DC amplifier with a Keithley 1100 V source meter.

A simple cylindrical glass capillary with a 40 μm diameter and 5 cm length serves as the microchannel for the ITP experiments. Glass wells are used to interface to the microchannel. Care is taken to add even amounts of fluid to both wells to suppress flow due to a pressure gradient. A schematic of the microchannel setup is shown in Figure 47.

The TE buffer is HCl at 100mM concentration and the LE buffer is 50 mM MES buffer. A single analyte is used, fluorescent dye with excitation spectra near 532 nm (AF532, Invitrogen, USA) conjugated with DNA. The DNA provides the correct mobility to allow focusing of the sample between the leading and trailing electrolytes. Three dimensional image stacks are acquired at frequency of 10 Hz and individual slices are acquired at 1000 Hz with 25 slices per scan and 1.6 μm between individual slices. The system needs to acquire 3D stacks at ≥ 10 Hz to ensure that it captures at least one stack of the fluorescent plug as it travels through the field of view. Setting the number of frames per scan at 25 gives us enough frames to visualize the entire plug and the interslice distance of 1.6 um is less than the approximate optical sectioning thickness for this system, as discussed in Chapters 3 and 5 (Wilhelm et al. 2003).

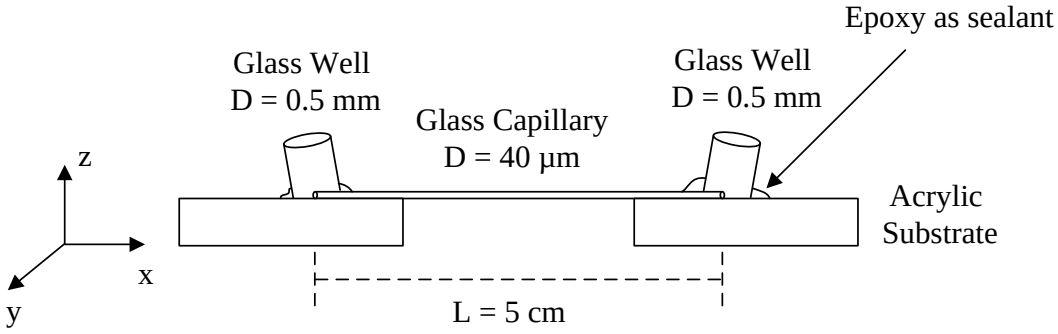

Figure 47. Experimental apparatus for ITP experiments.

6.3. Results

Plugs are captured in 3D and compared to results from a computational physics model provided by our collaborators at Stanford University. The model calculates the dye concentration at various locations along the microchannel,

using input parameters from the experiment (electric field, diameter of capillary, mobility of electrolytes, position along length of channel, etc). Figure 48 shows the experimental and predicted plug profiles for an ITP plug captured at an *x* location of L/L_{max} = 0.25, where L_{max} is the total microchannel length of 5 cm, with flow from left to right. Figure 48a and b show experimental data and Figure 48c and d depict the simulation results. Figure 48a and c show the plug shape in the *x*-*y* plane at a *z* location of *z*/*h* = 0.5. Figure 48b and d show the cross section of the plug in *y*-*z* plane at an *x* location indicated by the dotted line.

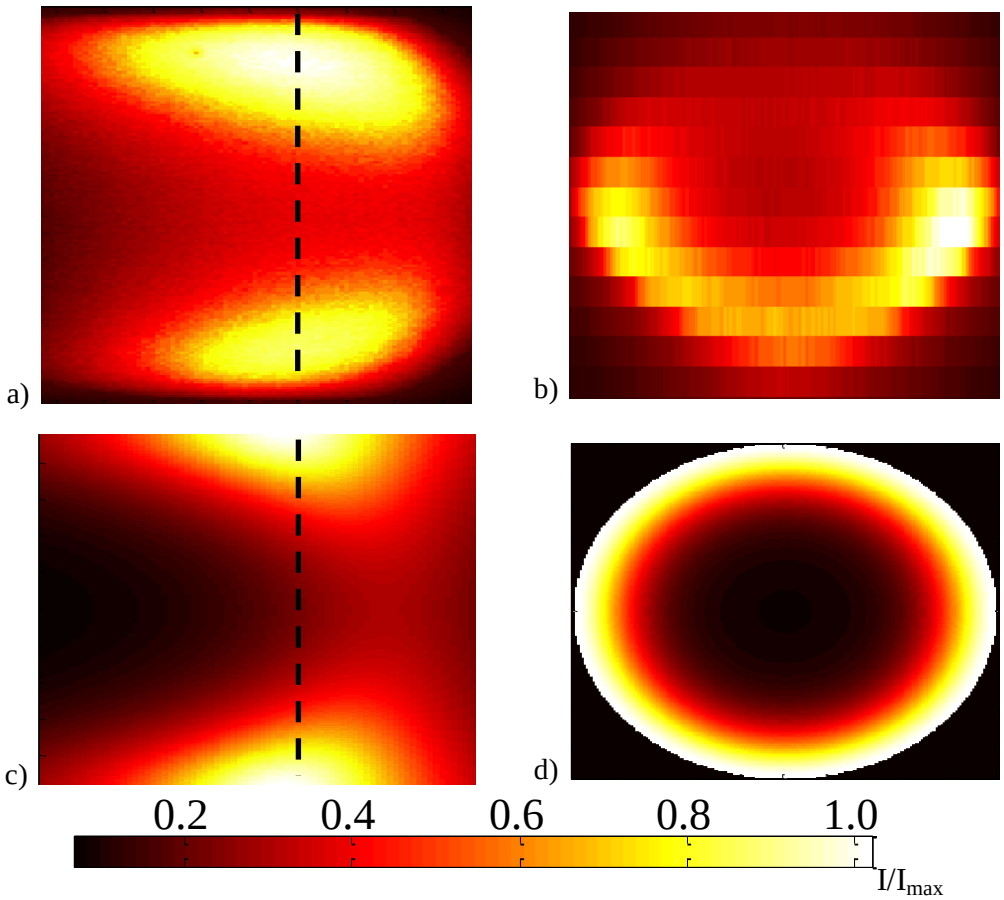

Figure 48. Isotachophoresis plugs with (a) and (b) showing experimental data and (c) and (d) depicting the simulation results. Figures (a) and (c) show the plug shape in the *x*-*y* plane at a *z* location of *z*/*h* = 0.5. Figures (b) and (d) show the cross section of the plug in *y*-*z* plane at a *x* location indicated by the dotted line.

The analytical model predicts that the plug shape in the *x*-*y* plane will be convex before $L = 0.5$ and concave after $L = 0.5$. From Figure 48and c, the experiments and model match in this respect. However, the north side of the experimental data seems to have a higher concentration of dye than the south side. The cause of this asymmetry is unknown, but it may be due to an instability in the ITP plug. Figure 48b and d show that the *yz* cross section of the plugs in both the simulations and experiments are toroid-shaped with the dye concentrating around the walls of the capillary. Interestingly, there is an apparent asymmetry in the experiment with a higher concentration of the dye in the lower section of the channel than the upper section as seen in Figure 48b. This is a repeatable phenomenon that has been observed in multiple experiments. Experiments have been conducted using varying concentrations of Rhodamine B dye in the microchannel that indicate that this discrepancy is due to the dye absorbing the excitation laser light at high dye concentrations, such that the excitation light becomes dimmer at the deeper focal planes. Cross sections in the *y*-*z* plane of Rhodamine dye at 1mM and 10mM concentrations are shown in Figure 49.

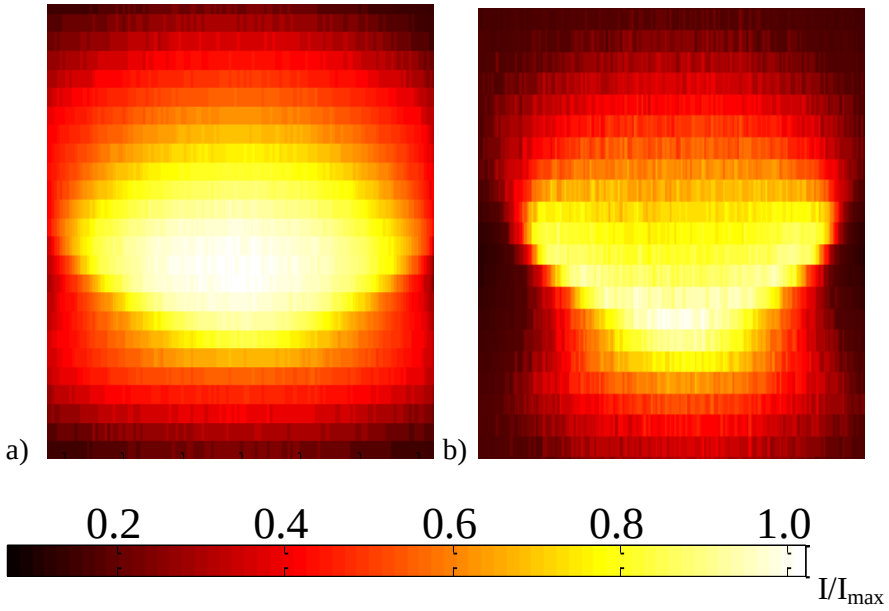

Figure 49. *xz* cross sections of a 40 µm capillary filled with Rhodamine dye at concentrations of 1 mM (a) and 10 mM (b). At 10 mM it is clear that absorption of the laser light by the dye causes the upper portion of the plug to appear less bright than the lower portion.

It is clear that at a concentration of 10mM the dye is apparently brighter in the lower portion of the channel compared to the upper portion, however this does not appear to be happening at 1mM concentrations. My assertion is that this effect is due to absorption of the laser light by the dye at higher concentrations where it becomes opaque. Assuming that the same effect is happening in the ITP experiments, it can be corrected for by conducting a pointwise division of Figure 48b by Figure 49b. The result of this operation is depicted in Figure 50a.

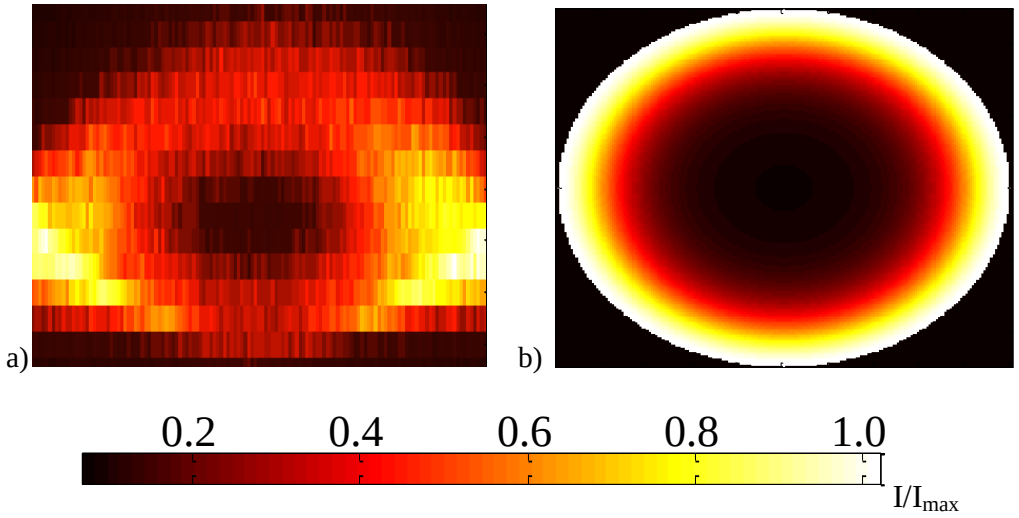

Figure 50. (a) *x*Z cross section of an ITP plug normalized by the 10mM *x*Z cross section shown in Figure 49b.

Figure 50 shows that after the experimental *y*-*z* cross section of the ITP plug is normalized by the *y*-*z* cross section of the Rhodamine filled channel, it more closely matches the simulated *y*-*z* cross section. Some asymmetry still exists, but most of the north-south asymmetry is removed and the overall shape of the plug is more toroidal than it was without normalization.

The simulation does not take into account any optical effects. This means that the experimental images will necessarily appear more smeared out due to the finite aperture of the microscope lens and its point spread function (see Chapter 2).

6.4. Summary

This data shows that the volumetric confocal scanning system is capable of capturing the 3D shape of ITP plugs as they advect through the microchannel. The convex shape of the plug is expected, however deviations from the prediction

of the numerical model are observed in both the planar and axial dimensions. Absorbance of the excitation light by the dye at high concentration is likely the culprit in the out of plane asymmetry observed. However, the in-plane asymmetry is not yet resolved, though it may be due to instabilities that are known to occur in ITP plugs under certain conditions. Further study is needed, but high speed volumetric scanning confocal measurements have been shown to be a useful tool in these types of investigations. Future work includes integrating the smearing effect due to the PSF of the optics into the model, which will enhance the comparison, as well as a detailed investigation of the asymmetries observed in the 3D ITP plugs at various experimental conditions.

CHAPTER 7

DIFFUSIOPHORETIC MOTION OF COLLOIDS ASSEMBLING ON A COPPER SUBSTRATE

7.1. Motivation

Colloidal crystal formations are important for a variety of applications from the deposition of paint onto surfaces to ultrafast protein identification assays. Defects formed in these films impair their effectiveness and should be investigated. In this chapter, the 3D confocal system described in this work is utilized to track colloidal particles during colloidal crystal deposition. Colloidal crystal films can be deposited on a substrate using a variety of methods. Some methods to create colloidal crystals include evaporation, electrodeposition, or diffusiophoresis. This chapter investigates diffusiophoretic deposition of colloidal crystals. Diffusiophoresis is a technique in which species translocate from one area to another due to a concentration gradient which induces an electric field (Prieve, Gerhart, and Smith 1978). Diffusiophoresis is used as the method of colloid deposition because the particle displacements are slow enough to measure easily in 3D while the flow remains unsteady and typically has three components of velocity. Additionally, diffusiophoresis is a current area of interest for colleagues in my laboratory. Confocal systems have been utilized previously to study the diffusion of colloids in colloidal crystal films but most systems are not fast enough to measure the actual deposition process in 3 dimensions (Dinsmore et al. 2001; Weeks et al. 2000; Besseling et al. 2009). The work in this section was performed in collaboration with Carlos Perez at ASU.

7.2. Introduction

The procedure to create a diffusiophoretic flow in this work uses hydrogen peroxide, a sacrificial copper substrate, sulphuric acid, and 3 μm fluorescent polystyrene particles as shown in Figure 51. The hydrogen peroxide causes the copper to dissociate from the substrate creating Cu^{2+} and OH^- ions. The sulfuric acid prevents oxidation of the surface copper by breaking down copper oxides that accumulate on the surface due to the hydrogen peroxide. The OH^- groups have a higher diffusivity than the copper ions and therefore diffuse away from the substrate faster. This causes a charge difference near the substrate due to a concentration gradient in positive and negative ions. This charge difference induces a diffusion potential which creates an electric field. The electric field scales as shown in equation 28 below, where D_1 is the diffusivity of the higher diffusivity ion (Prieve, Gerhart, and Smith 1978).

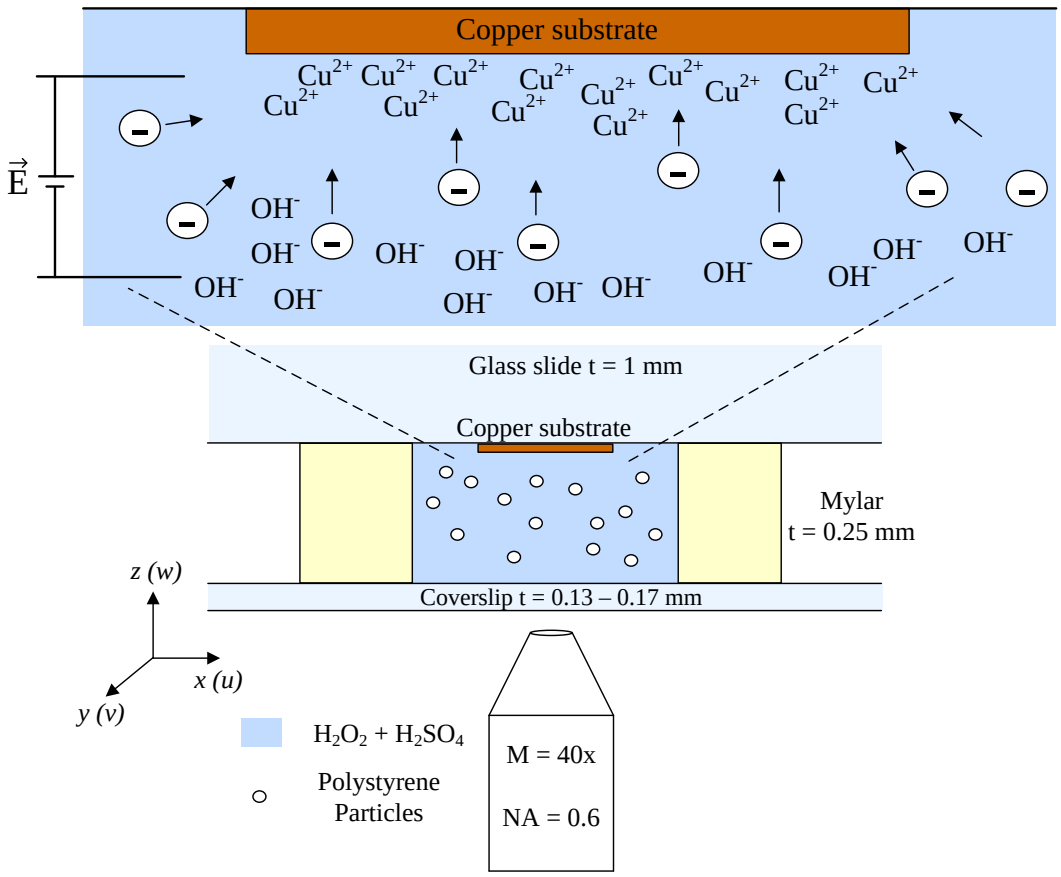

Figure 51. Depiction of diffusiophoretic deposition of colloids onto a substrate. Hydrogen peroxide causes the disassociation of Cu^{2+} and OH^- ions from the copper sacrificial substrate. The higher diffusivity of the OH^- groups causes them to migrate away from the surface faster than the heavy metals (Cu^{2+}), causing a ion concentration gradient (more positive than negative ions near the surface of the sacrificial substrate). This concentration gradient induces an electric field which causes the migration of the particles towards the substrate.

$$E \propto \frac{D_1 - D_2}{D_1 + D_2} \qquad (25)$$

The electric field causes the migration of the negatively charged polystyrene particles to the substrate. The electric field causes the particles to be attracted to the positively charged surface of the copper, where they should adhere due to Van Der Walls forces. Since the adhered particles are still negatively charged, the particles in solution should preferentially adhere to locations on the copper

surface that are void of polystyrene particles. The idea being that a colloidal crystal monolayer will be constructed of polystyrene particles with few defects. The method should also allow patterning of colloidal crystal films by changing the shape of the copper substrate.

7.3. Experimental Setup

As shown in Figure 51, the volumetric confocal scanning system measures particle motion in three dimensions. For a complete description of the measurement system, please see Chapter 3. In this experiment, I am interested in tracking the displacement of the particles individually, so only the PTV algorithm is used instead of the super resolution PIV algorithm. The solvent for this experiment is distilled water. The volume fraction of particles (φ), particle diameter (d), weight fraction of hydrogen peroxide (W_{H2O2}), and weight fraction of sulfuric acid (W_{H2SO4}) are shown 0.01%, 3 μm, 0.24%, and 0.24% respectively. The displacements of the particles are slow enough that the system uses Δt_{stack} = 200 ms, and use Δt_{slice} = 2 ms. The field of view is oriented such that the experiment measures particle displacements near the northeast corner of the copper substrate, with the top of the scanned depth coinciding with the top of the substrate. The number of slices per stack and number of stacks per experiment are 25 slices, and 640 stacks, respectively. The scanned depth, D, is 55 μm so the slice spacing, P_z, is 2.2 μm. This is less than the FWHM of the system with a 40x objective, 3.85 μm. The experimental parameters are listed in Table 7.

Table 7. Parameters for diffusiophoresis experiment

φ (%)	d (μm)	W_{H2O2} (%)	W_{H2SO4} (%)	Δt_{stack} (ms)	Δt_{slice} (ms)	D (μm)
0.01	3	0.24	0.24	200	2	55

7.4. Results

The method measures the temporally resolved 3D3C displacement of the polystyrene spheres as they are attracted to the copper substrate. Figure 52 shows isosurfaces of particle image intensity superimposed with temporally resolved particle tracks. The copper substrate is located in the lower left hand corner of Figure 52a and the upper left hand corner of Figure 52b.

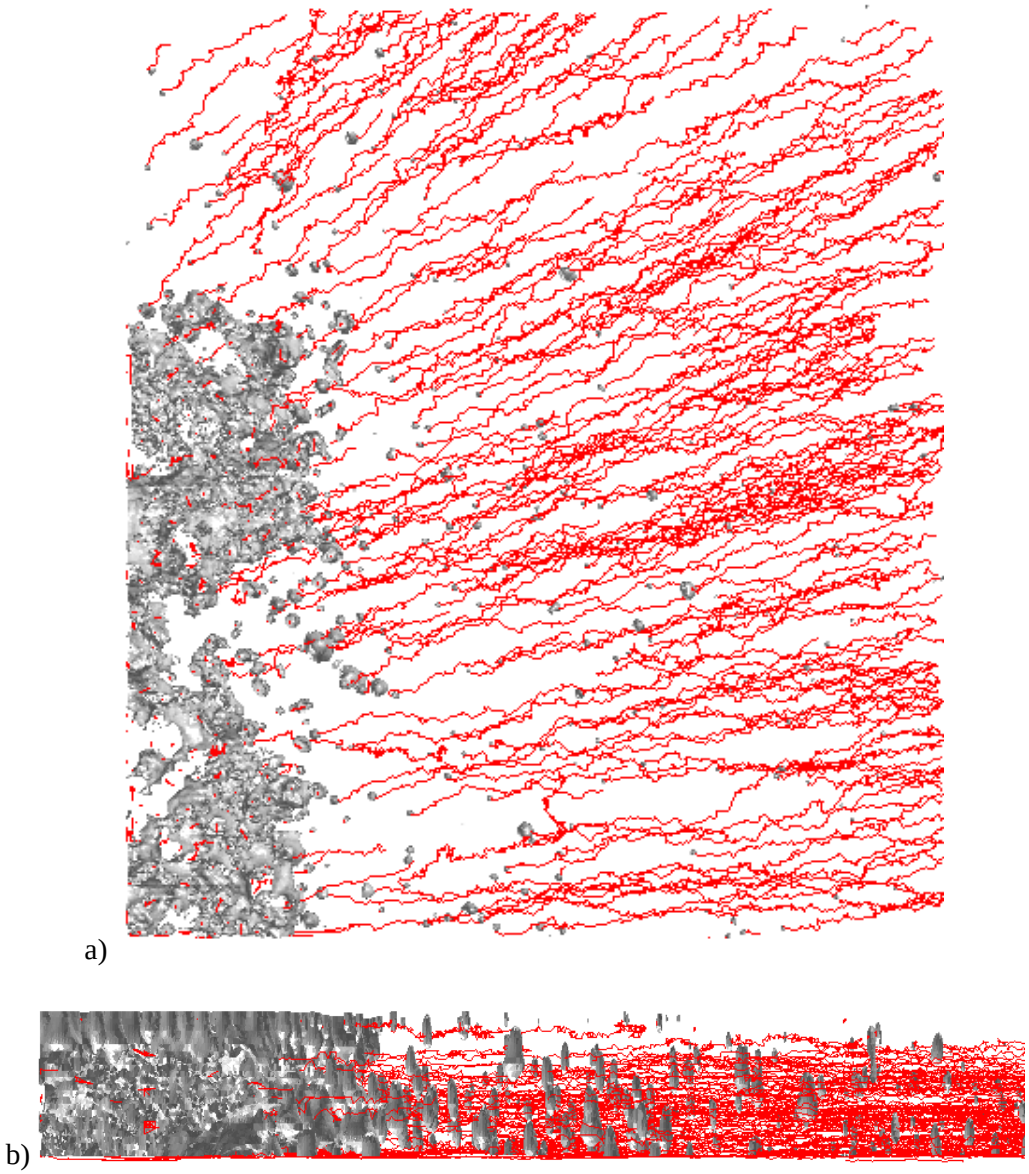

Figure 52. (a) Top view of particle motion towards the copper substrate. (b) Side view of particle motion. The copper substrate is located in the lower left hand corner of (a) and the upper left hand corner of (b).

It is clear from Figure 52 that there is net particle motion towards the copper substrate in both the *x* and *y* directions (coordinates from Figure 51) as expected from theory. However, whether or not there is net particle motion in the *z* direction is less clear. To investigate this further the data is averaged in time and gridded 3D vector plots and histograms are created. Figure 53 shows velocity

data for the three spatial dimensions. Figure 53a shows the *u* velocity has a Gaussian shaped velocity histogram with a negative mean, with many 'outlier' velocities very close to 0. Figure 53b shows a similar behavior with the mean of the Gaussian slightly less negative in this case. Figure 53c shows a histogram with a distribution showing three peaks, one at 0, one slightly positive and one slightly negative. From experience with this type of data, the two secondary peaks in Figure 53c are caused by pixel locking. This is likely because the slice spacing was not close enough in the *z* direction. Without the pixel locking effects the profile in Figure 53c would likely be Gaussian and centered around 0.

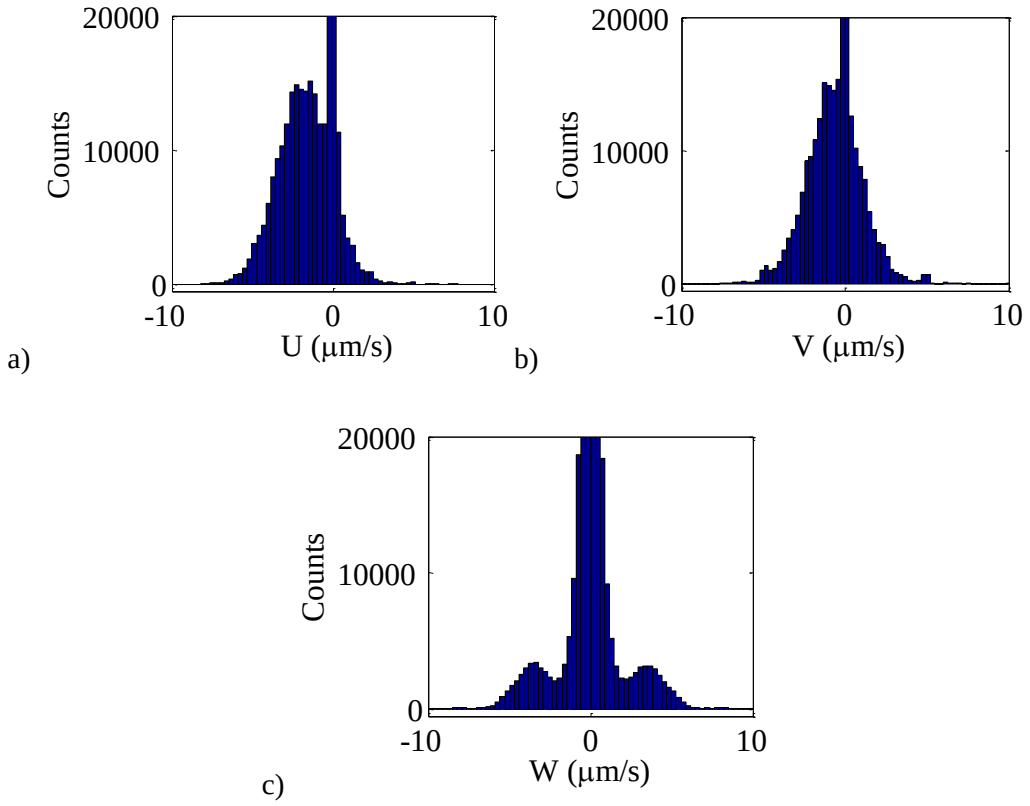

Figure 53. Histograms of particle velocity data. (a) *u* velocity (b) *v* velocity (c) *w* velocity.

The mean velocities from the time averaged data in each dimension are: u_{mean} = -1.00 μm/s, v_{mean} = -0.38 μm/s, w_{mean} = -0.01 μm/s. The peak in the number of velocities near 0 is likely due to particles that are adhered to the substrate surface but are still tracked. To remove these static particles from the statistics, the histograms can be used to estimate which particles to remove. From the histograms, the range of velocities between 0.2 and -0.4 μm/s for the *u* velocities are ignored from the statistics. For the *v* and *w* velocities, ranges of 0.2 and -0.3 μm/s and 0.2 and -0.2 μm/s respectively are ignored. Recomputing the mean velocities, u_{mean} = 1.89 μm/s, v_{mean} = -0.74 μm/s, w_{mean} = -0.01 μm/s. So

using this procedure to remove the static particles, the mean velocities in the *u* and *v* directions nearly doubled, whereas the *w* velocity stayed roughly the same.

Another method visualizes the data as 3D vector plots. A bin spacing of 15 by 15 by 15 μm is chosen, and all of the velocity values in each bin are averaged in time. Figure 54 shows 3D vector plots of velocity for a bin size of 15 by 15 by 15 μm. Figure 54a shows an isometric view of the velocity field and Figure 54b shows a side view.

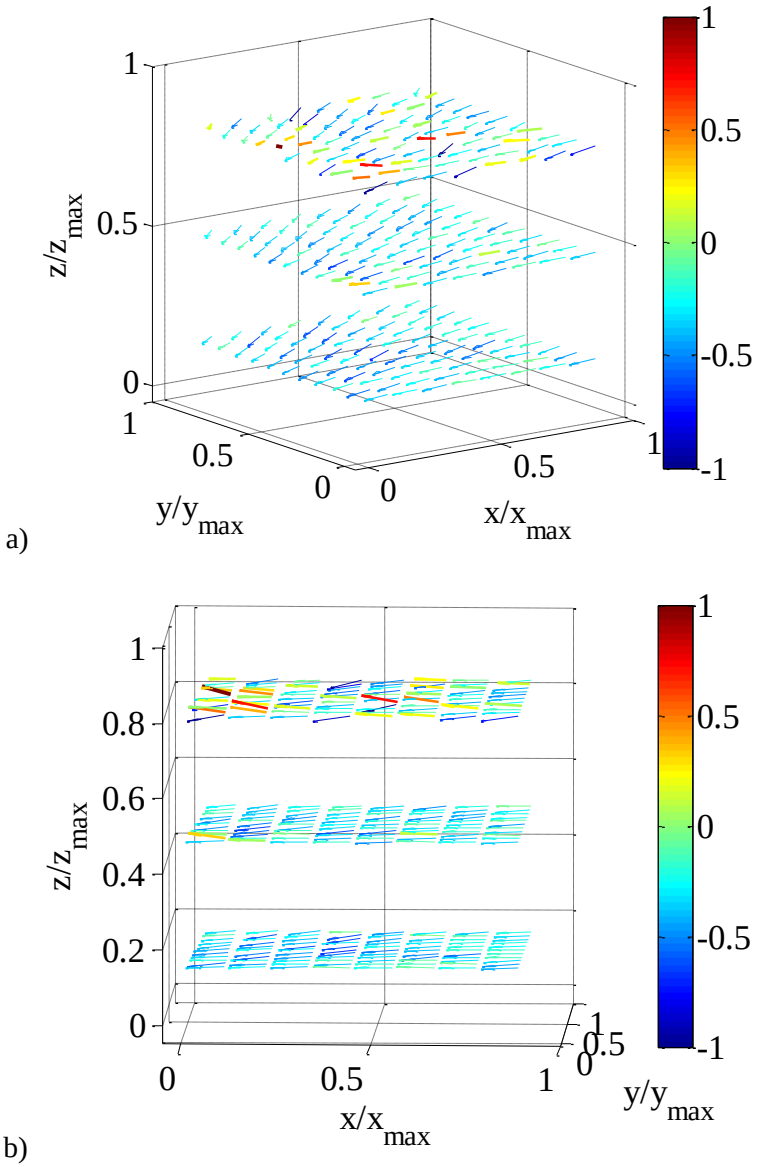

Figure 54. 3D velocity vectors for diffusiophoretic flow.

Figure 54 shows that, as expected from the previous visualizations, there seems to be very little out of plane motion of the particles, whereas there is clear *x* and *y* direction velocities. From theory, there should be a positive *z* velocity at planes below the copper substrate. In order to obtain a clearer picture of the velocity field, the velocity is averaged in the *z* direction, since there is apparently very little velocity in that direction. Figure 55 shows the velocity field after *z*

dimension averaging. Most outliers are removed and a seemingly robust estimate of the *u* and *v* velocities remains. The black rectangle in Figure 55 represents the copper substrate. Velocities appear to diminish at locations very close to the substrate surface. The center of the copper substrate in the *y* direction is located at $y \sim 0$. Interestingly, the velocities seem to be directed towards the center of the substrate, as they level out ($v \sim 0$) at $y \sim 0$.

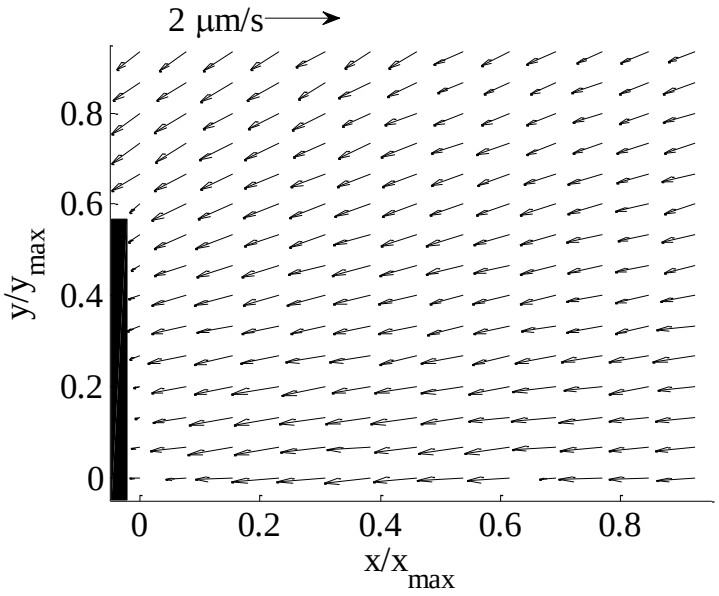

Figure 55. 2D velocity vector field (averaged in *z* direction).

7.5. Summary and future work

This chapter has investigated a possible application for the time resolved 3D3C volumetric scanning particle tracking velocimetry system. Measurements of 3D particle motion were recorded for a diffusiophoretic colloidal crystal deposition process. No significant net *z* direction motion was recorded in this brief experiment. However, pixel locking and the choice of field of view likely

played a role in the absence of out of plane motion. Running the experiment with the field of view directly under the center of the substrate (in x and y) will likely yield results for net out of plane motion. To fix the pixel locking issues, the slice spacing should be reduced in future work. Other future work in this area includes varying the weight fraction of H_2SO_4 and H_2O_2 as well as other parameters such as particle size, particle type, particle volume fraction, orientation of the substrate relative to the microscope, and geometry of the substrate.

CHAPTER 8

CONCLUSIONS

Velocity measurements at the microscale continue to be an area of interest for researchers in a variety of fields. Techniques for improving these velocity measurements are varied in scope and application. I have shown that a confocal system in conjunction with an epifluorescence microscope and high speed camera reduces the number of erroneous vectors in unsteady μPIV measurements through improvements in correlation signal to noise ratio. Using the confocal system, the percent erroneous vectors were reduced by over 5% in some cases, and, except at very low volume fractions (0.05% of 500 nm particles), the confocal system was found to reduce the number of erroneous vectors. The first ever PIV measurements of an electrokinetic instability in a microchannel were recorded using this confocal system at 1250 Hz with a spatial resolution of 4.9 μm by 4.9 μm (published in MS&T in 2010 by my collaborators and I). Recent work improving PIV algorithms also shows promise in enabling two-frame microscale velocity measurements. Future work should include integrating these new algorithms with 3D3C volumetric scanning super resolution PIV.

A 3D3C diagnostic was developed that uses a high speed camera, high speed confocal disk, and a high speed piezo actuated positioner to image unsteady 3D flow volumes at up to 60 Hz (16 ms temporal resolution). Velocity measurements were acquired using a PIV estimator for PTV measurements (super resolution PIV) at 30 Hz (33 ms temporal resolution) with an instantaneous spatial resolution

of 4.5 μm in each dimension. This is an increase (reduction in the magnitude of) in spatial resolution compared to most existing temporally resolved 3D3C measurements techniques for microvolumes. Techniques using projected images can obtain much higher temporal resolution than the current work (under 1 ms possible), at the expense of instantaneous spatial resolution. Maximum measureable velocities for the parameters used here are on the order of 100 μm/s with a field of view of 80 μm by 120 μm by 26 μm, a Reynolds number of Re ~ $8x10^{-4}$, and a Peclet number of Pe ~ 100. Dynamic velocity range (DVR) and dynamic spatial range (DSR) for the *xy* and *z* directions are estimated to be obtain $DSR_{xy} = 83.55$, $DVR_{xy} = 71.5$, $DSR_z = 8.95$ and $DVR_z = 43.44$. Comparison with simulations show the uncertainty between simulations and experiments to be on the order of 6-12%. More research is needed to accurately determine the true uncertainty of the technique because uncertainty in PIV and PTV is a developing area of research. Overall, the 3D3C volumetric scanning technique depicted here reduces the maximum measurable velocity of this technique compared to methods using projected images, however, no calibration or reconstruction algorithms are required for this technique. In addition, the technique directly estimates the out of plane velocity from 3D images of the actual particle displacements rather than inferring it from 2D projected images and is compatible with high numerical aperture objectives allowing high spatial resolution. As such, the diagnostic presented here has its main application in unsteady 3D flows such as colloidal crystal deposition, multi-cell tracking, as well as imaging applications such as the study of isotachophoresis plugs and Turing-patterns.

REFERENCES

Adrian, R. J. 1984. Scattering Particle Characteristics and Their Effect on Pulsed Laser Measurements of Fluid-Flow - Speckle Velocimetry Vs Particle Image Velocimetry. *Applied Optics* 23 (11):1690-1691.

Adrian, R. J. 1991. Particle-Imaging Techniques for Experimental Fluid-Mechanics. *Annual Review of Fluid Mechanics* 23:261-304.

Adrian, R. J. 1997. Dynamic ranges of velocity and spatial resolution of particle image velocimetry. *Measurement Science & Technology* 8 (12):1393-1398.

Adrian, R. J. 2005. Twenty years of particle image velocimetry. *Experiments in Fluids* 39 (2):159-169.

Adrian, R. J. 2011. The elements determining the accuracy of PIV measurements. Paper read at Workshop on Uncertainty in PIV, May 11, 2011, at Las Vegas, NV.

Adrian, R. J., and C. S. Yao. 1985. Pulsed Laser Technique Application to Liquid and Gaseous Flows and the Scattering Power of Seed Materials. *Applied Optics* 24 (1):44-52.

Anderson, J. R., D. T. Chiu, R. J. Jackman, O. Cherniavskaya, J. C. McDonald, H. K. Wu, S. H. Whitesides, and G. M. Whitesides. 2000. Fabrication of topologically complex three-dimensional microfluidic systems in PDMS by rapid prototyping. *Analytical Chemistry* 72 (14):3158-3164.

Angele, K. P., Y. Suzuki, J. Miwa, and N. Kasagi. 2006. Development of a high-speed scanning micro PIV system using a rotating disc. *Measurement Science & Technology* 17 (7):1639-1646.

Bastiaans, R. J. M., G. A. J. van der Plas, and R. N. Kieft. 2002. The performance of a new PTV algorithm applied in super-resolution PIV. *Experiments in Fluids* 32 (3):346-356.

Baygents, J. C., and F. Baldessari. 1998. Electrohydrodynamic instability in a thin fluid layer with an electrical conductivity gradient. *Physics of Fluids* 10 (1):301-311.

Besseling, R., L. Isa, E. R. Weeks, and W. C. K. Poon. 2009. Quantitative imaging of colloidal flows. *Advances in Colloid and Interface Science* 146 (1-2):1-17.

Bolt, P. S., J. W. Goodwin, and R. H. Ottewill. 2005. Studies on the preparation and characterization of monodisperse polystyrene latices. VI. Preparation of Zwitterionic latices. *Langmuir* 21 (22):9911-9916.

Born, M., and E. Wolf. 1997. *Principles of Optics*. New York: Pergamon.

Bourdon, C. J., M. G. Olsen, and A. D. Gorby. 2004. Validation of an analytical solution for depth of correlation in microscopic particle image velocimetry. *Measurement Science & Technology* 15 (2):318-327.

Bourdon et al. 2006. The depth of correlation in micro-PIV for high numerical aperture and immersion objectives. *Journal of Fluids Engineering-Transactions of the Asme* 128 (4):883-886.

Bown, M. R., J. M. MacInnes, and R. W. K. Allen. 2007. Three-component micro-PIV using the continuity equation and a comparison of the performance with that of stereoscopic measurements. *Experiments in Fluids* 42 (2):197-205.

Bown, M. R., J. M. MacInnes, R. W. K. Allen, and W. B. J. Zimmerman. 2006. Three-dimensional, three-component velocity measurements using stereoscopic micro-PIV and PTV. *Measurement Science & Technology* 17 (8):2175-2185.

Brakenhoff, G. J. 1979. Imaging Modes in Confocal Scanning Light-Microscopy (Cslm). *Journal of Microscopy-Oxford* 117 (NOV):233-242.

Carlsson, K., and N. Aslund. 1987. Confocal Imaging for 3-D Digital Microscopy. *Applied Optics* 26 (16):3232-3238.

Chandrasekhar, S. 1943. Stochastic problems in physics and astronomy. *Reviews of Modern Physics* 15 (1):0001-0089.

Chen, C. H., H. Lin, S. K. Lele, and J. G. Santiago. 2005. Convective and absolute electrokinetic instability with conductivity gradients. *Journal of Fluid Mechanics* 524:263-303.

Cheong, F. C., B. Sun, R. Dreyfus, J. Amato-Grill, K. Xiao, L. Dixon, and D. G. Grier. 2009. Flow visualization and flow cytometry with holographic video microscopy. *Optics Express* 17 (15):13071-13079.

Chong, F.K., C.G. Coates, D.J. Denvir, N. McHale, K. Thornbury, and M. Hollywood. 2004. Optimization of Spinning Disk Confocal Microscopy: Synchronization with the Ultra-Sensitive EMCCD. *Proceedings of SPIE* 5324:65-76.

Cierpka, C., R. Segura, R. Hain, and C. J. Kahler. 2010. A simple single camera 3C3D velocity measurement technique without errors due to depth of correlation and spatial averaging for microfluidics. *Measurement Science & Technology* 21 (4).

Corle, T. R., C. H. Chou, and G. S. Kino. 1986. Depth Response of Confocal Optical Microscopes. *Optics Letters* 11 (12):770-772.

Corle, T.R, and G.S. Kino. 1996. *Confocal scanning optical microscopy and related imaging systems* San Diego: Academic Press.

Crocker, J. C., and D. G. Grier. 1996. Methods of digital video microscopy for colloidal studies. *Journal of Colloid and Interface Science* 179 (1):298-310.

Devasenathipathy, S., J. G. Santiago, and K. Takehara. 2002. Particle tracking techniques for electrokinetic microchannel flows. *Analytical Chemistry* 74 (15):3704-3713.

Devasenathipathy, S., J. G. Santiago, S. T. Wereley, C. D. Meinhart, and K. Takehara. 2003. Particle imaging techniques for microfabricated fluidic systems. *Experiments in Fluids* 34 (4):504-514.

Dinsmore, A. D., E. R. Weeks, V. Prasad, A. C. Levitt, and D. A. Weitz. 2001. Three-dimensional confocal microscopy of colloids. *Applied Optics* 40 (24):4152-4159.

Dinsmore, A. D., and D. A. Weitz. 2002. Direct imaging of three-dimensional structure and topology of colloidal gels. *Journal of Physics-Condensed Matter* 14 (33):7581-7597.

Duffy, D. C., J. C. McDonald, O. J. A. Schueller, and G. M. Whitesides. 1998. Rapid prototyping of microfluidic systems in poly(dimethylsiloxane). *Analytical Chemistry* 70 (23):4974-4984.

Duncan, J., D. Dabiri, J. Hove, and M. Gharib. 2010. Universal outlier detection for particle image velocimetry (PIV) and particle tracking velocimetry (PTV) data. *Measurement Science & Technology* 21 (5).

Eckstein, A., J. Charonko, and P. Vlachos. 2008. Time Resolved Micro PIV. In *14th Int Symp on Applications of Laser Techniques to Fluid Mechanics*. Lisbon, Portugal.

Eckstein, A., and P. P. Vlachos. 2009. Digital particle image velocimetry (DPIV) robust phase correlation. *Measurement Science & Technology* 20 (5).

Erkan, N., K. Shinohara, S. Someya, and K. Okamoto. 2008. Three-component velocity measurement in microscale flows using time-resolved PIV. *Measurement Science & Technology* 19 (5).

Frakes, D. H., K. Pekkan, L. P. Dasi, H. D. Kitajima, D. de Zelicourt, H. L. Leo, J. Carberry, K. Sundareswaran, H. Simon, and A. P. Yoganathan. 2008. Modified control grid interpolation for the volumetric reconstruction of fluid flows. *Experiments in Fluids* 45 (6):987-997.

Frakes, D., M. Smith, D. de Zelicourt, K. Pekkan, and A. Yoganathan. 2004. Three-dimension velocity field reconstruction. *Journal of Biomechanical Engineering-Transactions of the Asme* 126 (6):727-735.

Garstecki, P., M. J. Fuerstman, H. A. Stone, and G. M. Whitesides. 2006. Formation of droplets and bubbles in a microfluidic T-junction - scaling and mechanism of break-up. *Lab on a Chip* 6 (3):437-446.

Haber, C. 2006. Microfluidics in commercial applications; an industry perspective. *Lab on a Chip* 6 (9):1118-1121.

Hajjoul, H., S. Kocanova, I. Lassadi, K. Bystricky, and A. Bancaud. 2009. Lab-on-Chip for fast 3D particle tracking in living cells. *Lab on a Chip* 9 (21):3054-3058.

Hecht, E., and A. Zajac. 1974. *Optics*: Addison-Wesley.

Hoburg, J. F., and J. R. Melcher. 1976. Internal Electrohydrodynamic Instability and Mixing of Fluids with Orthogonal Field and Conductivity Gradients. *Journal of Fluid Mechanics* 73 (JAN27):333-&.

Hunter, R.J. 1981. *Zeta Potential in Colloid Science*. New York: Academic Press.

Ichiyanagi, M., S. Sasaki, Y. Sato, and K. Hishida. 2009. Micro-PIV/LIF measurements on electrokinetically-driven flow in surface modified microchannels. *Journal of Micromechanics and Microengineering* 19 (4).

Inoue, S., and R. Oldenbourg. 1994. Optical instruments: microscopes. In *Handbook of Optics*, edited by J. Pawley. New York: McGraw-Hill.

Jain, A., and J. D. Posner. 2008. Particle dispersion and separation resolution of pinched flow fractionation. *Analytical Chemistry* 80 (5):1641-1648.

Jenkins, M. C., and S. U. Egelhaaf. 2008. Confocal microscopy of colloidal particles: Towards reliable, optimum coordinates. *Advances in Colloid and Interface Science* 136 (1-2):65-92.

Kajitani, L., and D. Dabiri. 2005. A full three-dimensional characterization of defocusing digital particle image velocimetry. *Measurement Science & Technology* 16 (3):790-804.

Keane, R. D., and R. J. Adrian. 1992. Theory of Cross-Correlation Analysis of Piv Images. *Applied Scientific Research* 49 (3):191-215.

Keane, R. D., R. J. Adrian, and Y. Zhang. 1995. Superresolution Particle Imaging Velocimetry. *Measurement Science & Technology* 6 (6):754-768.

Keane, R.D., and R. J. Adrian. 1993. Theory of cross-correlation analysis of PIV images. In *Flow Visualization and Analysis*, edited by F. T. M. Nieuwstadt. Dordrecht: Kluwer Academic Publishers.

Kim, H. B., and S. J. Lee. 2002. Performance improvement of two-frame particle tracking velocimetry using a hybrid adaptive scheme. *Measurement Science & Technology* 13 (4):573-582.

Kim, S., and S. J. Lee. 2007. Measurement of 3D laminar flow inside a micro tube using micro digital holographic particle tracking velocimetry. *Journal of Micromechanics and Microengineering* 17 (10):2157-2162.

Kino, G. S., and T. R. Corle. 1989. Confocal Scanning Optical Microscopy. *Physics Today* 42 (9):55-62.

Kinoshita, H., S. Kaneda, T. Fujii, and M. Oshima. 2007. Three-dimensional measurement and visualization of internal flow of a moving droplet using confocal micro-PIV. *Lab on a Chip* 7 (3):338-346.

Klein, S. A., J.L. Moran, D. Frakes, and J. D. Posner. 2011. Three-dimensional three-component direct micro particle velocimetry using volumetric scanning. *Measurement Science & Technology*.

Klein, S. A., and J. D. Posner. 2010. Improvement in two-frame correlations by confocal microscopy for temporally resolved micro particle imaging velocimetry. *Measurement Science & Technology* 21 (10).

Lee, S. J., and S. Kim. 2009. Advanced particle-based velocimetry techniques for microscale flows. *Microfluidics and Nanofluidics* 6 (5):577-588.

Lima, R., S. Wada, M. Takeda, K. I. Tsubota, and T. Yamaguchi. 2007. In vitro confocal micro-PIV measurements of blood flow in a square microchannel: The effect of the haematocrit on instantaneous velocity profiles. *Journal of Biomechanics* 40 (12):2752-2757.

Lima, R., S. Wada, S. Tanaka, M. Takeda, T. Ishikawa, K. I. Tsubota, Y. Imai, and T. Yamaguchi. 2008. In vitro blood flow in a rectangular PDMS microchannel: experimental observations using a confocal micro-PIV system. *Biomedical Microdevices* 10 (2):153-167.

Lima, R., S. Wada, K. Tsubota, and T. Yamaguchi. 2006. Confocal micro-PIV measurements of three-dimensional profiles of cell suspension flow in a square microchannel. *Measurement Science & Technology* 17 (4):797-808.

Lin, H. 2009. Electrokinetic instability in microchannel flows: A review. *Mechanics Research Communications* 36 (1):33-38.

Lin, H., B. D. Storey, M. H. Oddy, C. H. Chen, and J. G. Santiago. 2004. Instability of electrokinetic microchannel flows with conductivity gradients. *Physics of Fluids* 16 (6):1922-1935.

Lindken, R., M. Rossi, S. Grosse, and J. Westerweel. 2009. Micro-Particle Image Velocimetry (mu PIV): Recent developments, applications, and guidelines. *Lab on a Chip* 9 (17):2551-2567.

Lindken, R., J. Westerweel, and B. Wieneke. 2006. Stereoscopic micro particle image velocimetry. *Experiments in Fluids* 41 (2):161-171.

Meinhart, C. D., S. T. Wereley, and M. H. B. Gray. 2000. Volume illumination for two-dimensional particle image velocimetry. *Measurement Science & Technology* 11 (6):809-814.

Meinhart, C. D., S. T. Wereley, and J. G. Santiago. 1999. PIV measurements of a microchannel flow. *Experiments in Fluids* 27 (5):414-419.

Meinhart, C. D., S. T. Wereley, and J. G. Santiago. 2000. A PIV algorithm for estimating time-averaged velocity fields. *Journal of Fluids Engineering-Transactions of the Asme* 122 (2):285-289.

Meinhart, C. D., and H. S. Zhang. 2000. The flow structure inside a microfabricated inkjet printhead. *Journal of Microelectromechanical Systems* 9 (1):67-75.

Melcher, J. R., and G. I. Taylor. 1969. Electrohydrodynamics - a Review of Role of Interfacial Shear Stresses. *Annual Review of Fluid Mechanics* 1:111-&.

Mielnik, M. M., and L. R. Saetran. 2006. Selective seeding for micro-PIV. *Experiments in Fluids* 41 (2):155-159.

Mori, N., and K. Chang. 2003. Introduction to MPIV. Review of Reviewed Item.

Nagai, M., M. Oishi, M. Oshima, H. Asai, and H. Fujita. 2009. Three-dimensional two-component velocity measurement of the flow field induced by the Vorticella picta microorganism using a confocal microparticle image velocimetry technique. *Biomicrofluidics* 3 (1).

Navaneetham, G., and J. D. Posner. 2009. Electrokinetic instabilities of non-dilute colloidal suspensions. *Journal of Fluid Mechanics* 619:331-365.

Oddy, M. H., and J. G. Santiago. 2005. Multiple-species model for electrokinetic instability. *Physics of Fluids* 17 (6).

Oddy, M. H., J. G. Santiago, and J. C. Mikkelsen. 2001. Electrokinetic instability micromixing. *Analytical Chemistry* 73 (24):5822-5832.

Okamoto, K., S. Nishio, T. Saga, and T. Kobayashi. 2000. Standard images for particle-image velocimetry. *Measurement Science & Technology* 11 (6):685-691.

Olsen, M. G. 2009. Directional dependence of depth of correlation due to in-plane fluid shear in microscopic particle image velocimetry. *Measurement Science & Technology* 20 (1).

Olsen, M. G. 2010. Depth of correlation reduction due to out-of-plane shear in microscopic particle image velocimetry. *Measurement Science & Technology* 21 (10).

Olsen, M. G., and R. J. Adrian. 2000. Brownian motion and correlation in particle image velocimetry. *Optics and Laser Technology* 32 (7-8):621-627.

Olsen, M. G., and R. J. Adrian. 2000. Out-of-focus effects on particle image visibility and correlation in microscopic particle image velocimetry. *Experiments in Fluids* 29:S166-S174.

Ooms, T. A., R. Lindken, and J. Westerweel. 2009. Digital holographic microscopy applied to measurement of a flow in a T-shaped micromixer. *Experiments in Fluids* 47 (6):941-955.

Ozen, O., N. Aubry, D. T. Papageorgiou, and P. G. Petropoulos. 2006. Electrohydrodynamic linear stability of two immiscible fluids in channel flow. *Electrochimica Acta* 51 (25):5316-5323.

Park, J. S., C. K. Choi, and K. D. Kihm. 2004. Optically sliced micro-PIV using confocal laser scanning microscopy (CLSM). *Experiments in Fluids* 37 (1):105-119.

Park, J. S., C. K. Choi, K. D. Kihm, and J.S. Allen. 2003. Optically-Sectioned Micro PIV Measurements Using CLSM. *Transactions of the ASME* 125 (4):542.

Park, J. S., and K. D. Kihm. 2006. Three-dimensional micro-PTV using deconvolution microscopy. *Experiments in Fluids* 40 (3):491-499.

Park, J. S., and K. D. Kihm. 2006. Use of confocal laser scanning microscopy (CLSM) for depthwise resolved microscale-particle image velocimetry (mu-PIV). *Optics and Lasers in Engineering* 44 (3-4):208-223.

Pereira, F., and M. Gharib. 2002. Defocusing digital particle image velocimetry and the three-dimensional characterization of two-phase flows. *Measurement Science & Technology* 13 (5):683-694.

Pereira, F., H. Stuer, E. C. Graff, and M. Gharib. 2006. Two-frame 3D particle tracking. *Measurement Science & Technology* 17 (7):1680-1692.

Peterson, S. D., H. S. Chuang, and S. T. Wereley. 2008. Three-dimensional particle tracking using micro-particle image velocimetry hardware. *Measurement Science & Technology* 19 (11).

Petran, M., Hadravsk.M, M. D. Egger, and R. Galambos. 1968. Tandem-Scanning Reflected-Light Microscope. *Journal of the Optical Society of America* 58 (5):661-&.

Posner, J. D., and J. G. Santiago. 2006. Convective instability of electrokinetic flows in a cross-shaped microchannel. *Journal of Fluid Mechanics* 555:1-42.

Prasad, A. K., R. J. Adrian, C. C. Landreth, and P. W. Offutt. 1992. Effect of Resolution on the Speed and Accuracy of Particle Image Velocimetry Interrogation. *Experiments in Fluids* 13 (2-3):105-116.

Prasad, V., D. Semwogerere, and E. R. Weeks. 2007. Confocal microscopy of colloids. *Journal of Physics-Condensed Matter* 19 (11).

Prieve, D. C., H. L. Gerhart, and R. E. Smith. 1978. Chemiphoresis - Method for Deposition of Polymer-Coatings without Applied Electric-Current. *Industrial & Engineering Chemistry Product Research and Development* 17 (1):32-36.

Raffel, M., J. Westerweel, C. Willert, M. Gharib, and J. Kompenhans. 1996. Analytical and experimental investigations of dual-plane particle image velocimetry. *Optical Engineering* 35 (7):2067-2074.

Santiago, J. G., S. T. Wereley, C. D. Meinhart, D. J. Beebe, and R. J. Adrian. 1998. A particle image velocimetry system for microfluidics. *Experiments in Fluids* 25 (4):316-319.

Santos, J. J., and B. D. Storey. 2008. Instability of electro-osmotic channel flow with streamwise conductivity gradients. *Physical Review E* 78 (4).

Scarano, F. 2002. Iterative image deformation methods in PIV. *Measurement Science & Technology* 13 (1):R1-R19.

Scarano, F., and M. L. Riethmuller. 1999. Iterative multigrid approach in PIV image processing with discrete window offset. *Experiments in Fluids* 26 (6):513-523.

Schmieg, J., A. Eckstein, J. Charonko, and P. Vlachos. 2009. A Methodology for Time-Resolved microDPIV. Paper read at American Physical Society, Division of Fluid Dynamics, 11/24/2009, at Minneapolis, MN.

Shah, R.K., and A.L. London. 1978. *Laminar Flow Forced Convection in Ducts*. New York: Academic.

Sheng, J., E. Malkiel, and J. Katz. 2006. Digital holographic microscope for measuring three-dimensional particle distributions and motions. *Applied Optics* 45 (16):3893-3901.

Sheppard, C. J. R., and A. Choudhury. 1977. Image-Formation in Scanning Microscope. *Optica Acta* 24 (10):1051-1073.

Sheppard, C. J. R., and T. Wilson. 1978. Depth of Field in Scanning Microscope. *Optics Letters* 3 (3):115-117.

Shinohara, K., Y. Sugii, A. Aota, A. Hibara, M. Tokeshi, T. Kitamori, and K. Okamoto. 2004. High-speed micro-PIV measurements of transient flow in microfluidic devices. *Measurement Science & Technology* 15 (10):1965-1970.

Shinohara, K., Y. Sugii, J. H. Jeong, and K. Okamoto. 2005. Development of a three-dimensional scanning microparticle image velocimetry system using a piezo actuator. *Review of Scientific Instruments* 76 (10).

Stitou, A., and M. L. Riethmuller. 2001. Extension of PIV to super resolution using PTV. *Measurement Science & Technology* 12 (9):1398-1403.

Storey, B. D. 2005. Direct numerical simulation of electrohydrodynamic flow instabilities in microchannels. *Physica D-Nonlinear Phenomena* 211 (1-2):151-167.

Takehara, K., R. J. Adrian, G. T. Etoh, and K. T. Christensen. 2000. A Kalman tracker for super-resolution PIV. *Experiments in Fluids* 29:S34-S41.

Tanaami, T., S. Otsuki, N. Tomosada, Y. Kosugi, M. Shimizu, and H. Ishida. 2002. High-speed 1-frame/ms scanning confocal microscope with a microlens and Nipkow disks. *Applied Optics* 41 (22):4704-4708.

Trau, M., D. A. Saville, and I. A. Aksay. 1997. Assembly of colloidal crystals at electrode interfaces. *Langmuir* 13 (24):6375-6381.

van Steijn, V., M. T. Kreutzer, and C. R. Kleijn. 2007. mu-PIV study of the formation of segmented flow in microfluidic T-junctions. *Chemical Engineering Science* 62 (24):7505-7514.

Vedula, P., and R. J. Adrian. 2005. Optimal solenoidal interpolation of turbulent vector fields: application to PTV and super-resolution PIV. *Experiments in Fluids* 39 (2):213-221.

Webb, R. H. 1996. Confocal optical microscopy. *Reports on Progress in Physics* 59 (3):427-471.

Weeks, E. R., J. C. Crocker, A. C. Levitt, A. Schofield, and D. A. Weitz. 2000. Three-dimensional direct imaging of structural relaxation near the colloidal glass transition. *Science* 287 (5453):627-631.

Wereley, S. T., L. Gui, and C. D. Meinhart. 2002. Advanced algorithms for microscale particle image velocimetry. *Aiaa Journal* 40 (6):1047-1055.

Wereley, S. T., and C. D. Meinhart. 2010. Recent Advances in Micro-Particle Image Velocimetry. *Annual Review of Fluid Mechanics* 42:557-576.

Wernet, M. P. 2005. Symmetric phase only filtering: a new paradigm for DPIV data processing. *Measurement Science & Technology* 16 (3):601-618.

Westerweel, J., and B. Lecordier. 2003. The EUROPIV Synthetic Image Generator In *EUROPIV 2 workshop* Zaragoza, Spain.

Westerweel, J., and F. Scarano. 2005. Universal outlier detection for PIV data. *Experiments in Fluids* 39 (6):1096-1100.

Wilhelm, S., B. Grobler, M. Gluch, and H. Heinz. 2003. *Confocal laser scanning microscopy: principles.*: Carl Zeiss.

Wilson, T., and A. R. Carlini. 1987. Depth Discrimination Criteria in Confocal Optical-Systems. *Optik* 76 (4):164-166.

Wilson, T., and A. R. Carlini. 1987. Size of the Detector in Confocal Imaging-Systems. *Optics Letters* 12 (4):227-229.

Xiao, G. Q., T. R. Corle, and G. S. Kino. 1988. Real-Time Confocal Scanning Optical Microscope. *Applied Physics Letters* 53 (8):716-718.

Yamamoto, Y., and T. Uemura. 2003. A new super-resolution PIV accelerated by characteristic pixel selection. *Journal of Visualization* 6 (3):263-272.

Yoon, S. Y., and K. C. Kim. 2006. 3D particle position and 3D velocity field measurement in a microvolume via the defocusing concept. *Measurement Science & Technology* 17 (11):2897-2905.

Zukoski, C. F., and D. A. Saville. 1987. Electrokinetic Properties of Particles in Concentrated Suspensions. *Journal of Colloid and Interface Science* 115 (2):422-436.

APPENDIX A

MODEL OF POINT SPREAD FUNCTION FOR CONFOCAL SYSTEM

```
function
PSFuvCompute(pr,Mag,lambda,maxNM,maxr,maxz,R,n,NA,direct_alt,direct,nam
e_alt,rsphere)
% 3D PSF
% 3D object
FS = 18;
FN = 'Times New Roman';

% calcuate amplitude
r = linspace(-maxr,maxr,maxNM);
z = linspace(-maxz,maxz,maxNM);
N = length(r);
M = length(z);
alpha = asin(NA./n);
f_num = n/(2*NA);
v = 2*pi*n/lambda * sin(alpha)*r;
%v = 2*pi/lambda * f_num*r;
u = 8*pi*n/lambda * sin(alpha/2)^2*z;
%u = 2*pi/lambda * (f_num)^2*z;
doLoop = 0;


% with confocal
% add in pinhole function

PR = pr/Mag;
%vr = 2*pi/lambda * f

% create 3D psf
if doLoop == 1
   load('I.mat')
   load('r2.mat')
   load('v.mat')

else
   tic
   for i=1:N
      for j = 1:M
            V0sum = 0;
            V1sum = 0;
            U1sum = 0;
            U2sum = 0;
            if abs(u(j)/v(i)) < 1
               for s = 1:R
```

```
                U1sum = (-1)^(s-1) * (u(j)./v(i))^(1+2*(s-1)) * besselj(1+2*(s-
1),v(i)) + U1sum;
                U2sum = (-1)^(s-1) * (u(j)./v(i))^(2+2*(s-1)) * besselj(2+2*(s-
1),v(i)) + U2sum;
            end
            U1(i,j) = U1sum;
            U2(i,j) = U2sum;
            I(i,j) = abs((2/u(j)^2) * (U1(i,j)^2 + U2(i,j)^2));
        elseif abs(u(j)/v(i)) > 1
            for s = 1:R
                V0sum = (-1)^(s-1) * (v(i)/u(j))^(0+2*(s-1)) * besselj(0+2*(s-
1),v(i)) + V0sum;
                V1sum = (-1)^(s-1) * (v(i)/u(j))^(1+2*(s-1)) * besselj(1+2*(s-
1),v(i)) + V1sum;
            end
            V0(i,j) = V0sum;
            V1(i,j) = V1sum;
            I(i,j) = abs((2/u(j)^2) * (1 + V0(i,j)^2 + V1(i,j)^2 -
2*V0(i,j)*cos(.5*(u(j)+v(i)^2/u(j))) - 2*V1(i,j)*sin(0.5*(u(j)+v(i)^2/u(j)))));
        elseif abs(u(j)/v(i)) == 1
            I(i,j) = abs((1 - 2*bessel(0,u(j))*cos(u(j)) + besselj(0,u(j))^2)/u(j)^2);
%           elseif u(j) == 0 && v(i) ~= 0
%               I(i,j) = abs(2*besselj(0,v(i))/v(i));
%           elseif v(i) == 0 && u(j) ~= 0
%               I(i,j) = sin(u(j))^2 / u(j)^2;
%           elseif u(j) == 0 && v(i) == 0
%               I(i,j) = 1;
        end
        r2(i,j) = sqrt(z(j)^2 + r(i)^2);

        % Q(v) + 2/pi*(acos(v/(2*vp)) - (v/(2*vp))*sqrt(1 - (v/(2*vp))^2));

        if j == M/2
            if abs(r(i)) <= PR
                A(i,j)=1;
            else
                A(i,j) =0;
            end
        else
            A(i,j)=0;
        end

        if i == N/2
            if abs(z(j)) <= PR
                B(i,j)=1;
            else
```

```
                B(i,j) =0;
            end
        else
            B(i,j)=0;
        end

    end
    if mod(i,10)==0
        i
    end
  end

end
toc



r1 = r./max(r);
z1 = z./max(z);

% draw a image of a sphere in 3D

for i=1:N
  for j=1:M
      if abs(r2(i,j)) <= rsphere
          rconv(i,j) = 1;
      else
          rconv(i,j) = 0;
      end
  end
end

if exist(direct)==0
  mkdir(direct)
end


I = I./max(max(I));
%I(1,1) = 1;
figure1=figure;
axes1=axes;
set(axes1,'FontSize',16)
%
contour(r,z,I)
ylabel('r','FontSize',FS,'FontName',FN)
xlabel('z','FontSize',FS,'FontName',FN)
```

```
zlabel('I','FontSize',FS,'FontName',FN)
title(['PSF standard microscope' num2str(maxr) ' um by ' num2str(maxz) ' um'])
name = 'psfstandard';
saveas(gcf,[direct name name_alt '.fig']);
%saveas(gcf,[direct name name_alt '.bmp']);
%saveas(gcf,[direct name name_alt '.tif']);
close(gcf)
% % Take fft of radial psf
tic
% take the fast fourier transform

 % fftS = fftshift(fftS);
 Image2 = convnfft(I,rconv,'same');
 %fftA = fftn(A);
 % Infinitely small pinhole
 IConf = I.*I;

 IConfpinhole1 = convnfft(I,A,'same');
 IConfpinhole2 = convnfft(I,B,'same');
 IConfpinhole =  IConfpinhole1.*IConfpinhole1;
 IConfpinhole =  IConfpinhole./max(max(IConfpinhole));
 IConfpinhole_prime =  IConfpinhole2.*IConfpinhole2;
 IConfpinhole_prime =  IConfpinhole_prime./max(max(IConfpinhole_prime));
 ImageConf = convnfft(IConf,rconv,'same');
 ImageConfpinhole = convnfft(IConfpinhole,rconv,'same');
 ImageConfpinhole_prime = convnfft(IConfpinhole_prime,rconv,'same');



 disp('fft time =')
 toc

figure
contour(r,z,rconv)
ylabel('r','FontSize',FS,'FontName',FN)
xlabel('z','FontSize',FS,'FontName',FN)
zlabel('I','FontSize',FS,'FontName',FN)
title(['object standard microscope' num2str(maxr) ' um by ' num2str(maxz) ' um'])
%
name = 'object';
saveas(gcf,[direct name name_alt '.fig']);
%saveas(gcf,[direct name name_alt '.bmp']);
%saveas(gcf,[direct name name_alt '.tif']);
close(gcf)
```

```
Image2 = Image2./max(max(Image2));
ImageConf = ImageConf./max(max(ImageConf));
ImageConfpinhole = ImageConfpinhole./max(max(ImageConfpinhole));
ImageConfpinhole_prime =
ImageConfpinhole_prime./max(max(ImageConfpinhole_prime));
% LL = length(Image);



%
figure
contour(r,z,IConf)
ylabel('r','FontSize',FS,'FontName',FN)
xlabel('z','FontSize',FS,'FontName',FN)
zlabel('I','FontSize',FS,'FontName',FN)
title(['psf confocal microscope' num2str(maxr) ' um by ' num2str(maxz) ' um'])
name = 'psfConfocal_small';
set(gca,'FontSize',FS,'FontName',FN);

saveas(gcf,[direct name name_alt  '.fig']);
%saveas(gcf,[direct name name_alt '.bmp']);
%saveas(gcf,[direct name name_alt '.tif']);
close(gcf)

figure
contour(r,z,IConfpinhole)
ylabel('r','FontSize',FS,'FontName',FN)
xlabel('z','FontSize',FS,'FontName',FN)
zlabel('I','FontSize',FS,'FontName',FN)
title(['psf pinhole confocal microscope' num2str(maxr) ' um by ' num2str(maxz) '
um'])
name = 'psfConfocal_large';
saveas(gcf,[direct name name_alt '.fig']);
%saveas(gcf,[direct name name_alt '.bmp']);
%saveas(gcf,[direct name name_alt '.tif']);
close(gcf)

figure
contour(r,z,Image2)
ylabel('r','FontSize',FS,'FontName',FN)
xlabel('z','FontSize',FS,'FontName',FN)
zlabel('I','FontSize',FS,'FontName',FN)
title(['convolved standard microscope fft' num2str(maxr) ' um by ' num2str(maxz)
' um'])
%
name = 'convolvedStandard';
```

```
saveas(gcf,[direct name name_alt '.fig']);
%saveas(gcf,[direct name name_alt '.bmp']);
%saveas(gcf,[direct name name_alt '.tif']);
close(gcf)

figure
contour(r,z,ImageConf)
ylabel('r','FontSize',FS,'FontName',FN)
xlabel('z','FontSize',FS,'FontName',FN)
zlabel('I','FontSize',FS,'FontName',FN)
title(['convolved confocal microscope fft small pinhole' num2str(maxr) ' um by '
num2str(maxz) ' um'])
name = 'convolvedConfocal_small';
saveas(gcf,[direct name name_alt '.fig']);
%saveas(gcf,[direct name name_alt '.bmp']);
%saveas(gcf,[direct name name_alt '.tif']);
close(gcf)
%
figure
contour(r,z,ImageConfpinhole)
ylabel('r','FontSize',FS,'FontName',FN)
xlabel('z','FontSize',FS,'FontName',FN)
zlabel('I','FontSize',FS,'FontName',FN)
title(['convolved confocal microscope fft big pinhole' num2str(maxr) ' um by '
num2str(maxz) ' um'])
%
name = 'convolvedConfocal_large';
saveas(gcf,[direct name name_alt '.fig']);
%saveas(gcf,[direct name name_alt '.bmp']);
%saveas(gcf,[direct name name_alt '.tif']);
close(gcf)

figure
contour(r,z,IConfpinhole_prime)
ylabel('r','FontSize',FS,'FontName',FN)
xlabel('z','FontSize',FS,'FontName',FN)
zlabel('I','FontSize',FS,'FontName',FN)
title(['psf confocal microscope fft big pinhole prime' num2str(maxr) ' um by '
num2str(maxz) ' um'])
name = 'psfConfocal_large_prime';
saveas(gcf,[direct name name_alt '.fig']);
%saveas(gcf,[direct name name_alt '.bmp']);
%saveas(gcf,[direct name name_alt '.tif']);
close(gcf)
%
figure
```

```
contour(r,z,ImageConfpinhole_prime)
ylabel('r','FontSize',FS,'FontName',FN)
xlabel('z','FontSize',FS,'FontName',FN)
zlabel('I','FontSize',FS,'FontName',FN)
title(['convolved confocal microscope fft big pinhole prime' num2str(maxr) ' um
by ' num2str(maxz) ' um'])
name = 'convolvedConfocal_large_prime';
saveas(gcf,[direct name name_alt '.fig']);
%saveas(gcf,[direct name name_alt '.bmp']);
%saveas(gcf,[direct name name_alt '.tif']);
close(gcf)


HML = linspace(0.5,0.5,maxNM);
CML = linspace(0.1,0.1,maxNM);
[FWHMz] = ComputeDoC(z,I(N/2,:),HML);
[DoCz] = ComputeDoC(z,I(N/2,:),CML);
[FWHMr] = ComputeDoC(r,I(:,M/2),HML);
[DoCr] = ComputeDoC(r,I(:,M/2),CML);

[FWHMz_c] = ComputeDoC(z,IConf(N/2,:),HML);
[DoCz_c] = ComputeDoC(z,IConf(N/2,:),CML);
[FWHMr_c] = ComputeDoC(r,IConf(:,M/2),HML);
[DoCr_c] = ComputeDoC(r,IConf(:,M/2),CML);

[FWHMz_cp] = ComputeDoC(z,IConfpinhole(N/2,:),HML);
[DoCz_cp] = ComputeDoC(z,IConfpinhole(N/2,:),CML);
[FWHMr_cp] = ComputeDoC(r,IConfpinhole(:,M/2),HML);
[DoCr_cp] = ComputeDoC(r,IConfpinhole(:,M/2),CML);

[FWHMz_cpp] = ComputeDoC(z,IConfpinhole_prime(N/2,:),HML);
[DoCz_cpp] = ComputeDoC(z,IConfpinhole_prime(N/2,:),CML);
[FWHMr_cpp] = ComputeDoC(r,IConfpinhole_prime(:,M/2),HML);
[DoCr_cpp] = ComputeDoC(r,IConfpinhole_prime(:,M/2),CML);


[FWHMz_s] = ComputeDoC(z,Image2(N/2,:),HML);
[DoCz_s] = ComputeDoC(z,Image2(N/2,:),CML);
[FWHMr_s] = ComputeDoC(r,Image2(:,M/2),HML);
[DoCr_s] = ComputeDoC(r,Image2(:,M/2),CML);

[FWHMz_sc] = ComputeDoC(z,ImageConf(N/2,:),HML);
[DoCz_sc] = ComputeDoC(z,ImageConf(N/2,:),CML);
[FWHMr_sc] = ComputeDoC(r,ImageConf(:,M/2),HML);
[DoCr_sc] = ComputeDoC(r,ImageConf(:,M/2),CML);
```

```
[FWHMz_scp] = ComputeDoC(z,ImageConfpinhole(N/2,:),HML);
[DoCz_scp] = ComputeDoC(z,ImageConfpinhole(N/2,:),CML);
[FWHMr_scp] = ComputeDoC(r,ImageConfpinhole(:,M/2),HML);
[DoCr_scp] = ComputeDoC(r,ImageConfpinhole(:,M/2),CML);

[FWHMz_scpp] = ComputeDoC(z,ImageConfpinhole_prime(N/2,:),HML);
[DoCz_scpp] = ComputeDoC(z,ImageConfpinhole_prime(N/2,:),CML);
[FWHMr_scpp] = ComputeDoC(r,ImageConfpinhole_prime(:,M/2),HML);
[DoCr_scpp] = ComputeDoC(r,ImageConfpinhole_prime(:,M/2),CML);


fid1=fopen('I:\Confocal
Theory\psf3d\2Dconvn_new\Auto\Results\FWHM_simulated.csv','a');
fprintf(fid1,['\n' num2str(rsphere*2*1000) ',' num2str(PR*2) ',' num2str(NA) ','
num2str(FWHMz) ',' num2str(FWHMr) ',' num2str(DoCz) ',' num2str(DoCr) ','
num2str(FWHMz_c) ',' num2str(FWHMr_c) ',' num2str(DoCz_c) ','
num2str(DoCr_c) ',' num2str(FWHMz_cp) ',' num2str(FWHMr_cp) ','
num2str(DoCz_cp) ',' num2str(DoCr_cp) ',' num2str(FWHMz_cpp) ','
num2str(FWHMr_cpp) ',' num2str(DoCz_cpp) ',' num2str(DoCr_cpp) ','
num2str(FWHMz_s) ',' num2str(FWHMr_s) ',' num2str(DoCz_s) ','
num2str(DoCr_s) ',' num2str(FWHMz_sc) ',' num2str(FWHMr_sc) ','
num2str(DoCz_sc) ',' num2str(DoCr_sc) ',' num2str(FWHMz_scp) ','
num2str(FWHMr_scp) ',' num2str(DoCz_scp) ',' num2str(DoCr_scp) ','
num2str(FWHMz_scpp) ',' num2str(FWHMr_scpp) ',' num2str(DoCz_scpp) ','
num2str(DoCr_scpp)]);
fclose(fid1);
fclose('all');
save([direct 'vars' name_alt])

function [Returnfw] = ComputeDoC(z,I,p)

[fw,y0,iout,jout] = intersections(z,I,z,p);
Returnfw = sum(abs(fw));
```

APPENDIX B

CONFOCAL SYSTEM MODIFICATION INSTRUCTIONS

CARV II Confocal System Instructions for Modification:

You need to short pins 6 and 7 together.

Pin 9 – Readout for Disk Speed

To read, attach ONLY positive electrode from digital multimeter to readout (let ground from multimeter float). Then set multimeter to read AC frequency (Hz). Multiply this frequency by 20 to get the disk speed in RPM.

Pins 1 and 2

These pins are used to attach the power supply, pin 1 is positive, pin 2 is negative. An external power supply can be used up to 35 V (3 Amps maximum) in order to reach a disk speed of over 10000 RPM.

To drive the disk speed over 10000 RPM:

Connect a jumper to the jumper connector (JP1) that is left of pin 9 when viewed from the top of control board. This bypasses the limiter that keeps the disk spinning at < 10k RPM.

Next attach an external power supply to pins 1 and 2 and apply more than 12 V DC.

There is a rotating control knob near pin 9 that controls the disk speed. Applying > 12V to the board with JP1 shorted will simply alter the maximum speed obtainable, however the actual disk speed is still controlled with this knob.

Take care when you attach the external power supply to turn the knob to the lowest setting before putting the disk in.

Yellow in Pin 5.

Overriding the disk speed control knob:

If you connect a jumper to the jumper connector (JP2) that is beneath Pin 8 when viewed from the top of control board, this will cause the disk to always spin at the maximum speed set by the applied voltage at Pins 1 and 2 (for 12 V applied this is 10000 RPM).

CARV II External Power Directions

Power up

1) Turn on CARV II controller module.
2) Ensure DC Power supply "DC Out" is not pressed in.
3) Ensure current knob is at half maximum.
4) Ensure voltage knob is at 12 Volts.

Turn on disk

5) Insert Disk using software or on controller
6) Press "DC Out" to turn on DC power.

Turn off disk

7) Press "DC Out" to turn off DC power
8) Press Disk button to remove disk

Power down

9) IMPORTANT: Do not turn off the CARV system with the DC Power module on. MAKE CERTAIN that the "DC Out" button is not pushed in and/or make sure the DC power supply is off.